INFORMATION TO USERS

This manuscript has been reproduced from the microfilm master. UMI films the text directly from the original or copy submitted. Thus, some thesis and dissertation copies are in typewriter face, while others may be from any type of computer printer.

The quality of this reproduction is dependent upon the quality of the copy submitted. Broken or indistinct print, colored or poor quality illustrations and photographs, print bleedthrough, substandard margins, and improper alignment can adversely affect reproduction.

In the unlikely event that the author did not send UMI a complete manuscript and there are missing pages, these will be noted. Also, if unauthorized copyright material had to be removed, a note will indicate the deletion.

Oversize materials (e.g., maps, drawings, charts) are reproduced by sectioning the original, beginning at the upper left-hand corner and continuing from left to right in equal sections with small overlaps.

ProQuest Information and Learning
300 North Zeeb Road, Ann Arbor, MI 48106-1346 USA
800-521-0600

UNIVERSITY OF CALGARY

The feasibility of measuring regional lung perfusion with a conventional CT scanner

by

Parminder Singh Basran

A THESIS

SUBMITTED TO THE FACULTY OF GRADUATE STUDIES

IN PARTIAL FULFILLMENT OF THE REQUIREMENTS FOR THE

DEGREE OF DOCTOR OF PHILOSOPHY

Department of Physics and Astronomy

Calgary, Alberta

September, 2002

ABSTRACT

Given the technical limitations of conventional CT scanners and the physiological characteristics of pulmonary perfusion, the goal of this work was to assess the feasibility of measuring regional lung perfusion with a conventional CT scanner. A variety of theoretical and experimental work was undertaken to address specific difficulties encountered in such a measurement.

Seventeen patients participated in a study to assess the reliability of an assisted breath-hold technique to reduce respiratory motion artifacts. For the majority of these patients, respiratory motion was reduced from 1.7 cm to 0.4 cm when using the assisted breath-hold technique. Because the injection protocol in a functional study requires that a highly concentrated pulse of the contrast be delivered in a very short time, the relationship between contrast concentration and CT number must be carefully studied. Therefore, this relationship was theoretically and experimentally examined. The linearity between CT number and contrast concentration was found to falter when: 1) x-rays become beam-hardened in the contrast; 2) there are large variations in concentration within the CT scan-time, and; 3) the contrast passes through the imaging plane rapidly. Streaking artifacts emanating from vessels containing the contrast were found to perturb the CT number in the surrounding vessel. This is primarily due to the time changes in density in the vessel, rather than beam-hardening. To obtain reliable perfusion estimates in the presence of noisy data, a non-model based deconvolution method that uses the input, tissue and output signals of blood flow was developed. This method was shown to

be more reliable than more conventional methods of deconvolution. High signal-to-noise ratios in the lung were obtained when using a low tube-energy (100 or 120 kVp) and large slice thickness (0.5-1.0 cm).

A pilot study to measure regional lung perfusion on a cancer patient was successfully performed. This work demonstrates the first reported measurement of regional lung perfusion using a conventional CT scanner. Because conventional scanners are accessible in most clinics and this technique requires only minor modifications to these scanners, there is great potential in the use of functional CT in healthy and diseased lung.

ACKNOWLEDGMENTS

I have had the fortune of working with a number of helpful and friendly people during my tenure at the Tom Baker Cancer Centre. But first and foremost, I want to thank Dr David Spencer for encouraging me to enroll into the PhD program and guiding me throughout this adventure. He is an exceptional supervisor and friend.

I am also indebted for past and present directors Drs George Sandison and Peter Dunscombe for providing a friendly academic environment at the Tom Baker Cancer Centre while also providing some gratefully accepted pay-stubs. Chairs Drs Bart Hicks and Sandy Murphree from the Department of Physics and Astronomy both provided support and sage advice during my program. Ms Tracy Korsgaard, Ms Linda Livermore and Ms Brenda Cremer demonstrated both skill and patience, despite my administrative foolhardiness. Past and present graduate students often provided me with coffee breaks and inane banter to quench those mental lulls. A special note of thanks goes to John Kollar whose company was always refreshing, appreciated, and enjoyable. I would like to thank Velo investments and Varian Oncology Systems for their financial support.

Also acknowledged are the efforts from Dr Marc Mackenzie for providing a copy of his DICOM-Matlab conversion scripts for CT images, Dr Oguchi in providing me with their injection protocol and insight into their studies, Leo Moriarity and John Schneider for their exceptional skill in designing and constructing most of the phantoms in this work, Kurt Knibutat, Rahim Heshmati, and Ed Rhymes for their electronics support, Yvette Bayliss and Darren Graham for their simulator and CT expertise, and the rest of

Department of Physics at the Tom Baker Cancer Centre for their support and contributions. I would also like to thank those on my supervisory and examining committees, with special thanks to Dr Pelizzari for making the trek from Chicago.

This work would not be possible were it not for Dr Ian Kay, whose academic input, guidance and generosity is sincerely appreciated. A special note of thanks is also given for Eva and Scapa for their hospitality and friendship.

My family has been extremely supportive of this endeavor and they deserve credit for both the glory and the shame. My parents, Parkash and Gurbax, never once rescinded their support. My siblings (Sat, Belbi and Manjeet), sister-in-laws (Gurjinder and Anita), brother-in-law (William) and Max, Amit, Arun, Akash and Sameena have been an extraordinary support group. My wife's family have all have contributed via food, encouragement, and inspiration.

Last, I cannot forget my wife, Kim, who sacrificed much for me during this PhD. Those sacrifices will not be forgotten. She's my best friend and a nerd too!

DEDICATION

This thesis is dedicated to my wife,

Kim Paula Nayyer

for her encouragement, support, love,

and, of course, her proofing reading skills.

TABLE OF CONTENTS

LIST OF TABLES

LIST OF FIGURES

LIST OF ABBREVIATIONS

3D	three dimensional
ABC	active breathing control
AP	anterior-posterior
ATH	adiabatic tissue homogeneity
BTV	biological target volume
CRT	conformal radiation therapy
CT	computed tomography
CT#	CT number
d-CT	dynamic computed tomography
DAC	digital to analogue converter
DRR	digitally reconstructed radiographs
EPI	electronic portal images/imaging
f-CT	functional computed tomography
fx	radiation fraction
FFT	fast Fourier transform
FOM	figure of merit
GTV	gross tumor volume
HU	Hounsfield Unit
ICRU	International Commission on Radiological Units
INF	inferior
LAT	lateral
LBF	lung blood flow
LBV	lung blood volume
MLC	multi-leaf collimators
MTT	mean tissue transit time
PTV	planning target volume
ROI	region of interest
SAD	source to axis distance
SPECT	single photon emission computed tomography
SSD	source to surface distance
SUP	superior
TBCC	Tom Baker Cancer Centre
TPS	treatment planning system
VOI	volume of interest

1. General Introduction

1.1 Radiation therapy of lung cancer

Lung cancer remains the leading cause of cancer deaths in Canada [Statistics Canada 1996]. Within the last three years, there have been modest decreases in the probability of male deaths from lung cancer (8.5 to 8.3%); however, the probability of female deaths within the same period has risen from 4.2 to 4.5%.

In the early stages of disease, some lung cancers have high control-rates via radiation and/or chemotherapy [Cox *et al.* 1986]. However, the control-rates for those diagnosed at later stages of growth are poor [Graham *et al.* 1994]. Some purported reasons for treatment failure are the variations in the radiosensitivity of different tumor sizes and types, inadequate or insufficient delivery of dose, and the deleterious effects of normal tissue irradiation.

In radiation therapy of lung tumors, multiple high-energy X-ray beams are cross-fired into the deeper lying tumor volume, resulting in a concentration of dose to the volume of interest. Through multiple beams, a high and uniform dose distribution may be delivered that not only conforms to the tumor geometry, but also avoids critical structures. The efficacy of the treatment hinges on the conformation of dose to the tumor volume since both local tumor control and normal tissue complications increase with dose.

With novel use of technology such as three-dimensional conformal therapy (3D-CRT) and intensity modulated radiation therapy (IMRT), it may be possible to increase

the dose to the tumor while still adhering to normal tissue constraints [Liebel *et al.* 1994, Armstrong *et al.* 1993, Chao *et al.* 2001]. However, the tolerance of lung tissue to radiation is still not well understood.

1.2 Lung complications in radiation therapy

Lung complications may be expressed through clinical signs such as the loss of lung function and scarring (or fibrosis) of lung tissue [Marks *et al.* 1993, Boersma *et al.* 1994, Mah *et al.* 1988]. Marks *et al.* and Boersma *et al.* both show that lung perfusion becomes significantly reduced as a result of radiation therapy. They demonstrate that the difference in single photon emission computed tomography (SPECT) signals taken before and after radiation therapy correlate with radiation dose. However, the interpretation of the difference in signal remains unclear since SPECT studies are generally non-quantitative [Marks *et al.* 1995]. Furthermore, the large image resolution of SPECT scanners, respiratory motion, and uncertainties in the registration of the SPECT and dose images decrease the quality of this complication data.

Mah *et al.* show that with computed tomography (CT), the degree of fibrosis in the lung tissue may be assessed through changes in the mean density before and after radiation therapy. Changes in mean density within the irradiated regions may increase by as much as 0.20 +/- 0.10 g/cm^3. However, the sensitivity of this technique is poor (5%) and density increases of as much as 0.20 +/- 0.09 g/cm^3 may occur within non-irradiated regions. Because of the low sensitivity, complication data generated from this data are susceptible to errors.

Positron emission tomography (PET) produces a molecularly tagged image of lung tumor cells and is quantitative. The utility of this technique to define tumor volumes is of growing interest; however, the ability of PET images to provide insight on normal tissue damage remains unclear [MacManus *et al.* 2002, Mah *et al.* 2002, Mutic *et al.* 2002].

The use of magnetic resonance imaging (MRI) and functional MRI (f-MRI) in radiation therapy is also of growing interest. F-MRI has been used to measure radiation complications in other organs such as the brain and cervix, but not in lung [Fuss *et al.* 2000, Huber *et al.* 2001,Gong *et al.* 1999]. Because the lung has a low magnetic susceptibility, the feasibility of MRI to assess radiation damage also remains unclear.

There are reports on chronic lung tissue complications in mouse lung from radiation, but there is a clear need for better in-vivo human data [Liao *et al.* 1995, Tucker *et al.* 1997].

1.3 Functional imaging

In addition to providing anatomical and structural information, imaging techniques such as Ultrasound, MRI, and CT can also provide physiological or functional information. Of all functional imaging techniques, nuclear medicine images yield the highest "functional resolution". Radioactive particles may be strategically attached to receptor molecules that either permeate cell membranes or attach to internal structures. After they permeate or attach, the particle decays and locally emits a photon(s). Despite the high functional resolution, most nuclear medicine techniques have poor spatial resolution (0.5 cm or greater) due to large detector sizes and motion

artifacts from long scanning times. Other problems include translating the intensity of signal to an absolute measure of function.

Computed tomography, which is generally known to provide anatomical information, may also provide physiological information [Miles *et al.* 1997]. This technique, called dynamic CT (d-CT), has numerous imaging protocols, but a common element shared by all is the repeated image acquisition of a volume of interest (VOI) as a high density tracer migrates through the vasculature. By quantifying the change in density in a VOI, it is possible to assess the VOI's ability to transfer the agent through, for example, the arterial blood supply to the extra-vascular space.

The change in CT Number as a function of time may be graphically analyzed to provide a quantitative measure of perfusion [Miles *et al.* 1997]. In quantitative d-CT studies, or functional CT (f-CT), this time-density data may be treated as time-series functions from which physiologically meaningful parameters or functions may be estimated. A common approach is to treat the signals as a series of independent causal-linear systems [Zierler 1965]. This type of analysis has been performed in the brain to estimate mean transit time (MTT), cerebral blood volume (CBV), cerebral blood flow (CBF) and other perfusion metrics [Axel 1980, Nabavi *et al.* 1999].

An advantage of this technique over other functional imaging methods is the linear relationship between the tracer concentration and the signal. Indicator-dilution theory and data handling methods developed for nuclear medicine techniques may be applied in f-CT without correcting for nonlinear effects inherent in MRI and Ultrasound.

Common problems associated with this imaging technique include image artifacts due to motion and re-circulation.

1.4 The use of functional CT to measure regional lung perfusion

There have been several reports on the use of f-CT to detect lung nodules with Patlak analysis. In this approach, images are periodically obtained several minutes after the contrast agent injection [Swenson *et al.* 2000, Yamashita *et al.* 1995]. However, measurements of regional lung perfusion, which require multiple images to be sampled immediately after injection, have been performed only with ultra-fast CT scanners and on canines. Wu *et al.* successfully estimated regional pulmonary perfusion with their dynamic spatial reconstructor at the Mayo Clinic in Minnesota [Wu *et al.* 1988]. Hoffman *et al.* also successfully measured regional differences in lung perfusion with their ultra-fast CT scanner in Iowa [Hoffman *et al.* 1995]. The same group in Iowa measured microvascular transit times in dog lung [Tajik *et al.* 1998]. Both groups achieved this with highly invasive animal studies, where the contrast was injected directly into the right ventricle within several seconds. Measurements of Xenon-enhanced regional lung ventilation have also been performed using a conventional CT [Gur *et al.* 1979, Herbert *et al.* 1982].

To our knowledge, there is no published work demonstrating the use of f-CT to measure regional lung perfusion with a conventional CT scanner. This may be attributable to a number of technical and physiological limitations. For example, the lung is a highly perfuse organ and exhibits rapid clearance rates of the contrast. Therefore, the contrast remains in the lung tissue for only a few seconds, making the

timing of the bolus injection and imaging critical in the protocol. Conventional CT image acquisition periods, which are typically 0.5 - 2 seconds, are as rapid as the total contrast injection period performed by Tajik *et al.* and Wu *et al.* Because the image is collected in a duration nearly equal to that of the signal, potentially ambiguous measures of the signal may result. Furthermore, artifacts caused by respiratory motion and image reconstruction may reduce the image quality. This is all compounded by low contrast enhancement within the lung due to the large air volumes.

1.5 Motivation and project hypothesis

As mentioned earlier, SPECT images taken before and after radiation therapy can provide insight on the degree of vascular damage in the lung [Marks *et al.* 1993, Boersma *et al.* 1994]. This damage may be expressed through a loss of perfusion after the course of therapy. By correlating the difference in perfusion with the delivered dose one can estimate the radiation sensitivity of the lung. This technique, however, is subject to a number of difficulties.

Several minutes are required to collect the SPECT signals. As a result, significant amounts of respiratory motion occur within the image, resulting in a blurred and time-averaged functional image. As a result, the registration between the SPECT and CT images is suspect to uncertainties. Further, potential errors may arise from the re-positioning of patient in the follow-up SPECT images, which are taken several months after the initial scans. Also, the SPECT images are qualitative. Processing methods required to convert the measured SPECT image to absolute perfusion are subject to uncertainties [Bushberg *et al.* 2001]. Last, the image resolution of the SPECT

(0.5 cm or greater) is much larger than that of the CT (typically 0.1 cm), resulting reduced precision.

The major hypothesis of this work is that a conventional CT scanner, with its inherent limitations, can be used to measure regional lung perfusion. The goal of this research is to develop a tool that can be used to obtain a better understanding of the radiation sensitivity, as expressed through the loss of perfusion, of the lung *in-vivo*. The following chapters describe theoretical work, phantom experiments, and a patient study that examines the feasibility of using a conventional CT scanner to measure regional lung perfusion. It is hoped that through the use of f-CT before and after radiation therapy, a better understanding of lung tissue damage can be obtained.

This thesis is organized as follows. Chapter 2 describes the use of a device to reduce the key issue of respiratory motion artifacts. This device may be used for both diagnostic and therapeutic purposes. Applications of this device in diagnostic imaging and radiation therapy are investigated in this work.

Lung perfusion measurements with a conventional CT scanner require rapid data acquisition from the CT scanner and a very short, but concentrated, contrast pulse. Because of this, Chapter 3 examines the fidelity of contrast concentration to CT signal. This work suggests that f-CT methods that rely on the rise-times in the time-density curves may result in erroneous perfusion estimates.

In the first section of Chapter 4, methods used in obtaining perfusion-related parameters from f-CT data are discussed. The proceeding section describes a new

technique to analyze f-CT data that exploits additional features of the f-CT image set that are often neglected.

In Chapter 5, theoretical and experimental work that examines the likelihood of obtaining a signal in the lung is described. Also, an investigation of the various CT scanning parameters that maximize the signal to noise ratio in the lung is performed. This information is then used to predict f-CT signals in the lung. Lastly, a demonstration of f-CT to measure regional lung perfusion in the lung is performed with a patient study.

Chapter 6 summarizes the main conclusions found in this thesis. This is followed by a discussion of proposed future work.

2. Evaluation of Active Breathing Control in reducing respiratory motion artifacts

This chapter describes the use of a tool that reduces respiratory motion in diagnostic imaging and radiation therapy. A study was undertaken at the Tom Baker Cancer Centre that assesses the reliability of this tool in reducing respiratory motion. While the design and rationale for this tool are in the context of radiation therapy, it may also be used in diagnostic imaging studies, such as functional CT.

Appendix A describes a clinical demonstration of this device in radiation therapy. This section is included in this thesis since it chronicles the first known use of respiratory gated radiation therapy with Active Breathing Control (ABC) in Canada. It also is the first reported use of ABC within a f-CT imaging study.

2.1 Reducing respiratory motion artifacts in diagnostic imaging

Respiratory motion may decrease the image quality of CT scans taken at or proximal to the thorax [Bushberg *et al.* 2001]. This is due to the motion of the internal and external structures during the image acquisition. To reduce these artifacts, a common approach used is to simply instruct the patient to maintain a breath-hold while the image is acquired. This 'breath-hold' technique provides a simple but efficient method for reducing respiratory motion artifacts. However, the method poses difficulties in CT exams that require several minutes; as a result, multiple breath-holds may be necessary in the exam. In this case, the reproducibility of the patient's position for each of the images taken is unreliable.

Other strategies to reduce respiratory motion in diagnostic CT include the work of Mori *et al.* (1994), who employ respiratory-gating of the CT images using a respiratory trace that triggers the image acquisition. Ritchie *et al.* (1994) utilize a predictive respiratory gating system where scanning is performed during end expiration. A more elaborate technique is to collect all the CT data as quickly as possible as can be done with ultra-fast CT scanners. Ultra-fast CT scanners can scan the entire lung volume within 200 milliseconds, thereby minimizing respiratory motion artifacts [Galvin *et al.* 1994]. These scanners are, however, costly and available in only a small number of facilities.

2.2 Reducing respiratory motion artifacts in radiation therapy

In radiation therapy, increasing the dose to the tumor results in increased tumor control. Also, increasing the dose to normal tissue results in increased normal tissue complications. Since irradiation of normal tissue is often unavoidable in radiation therapy, a balance between normal tissue damage and tumor control must be struck to achieve an optimal treatment.

In a typical treatment, a patient may take 4 to 25 breaths while a radiation beam remains on. Although the beam remains stationary, the tumor volume must always reside within the radiation field. A volumetric change in the thorax due to respiration may modify the dose delivered to the patient. Respiratory muscular contractions (such as those of the diaphragm) may cause the target and other structures to move inside and possibly outside the treatment-field. The clinical implication of this motion is that internal and external patient movements of 1 cm or greater can significantly alter the

dose distribution and, therefore, outcomes [Hobday *et al.* 1979]. If volumes allotted to accomodate respiratory motion are not included in the treatment, it may be possible to reduce normal tissue complications. Furthermore, the respiratory motion of the tumor and peripheral lung reduces the homogeneity and the mean dose the tumor receives [Brugmans *et al.* 1999]. Because of the uncertainties in lung dose, normal tissue tolerance data derived from these dose distributions are subject to further uncertainty [Emami *et al.* 1991, Basran 1997]. Eliminating the margin allotted for respiration may lead to meaningful increases in tumor dose without increasing complications [Basran 1997].

There are several methods to account for respiratory motion in radiotherapy. The conventional approach is simply to widen the beam size to ensure coverage throughout the entire respiratory cycle. Another approach is to coach the patient to hold their breath and treat in small time intervals [Ten Haken *et al.* 1997, Mah *et al.* 2000]. Yet another approach is to synchronize the radiation beam to the patient's respiratory motion with a surrogate signal, such as change in volume, diaphragm position, or CO_2 concentration [Ohara *et al.* 1989, Kubo et al 1996, Wong *et al.* 1999].

In 1999, the Tom Baker Cancer Centre acquired a prototype of the Active Breathing Control (ABC) Device from William Beaumont Memorial Hospital in Royal Oak, Michigan [Wong *et al.* 1999]. This device may be used to reduce respiratory motion in both diagnostic imaging and radiation therapy.

2.3 System description

Details of the ABC device are described in detail by Wong *et al* (1999). To summarize, there are several components, which are displayed in Figure 2-1: lap-top computer with software (1); digital to analogue converter (DAC) (2); pneumotach, scissor valve and mouth-piece assembly (3); and emergency release switch (4). The lap-top and DAC reside in the diagnostic or treatment console area while the pneumotach and emergency switch are located above the patient.

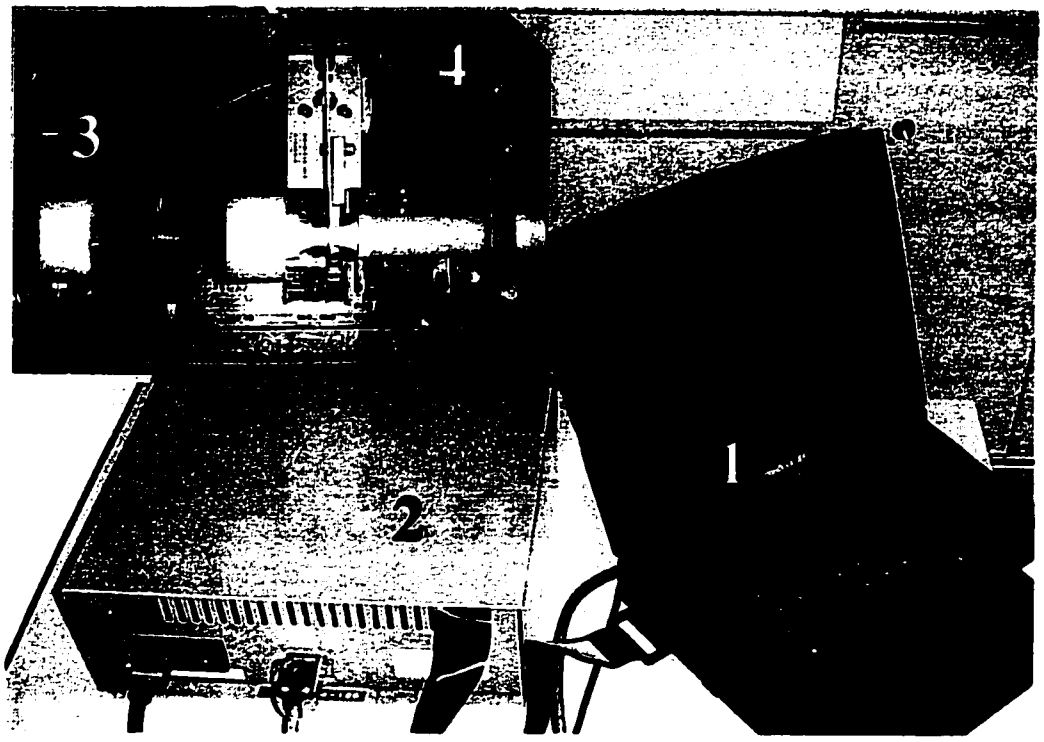

Figure 2-1: Components of the Active Breathing Control device. The laptop (1) and DAC converter (2) placed in the treatment console area, the pneumotach and mouth-piece assembly (3) placed near the patient. Note that the pneumotach and mouth-piece assembly is connected to an emergency off switch (4).

The pneumotach and DAC are connected with a 15-pin parallel port. Since most treatments are performed with the patient's arms above the head, as in Figure 2-2, a common procedure is for the patient to hold the emergency switch with one hand throughout the diagnostic exam or therapy.

A nose-clip and mouthpiece are attached to the patient and the volume of air (in litres) flowing through the pneumotach is sampled and displayed on the lap-top monitor in real-time. Once the patient is ready, the patient is instructed (via intercom) that on their next breath, the valve will close for a duration slightly less than the maximum time that they can hold their breath. The patient then inhales and the scissor valve is closed and thus constrains the volume of air inside the patient. During this time, the image is acquired or therapy is delivered. Figure 2-3 shows an ABC sequence displayed on the lap-top computer for 5 seconds while 1.0 litre of air is "contained" in the patient. The valve may be closed at some volume either at inspiration or beginning of expiration (the latter is shown in Figure 2-3).

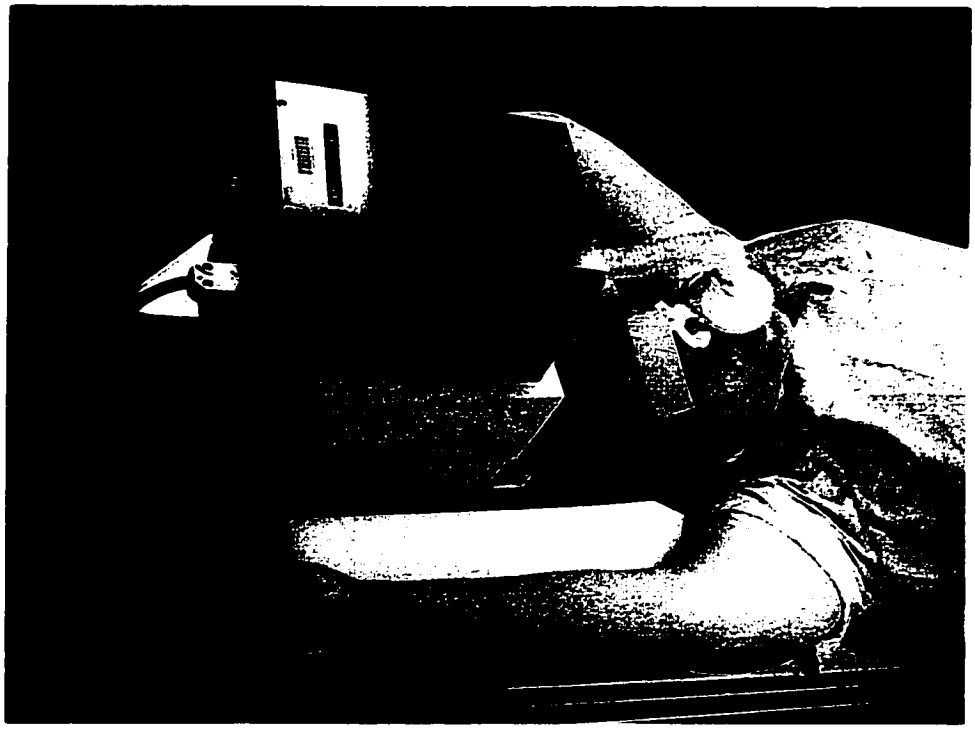

Figure 2-2: A typical patient set-up with the ABC device. Note that the emergency release valve is placed in the patient's hand.

Since it is unlikely that the patient will breathe exactly the same inhale and exhale volume in one breath, the volume trace is automatically set to zero at the end of each exhale. This is done by setting the volume signal to zero when the sign of the first derivative in the volume changes from negative to positive. Therefore, the volume signal is a measure of the air volume flowing through the pneumotach during the breathing cycle rather than the air volume contained in the lungs.

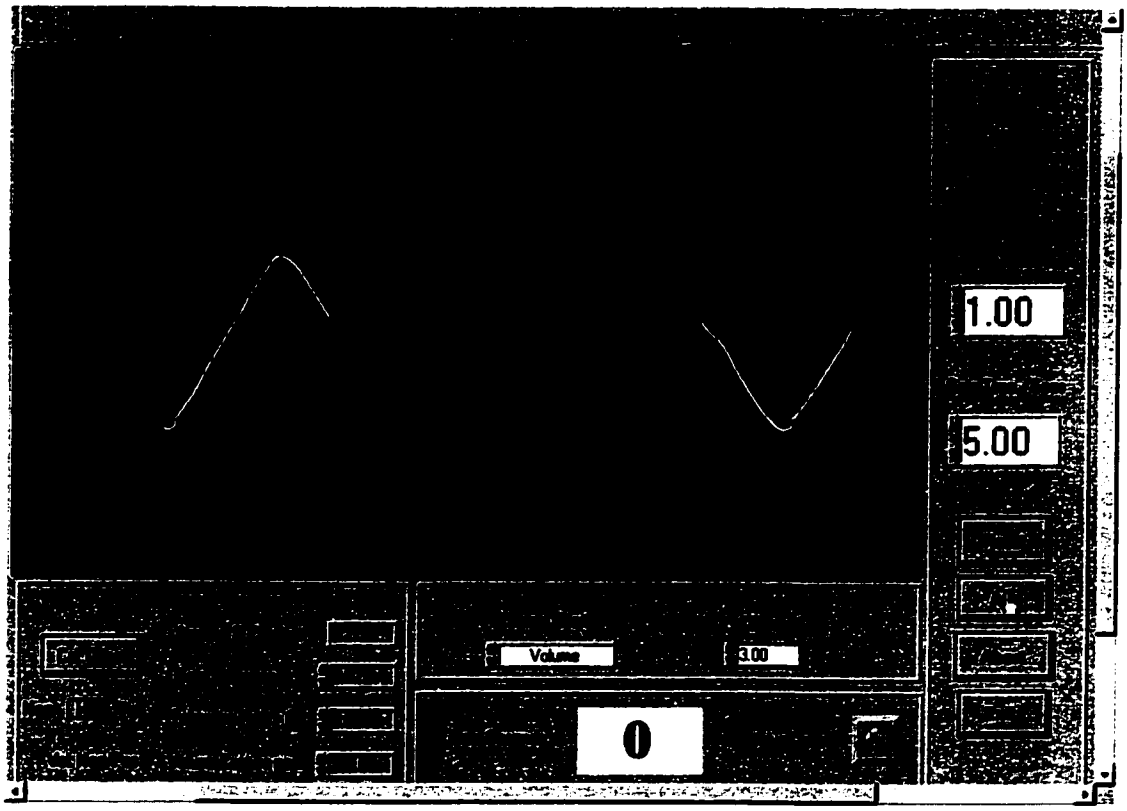

Figure 2-3: Laptop display of the ABC software. The curved line is a trace of the integrated signal of the pneumotach, and the horizontal line represents the "gating" level.

Prior to use, the electronics must be calibrated to reduce drifts in the volume measurements. Pressing the "Reset" button resets the volume signal to zero when drifting of the volume signal occurs. This drift is reduced when the ABC system is constantly on.

2.4 Methods and materials

The study population consisted of lung cancer patients at the Tom Baker Cancer Center who underwent diagnostic x-ray fluoroscopy for the purposes of radiation

therapy planning. Patients unable to maintain a breath hold at 10 seconds were excluded from the study.

The hypothesis in this study was that the ABC device can reduce the uncertainty in the position of the tumor and healthy tissue volumes for the purposes of radiation therapy or CT imaging. To this end, the purpose of this experiment was to assess the reproducibility of the diaphragm position while using the ABC device. It is assumed that if the diaphragm position is reproduced, then so are the positions of the tumor and healthy tissue. It is also assumed that the sample of patients used in this experiment does not affect the reliability of reproducing the diaphragm position.

All patients both were study subjects and acted as their own controls. In the patient's first simulation session prior to radiation therapy, two fluoroscopic images were taken to establish the amount of variability in diaphragmatic positioning during relaxed breathing (phase 1). Relaxed breathing measurements were taken at end inhale and exhale. These were the control measurements. Also during the first session, three breath-hold fluoroscopic images were taken at deep inhalation using ABC (phase 2). The maximum superior excursion point of the diaphragm was measured from a specified, fixed anatomical landmark (often an inter-vertebral space in the spinal column). The same landmark was used for all measurements taken for a given subject.

All patients received a twenty-minute consultation session prior to simulation. Eight of these patients trained on the device prior to use. The aims of session were to acquaint the patient to the device and to screen those patients who cannot tolerate the

mouthpiece or those with reduced pulmonary function (unable to hold their breath for >10 seconds).

The maximum superior aspect of the diaphragm is seen well on fluoroscopy and radiation portal images. Given that the diaphragm is the major muscle of breathing while in the supine position, the positions of organs and tumors were inferred from diaphragmatic positioning. Davies *et al.* (1994) found that the motion of the diaphragm was predominantly in the superior-inferior direction with average displacements of from 7 to 28 mm during quiet respiration. The reliability in the position of the maximum superior excursion of the diaphragm is assumed to correspond to the reliability in the position of the lungs and the tumor.

Statistical analysis was done to determine the amount of variability within the three measurements in each phase. The maximum range in the height of the diaphragm minus the minimum distance to a vertebral body was measured for each set of images. For phase 1 images, this distance (D_n) corresponded to the maximum height of the diaphragm for the normal inspiration and expiration images. For phase 2 images, the maximum distance to the dome of the diaphragm minus the minimum distance to the dome of the diaphragm with respect to the vertebral body was measured (D_{abc}). A Student's t-test between the variables D_n and D_{abc} was calculated to determine statistical significance.

The number of subjects was determined by the availability of suitable patients who agreed to participate. The projected number was set at 15 to 20. As this study had subjects acting as their own controls, and because the difference was expected to be

quite large, this number of subjects gave us a high degree of confidence in the effect of ABC in controlling the movement of breathing.

2.5 Results

A total of 17 patients were entered into the study. There were software problems with the first patient, and the data from one patient were rejected due to severe patient discomfort. Thus, data from 15 patients were analyzed.

Varis VISION software was used to determine the displacements with respect to the diaphragm [Varis Oncology Systems, Palo Alto USA]. This software automatically calibrates the image pixel sizes in a consistent coordinate system. This calibration allows the user to measure true distances rather than pixel distances while using the measuring tools available in the software. The pixel size and resolution of the simulator images were 0.9 mm or less.

Figure 2-4 shows a typical fluoroscopic image acquired during the study. The figure on the left shows the position of the diaphragm while the patient was inhaling, whereas the figure on the right shows the position of the diaphragm while exhaling. The position of an inter-vertebral space and diaphragm-dome were contoured on both images. Then, the superior aspect of the diaphragm was measured with respect to the inter-vertebral space. The difference in the distances defined the statistic D_n which, in this case, was approximately 1.5 cm.

Figure 2-4: Fluoroscopic image of an inhale (left) and exhale (right) with respect to an inter-vertebral space. The contour of both the inhale and exhale positions of the diaphragm are displayed on the right image.

The right image of Figure 2-5 shows the diaphragm contours for 3 ABC images, whereas the left image shows the diaphragm contours for normal exhale and inhale and one ABC image. For the ABC images, the same vertebral mark was contoured and the superior aspect of the diaphragm was measured with respect to the inter-vertebral space. In this example, the maximum difference in the distance defined the statistic D_{abc} which, in this case, is 0.3 cm.

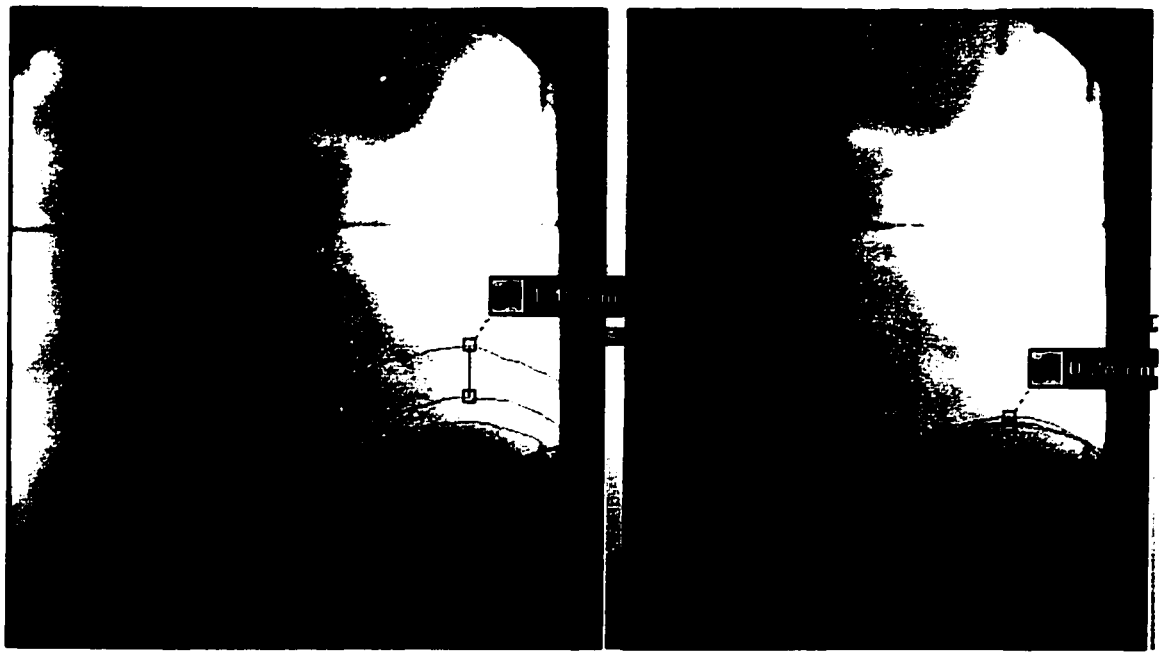

Figure 2-5: Two ABC images displaying the contours of the diaphragm. Normal inhale and exhale contours and first ABC image are displayed on the left along with a measure of D_n. The contours of the diaphragm for three ABC images are displayed on the right.

Table 2-1 summarizes the results from the test for the 15 patients. A two-tailed Student's t-test (assuming equal and unequal variances) between the population of D_n and D_{abc} was performed to assess whether D_{abc} is randomly sampled from a distribution with a mean of D_n. The t-statistic assuming equal variances was calculated as 4.03. With 14 degrees of freedom, significance at the 5 and 1% level is 2.03 and 2.78, respectively. The result was highly significant; the probability that D_{abc} is randomly sampled from a distribution with mean of D_n is less than 0.0004. There was little difference in the results of the t-test if unequal variances are assumed.

Table 2-1: Summary of results after 15 patients.

Statistic	Average Distance [cm]	Standard Deviation [cm]	Maximum [cm]	Minimum [cm]
D_n	1.7	0.8	3.0	0.6
D_{abc}	0.6	0.6	2.3	0.1

In addition to the fact that the result was highly significant, the standard deviations in D_n and D_{abc}, which represents the range in diaphragm position, was also reduced when using the ABC device.

Figure 2-6 displays a histogram plot of the D_n and D_{abc} as a function of diaphragm displacement. Most of the D_{abc} data points are less than or equal to 1 cm and clustered closer to the smaller displacements, whereas the D_n data points are more randomly spread. This would suggest further that the variation in the diaphragm position is smaller when using ABC than during normal respiration.

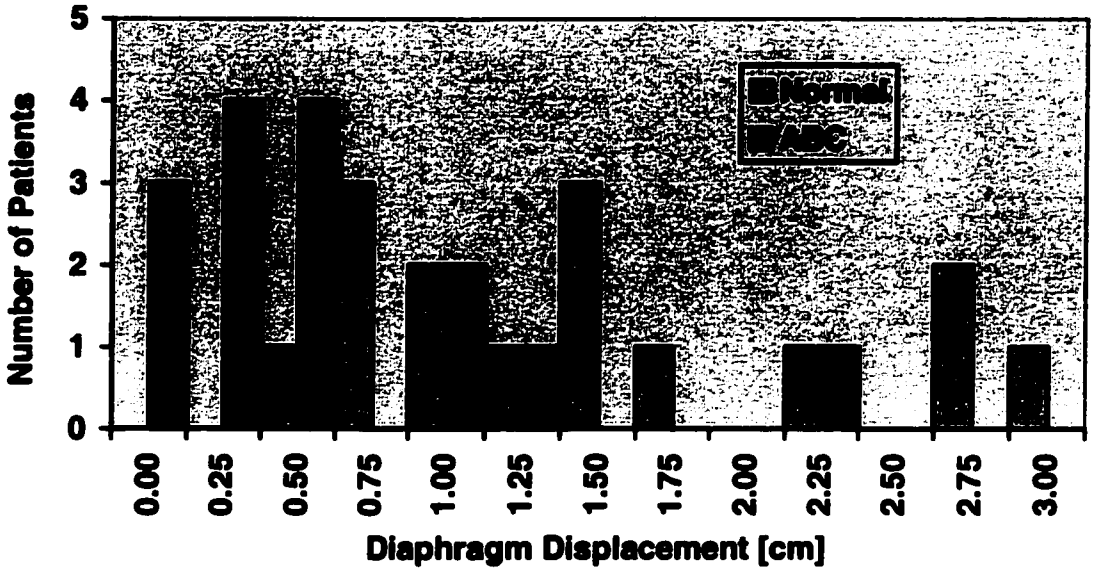

Figure 2-6: Histogram plot of the diaphragm displacements with and without ABC.

To assess inter-observer variability, diaphragm and intervertebral spaces were contoured and compared by two people (the author and thesis supervisor). Measurements of $D_n(1)$ and $D_{abc}(1)$ were compared for 11 patients and the inter-observer variability was determined to be +/- 1 mm. To assess intra-observer variability the author measured contours of 11 patients 3 times. The intra-observer variability was determined to be +/- 1 mm.

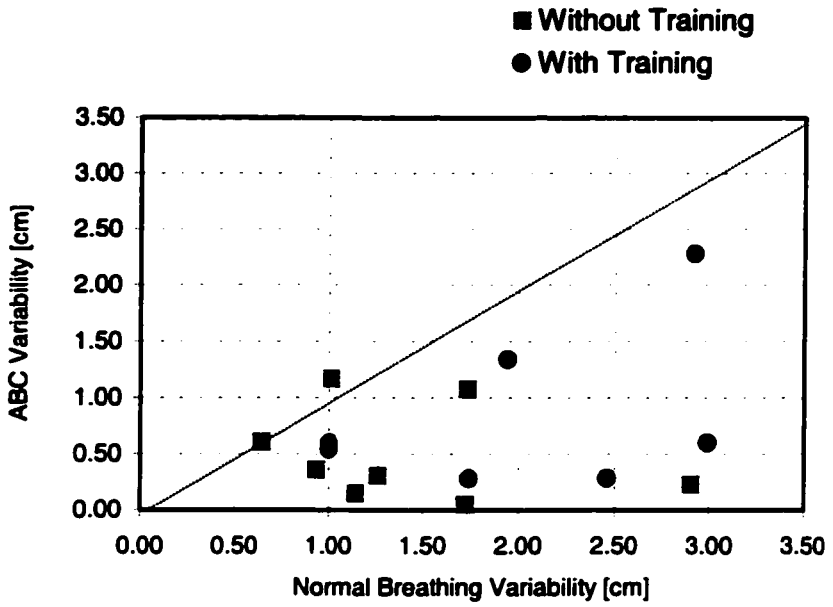

Figure 2-7: Scatter plot of D_n and D_{abc} for N=15.

Figure 2-7 displays a scatter plot that illustrates the potential benefit of using ABC. Each point represents a patient with their D_n and D_{abc} results plotted on the x- and y-axis. If the device is to have any clinical value, the ABC device must reproduce the diaphragm position with less variability than during normal breathing. If one defines the uncertainty in tumor position in non-ABC and ABC treatments as D_n and D_{abc}, the ABC device must ensure that D_{abc} is less than D_n in order to be of value.

The diagonal line on the plot represents the boundary where D_n is equal to D_{abc}. If D_{abc} is less than D_n for a patient, the data point will lie on the lower right section of the scatter plot; therefore, at most 14 of the 15 patients could benefit from ABC. Of these, one patient shows no clear advantage of using ABC and one patient has both D_{abc} and D_n

that are quite large. Of the 15 patients studied, 12 would be suitable candidates for ABC imaging and treatment. Greater clinical gains are expected for patients whose data points reside further right and lower on the scatter plot.

2.6 Discussion

The ABC device reliably reproduces the position of the diaphragm. Because of this, the use of the ABC device will improve the quality of diagnostic exams and radiation therapy. In the context of radiation therapy, planning target volumes allotted for respiratory motion can be decreased (on average) from 1.7 to 0.6 cm. This extra 1.1 cm includes significant amounts of healthy tissue and eliminating these irradiated regions may reduce the risk of pneumonitis and fibrosis [Basran 1997].

It should not be assumed that patients who use the ABC for diagnostic exams or radiation therapy are expected to have diaphragm reproducibility of 0.6 cm. This is simply because patients who have normal ranges of motion that are smaller than they are when using the ABC device would not be candidates for ABC imaging or treatment. If a statistical re-analysis were performed for those patients who would be suitable candidates for ABC imaging or treatment, D_{abc} reduces from 0.6 to 0.4 cm with a standard deviation of 0.1 cm. This statistic is a more reasonable estimate of potential diaphragm movement after fluoroscopic screening.

In his investigations, Wong reports intra-fractionation reproducibility better than 2 +/- 2 mm (N=12). Further, he reports inter-fractionation reproducibility of 4 +/- 3 mm, which is also smaller than our result. Ohara *et al.* (1989) also report millimeter reproducibility but still use a 10-15 mm margin for concerns of safety (N unknown).

Hanley *et al.* used voluntary self-breath hold gating and measured an inter-fractionation reproducibility of 1 mm (N unknown). With the exception of Ohara *et al.*, all results are much smaller than results found here. It is unclear, however, how these statistics were computed and hence, interpretation and intercomparison of results become difficult.

Not all screened patients would benefit from gated radiation therapy. Memorial Sloan Kettering in New York and Thompson Survival Cancer Center in Knoxville select patients for gated breathing if the tumor appears to move at least 1 cm due to breathing [Mageras and Ramsey 2000]. Why they have selected such a margin remains unclear. Theoretically, clinical gains may be achieved when spared margins are equal to or greater than 1.0 cm [Basran 1997]. If one uses this 1.0 cm sparing margin to screen patients receiving therapy or a diagnostic exams with ABC, only 6 patients would qualify. As expected in such a case, D_{abc} decreases to 0.3 cm.

2.7 Error analysis

Errors due to displacements within an exam or treatment are either random or systematic. During the simulation session, marks are placed on the patient for the first time: there is no opportunity for systematic error to occur unless for some reason the patient had to be repositioned on the treatment couch within the simulation session. In this study the mouthpiece was inserted after the D_n images were obtained. There exists an opportunity for displacements when inserting the mouthpiece since small amounts of patient handling and movement were required. In this study, however, surface marks were checked immediately after the mouthpiece was inserted and this motion was limited to the head and arm. Therefore, these errors are considered negligible.

A question that needs to be addressed is whether motion of the diaphragm correlates with the tumor position. Within the context of radiation therapy, the current clinical practice at the TBCC is to simply allocate a 2 cm margin on the superior and inferior aspects of the tumor volume to account for respiratory motion. This uninformed criterion could easily overestimate - and possibly underestimate - the required margin necessary to ensure the tumor is irradiated at all times. Because the diaphragm contributes 90% of the volume changes within the thorax while in the supine position, it may be safe to assume that diaphragm displacements would represent a maximum range of tumor motion in the lung. However, micro-extensions of tumor volumes may 'anchor' themselves within the lung, thus making the motion much more complex than the diaphragm itself. Motion of the tumor volume must be assessed independently from that of the diaphragm when selecting patients for treatment with ABC. This assessment may be done during the initial simulation of the patient. In short, the diaphragm motion itself should not be used as a criterion for tumor motion; the tumor motion itself must be assessed independently.

Throughout the study, it is assumed that the bony landmarks remain stationary during each of the ABC and normal breathing images. Although it is unlikely, the bony landmarks could shift during the simulation session. The magnitudes of these shifts are expected to be small, since significant changes may be detected by shifts in the body surface.

Small drifts in the electronics could have an impact on the gate volume and, therefore, the tumor position. Since the volume traces are much greater than 1 litre, and

the tolerance during a gating sequence is 0.02 litre, a 2% error in the volume may be expected during consecutive gating sequences. If one assumes, to a first approximation, that the volume of air is proportional to the diaphragm displacement and that the average displacement and volume are 1.7 cm and 1.7 litres, a 2% error in volume could result in a 0.02 cm change in diaphragm position. This displacement is not detectable.

3. Fidelity of contrast concentration with CT number

If a f-CT study is to be performed in the lung with a conventional CT scanner to measure lung perfusion, the physiology of the lung dictates that the f-CT data must be collected within a matter of seconds after the contrast injection. During the first pass the contrast passes through the intra-vascular space of the lung within several seconds. The duration of the scan must be neither longer than a single breath hold nor longer than the re-circulation period, which are both typically on the order of tens of seconds. Therefore, the width (or duration) of contrast injection must be small, potentially ranging from one to several seconds.

A fundamental assumption in all f-CT analysis is that the contrast concentration is linearly proportional to the observed CT number. Because the contrast pulse-width approaches the duration of the sampling interval in a single CT image, the fidelity of the contrast concentration to CT number becomes questionable. Further, the artifacts resulting from the time-dependent contrast flow may degrade the image quality and potentially skew the measured response functions. A more thorough analysis of the meaning of CT number (*CT#*) in the presence of highly fluctuating densities is required. These questions are addressed in this chapter.

A theoretical model of the *CT#* as a function of agent concentration and relevant CT scanning parameters is developed. Then, this model is tested in experiments. It is shown that the *CT#* is related to the agent concentration in a complex manner when the concentration is a function of space and time. These discrepancies arise primarily from

the reconstruction algorithm, finite sampling width (or slice thickness), sampling duration and velocity of the contrast through the imaging plane.

3.1 Spiral and axial CT scanning

Before these questions are examined, some background on CT image acquisition is provided. A wide variety of reconstruction algorithms are often available in commercially available CT scanners, but only two methods of reconstruction were used in this work: a standard axial and standard spiral reconstruction algorithm. No additional smoothing or additional processing methods were applied. The details of the reconstruction algorithms are not central to this thesis and can be found elsewhere [Macovski 1979].

The conventional method of obtaining volumetric CT data is in "axial" mode. Here, an image is acquired, the CT couch is translated some distance, and the image acquisition is repeated until the complete volumetric data is collected (see Figure 3-1). After each slice acquisition, algorithms can be used to reconstruct the projection data .

A more sophisticated method of obtaining an image is to collect projection data continuously while the table slowly moves through the bore of the CT scanner. This method of image acquisition is known as "spiral" or "helical" mode. The beam is continuously on until the table completes its range of motion. Once the raw projection data is collected, the user can reconstruct images at desired intervals along the couch's axis.

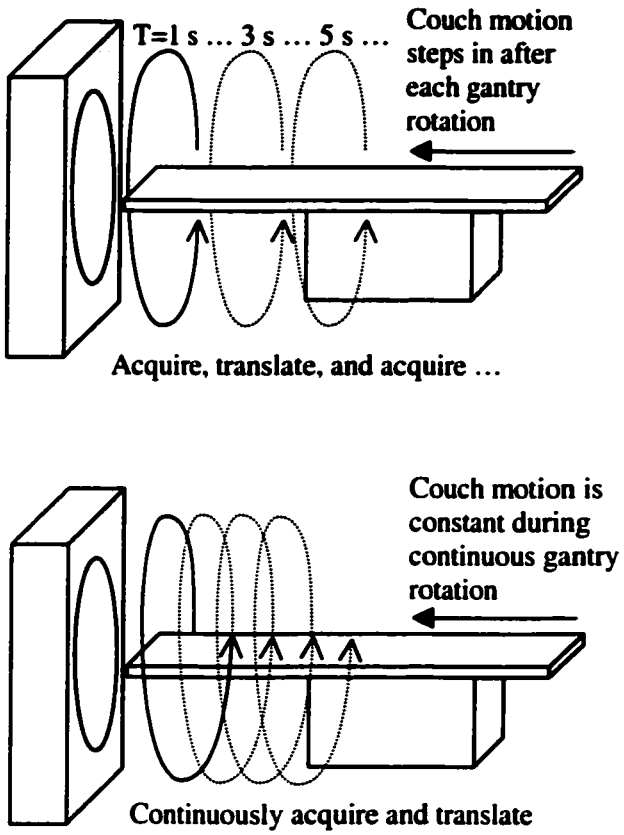

Figure 3-1: Schematic of axial and spiral mode of CT image acquisition.

In f-CT, the time-density curves are obtained by fixing the couch position such that every image is acquired in the same plane. Each point in the reconstructed image represents a data point in the time series function. One drawback of axial scanning on some scanners, such as the one in the TBCC, is that a finite time-interval (at least one second) is inserted between every 360 degree rotation, even when the couch position is fixed. In axial mode, the CT reconstruction algorithm reconstructs images immediately after each slice, rather than storing all the data into a memory buffer and reconstructing

the data set after all slices are imaged. Because the reconstruction requires a finite time, a delay in the image acquisition is required between each slice. Thus, the sampling period while in axial mode is 2 seconds. This limitation does not exist in spiral mode since the user specifies the distance between each reconstructed image.

3.2 Theory

In f-CT of the lung, high concentrations of Iodinated solution must be rapidly injected into the body, potentially introducing spatial and temporal dependencies to the linear attenuation. To better understand this, consider a voxel with dimensions (W_x, W_y, W_z) containing vessels with differing orientations and diameters. The orientations and diameters of the blood vessels within the voxel are complex and not parallel to any single surface within the voxel. Rather, the distribution of vessels within the voxel is complex or ectatic. Thus, the velocity field within the voxel depends on the blood flow flux through the 6 surfaces of the voxel. The arrows in Figure 3-2 schematically represent the mean blood flow velocities through 5 surfaces of the voxel. Assuming that the response within the voxel is independent of flow rate, the velocity of blood flow within the voxel is a function of spatial position, or $v(x,y,z)$.

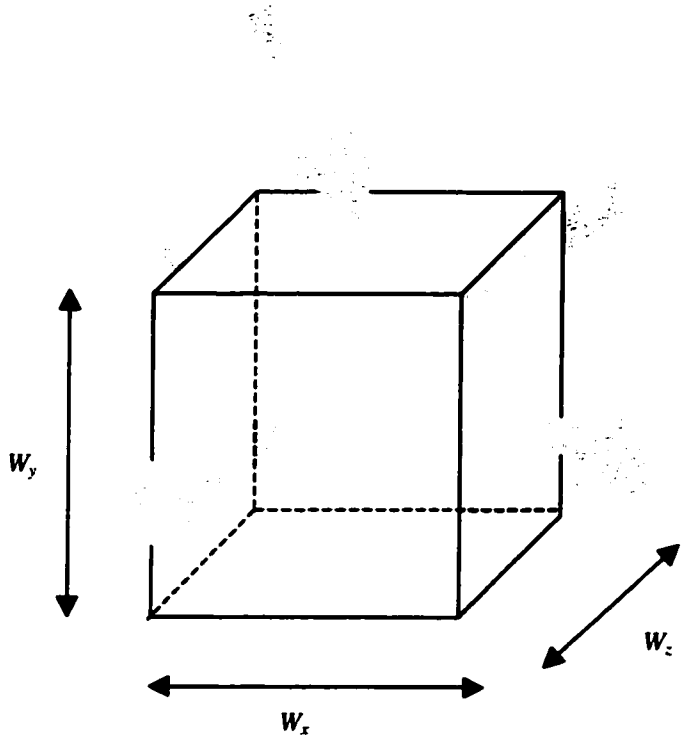

Figure 3-2: Surface flows on a single voxel.

If it is assumed that the total volume of blood entering and exiting a voxel is the same, then one can exploit mass conservation principles and arrive at the standard indicator-dilution formulas. However, employing these formulas in f-CT studies assumes that the volume of indicator entering the voxel within the image acquisition period, T_s, equals the amount of indicator leaving the same volume.

To better understand the relationship between the 'true' and 'sampled' concentration, consider the arguments described by Cottrall [Cottrall 1977]. Here, consider the simplified case of flow in one direction with the imaging plane

perpendicular to the flow (as in Figure 3-3). Generally, the true concentration, c, of a tracer is defined as:

$$c = \underset{\delta V \to 0}{Lim} \frac{\delta m}{\delta V} = \frac{dm}{dV}, \qquad \textbf{Equation 3-1}$$

where δm is the elementary mass of tracer contained in volume δV. Let the mass be a function of time, t, and distance along only the z direction. Thus, the concentration may be written as a partial derivative:

$$c(z,t) = \left(\frac{\partial m(z,t)}{\partial t} \right)_z \frac{dt}{dV} + \left(\frac{\partial m(z,t)}{\partial z} \right)_t \frac{dz}{dV}. \qquad \textbf{Equation 3-2}$$

In estimating the sampled concentration, $\bar{c}$, the volume may be defined in two ways. If it is defined as the volume of tracer passing some plane within some finite time t, then dz goes to zero. This is the case in "bucket sampling" methods, where the concentration is sampled directly by inserting a needle at the site of interest and sampling the collection of concentration at different times [Doriot *et al.* 1997]. Alternatively, if the volume is defined as the instantaneous volume over some distance, z, then dt goes to zero. This is the case in functional imaging studies performed with CT. These two definitions will generally be different unless the true concentration is constant over the volume.

In this example, assume that the true concentration can be sampled instantaneously (correction for this will be discussed shortly). The volume is defined as the volume contained instantaneously within W_x, W_y, and W_z. In this case, dt is zero and the sampled concentration, $\bar{c}$, sampled over some finite volume, ΔV, becomes:

$$\bar{c} = \frac{\int_0^{\Delta V} \left(\frac{\partial m(z,t)}{\partial z} \right)_t \frac{dz}{dV} dV}{\int_0^{\Delta V} dV}. \qquad \textbf{Equation 3-3}$$

The partial derivative in Equation 3-3 may be equally written as the instantaneous flow rate through a plane normal to the z axis, $Q(z)$, multiplied by the concentration:

$$\left(\frac{\partial m(z,t)}{\partial z} \right)_t = Q(z)\, c(z,t). \qquad \textbf{Equation 3-4}$$

Note also that the inverse of dz/dV defines the normal surface, S, that the contrast passes through:

$$\frac{1}{\frac{dz}{dV}} = S. \qquad \textbf{Equation 3-5}$$

But the velocity of the contrast $v(z)$ may be defined as:

$$\frac{Q(z)}{S} = v(z). \qquad \textbf{Equation 3-6}$$

This gives us the expression given by Doriot *et al.*,

$$\bar{c}(t) = \frac{\int v(z)c(z,t)\, dz}{\int dz}, \qquad \textbf{Equation 3-7}$$

for the sampled concentration in a CT study [Doriot *et al.* 1997]. In CT, the volume integral spans over some finite slice thickness W_z, so Equation 3-7 is simply:

$$\bar{c}(t) = \frac{1}{W_z} \int v(z)c(z,t)\, dz. \qquad \textbf{Equation 3-8}$$

Equation 3-8 describes the sampled concentration based on the true concentration as a function of space. However, unless the concentration curve can be

sampled in a time interval less than the time required for the contrast to pass through the voxel, the f-CT signal will measure some average concentration over the scan time ΔT_s. When the velocity of the concentration is v_z, the concentration curve will travel a distance equal to $v_z \delta t$ in some small time interval δt (see Figure 3-3). In the scan period ΔT_s, the concentration curve will traverse a distance equal to $v_z \Delta T_s$, resulting in a "time-averaged" concentration curve.

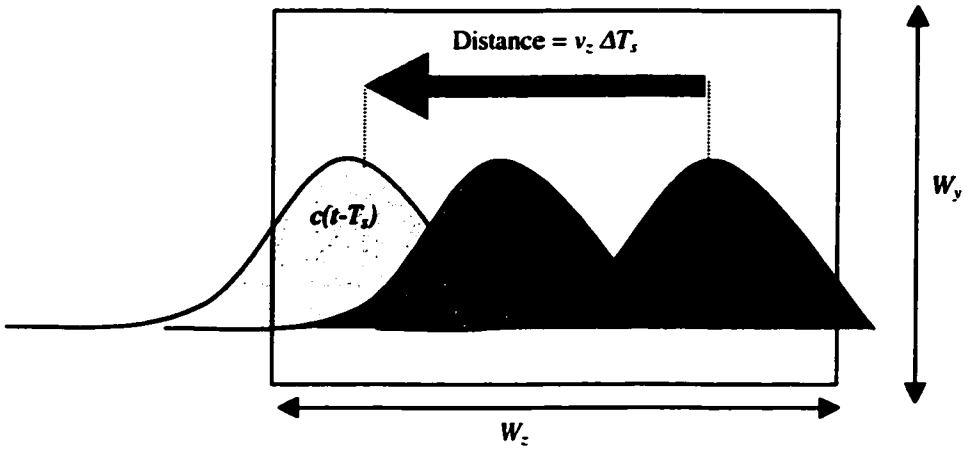

Figure 3-3: Temporal and spatial averaging of the moving concentration curve *c(t)*. The *x* dimension points into the page.

As ΔT_s approaches zero, the time-averaged concentration curve will equal the sampled concentration curve, or generally:

$$\bar{c}(t) = \frac{1}{W_z \Delta T_s} \int_0^{\Delta T_s} \iint v(z) c(z, t-\tau)\, dV d\tau \xrightarrow{\lim \Delta T_s \to 0} \frac{1}{W_z} \int v(z) c(z,t)\, dV \quad \textbf{Equation 3-9}$$

Thus, if there are significant variations of the concentration during the sampling period, the limit of ΔT_s does not approach zero and the left side of Equation 3-9 must be used.

3.3 Methods and materials

3.3.1 Linearity of concentration and CT number

In a f-CT study, the *CT#* is often assumed to be proportional to the contrast concentration. However, attenuation of lower energy x-rays in high-density materials may result in spectral changes (or beam hardening) in the CT beam, which may alter the estimate of *CT#*. The result is that the assumption of linearity between contrast concentration and *CT#* may break down, making the quantitative analysis of the f-CT study difficult.

To investigate the validity of this assumption, twelve vials of varying Iodinated contrast were created and scanned. Various amounts of distilled water and 300 mgI/ml Iohexol were mixed to an error less than 2%. The manufacturer specifications on error could not be found. The concentrations were roughly logarithmic in concentration steps, ranging from 300 mgI/ml to 0.150 mgI/ml (see Table 3-1). Each mixture was carefully prepared with 1% resolution syringes and syringes were discarded after use to reduce contamination. For example, 50 ml of water plus 50 ml of Iohexol results in a 150 mgI/ml solution. After preparation, the solutions were placed in vials of a 1.0 cm diameter acrylic cylinder of approximately 15 cm length.

Concentration [mgI/ml]	Error [+/- mgI/ml]
300.0	-
150.0	3.0
75.0	1.5
37.50	0.75
18.75	0.38
9.30	0.10
4.72	0.05
2.38	0.02
1.20	0.01
0.599	0.006
0.300	0.003
0.150	0.002

Table 3-1: Concentrations (and errors) used in experiment.

To estimate the linear attenuation of a vial with some known contrast concentration, assume a well-mixed solution of the contrast (i) and blood (b). The mass attenuation coefficient (μ/ρ) of the mixture (mix) may be given as:

$$(\mu/\rho)_{mix} = f_i(\mu/\rho)_i + (1-f_i)(\mu/\rho)_b, \qquad \textbf{Equation 3-10}$$

where f_i is the fraction (by mass) of Iodine in the solution, and ρ is the density [Johns *et al.* 1983]. The fraction by mass of Iodine is:

$$f_i = m_i / (V \rho_{mix}) = c_i / \rho_{mix} , \qquad \textbf{Equation 3-11}$$

where c_i is the Iodine concentration. Combining Equation 3-10 and 3-11, one gets:

$$(\mu/\rho)_{mix} = (c_i / \rho_{mix})[(\mu/\rho)_i - (\mu/\rho)_b] + (\mu/\rho)_b . \qquad \textbf{Equation 3-12}$$

Note that:

$$\rho_{mix} = \text{ Mass / Volume } = (m_i + m_b) / V = c_i + c_b . \qquad \textbf{Equation 3-13}$$

Thus, simplifying Equation 3-12 for the linear attenuation of the mixture, one has:

$$\mu_{mix} = c_i (\mu/\rho)_i + c_b (\mu/\rho)_b . \qquad \textbf{Equation 3-14}$$

Equation 3-14 implies that the linear attenuation of the Iodine and blood mixture is a linear function of the concentration of Iodine and the blood concentration. In experimental conditions where the CT beam consists of a spectrum of energies, the linear attenuation is averaged over the spectrum of energies, which results in an "effective" linear attenuation. The *CT#* is simply the ratio of linear attenuations with respect to water:

$$CT\# = 1000\left(\frac{\mu_{mix} - \mu_{water}}{\mu_{water}} \right). \qquad \textbf{Equation 3-15}$$

As an estimate of the relative amounts of attenuation expected in the 300 mgI/ml vial, one can use the expression:

$$N = N_o e^{-\mu t}, \qquad \textbf{Equation 3-16}$$

where N and N_o is the exit and entrance photon fluence, μ is the estimated linear attenuation value using a monoenergetic approximation, and t is the thickness of the attenuator. Figure 3-4 displays the relative transmission as a function of contrast thickness.

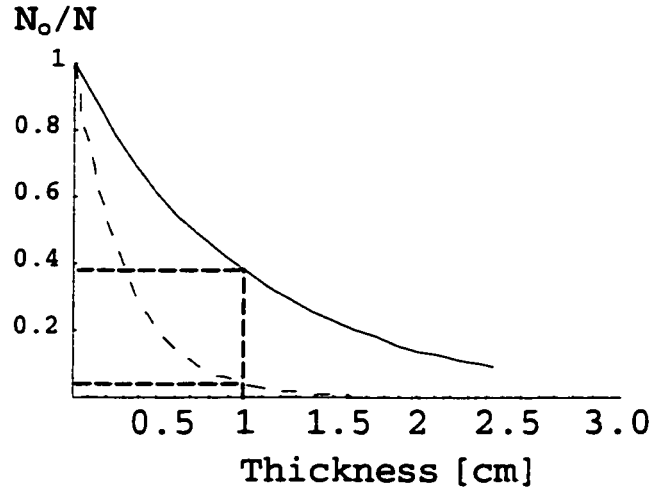

Figure 3-4: Estimates of the relative transmission as a function of thickness. The vial diameter in this experiment is 1.0 cm. The dashed and solid lines display the transmission for 300 and 0.15 mgI/ml concentrations.

As displayed in Figure 3-4, significant amounts of attenuation in the 1 cm vial (40% and 8%) are expected from the 300 and 0.15 mgI/ml concentrations, respectively. Therefore, from Equation 3-15, large changes in *CT#* are expected when contrasted against a uniform background.

A Marconi ACQSIM CT scanner was used to measure the *CT#* in the vials while in axial mode and using slice thicknesses of 0.5 and 1.0 cm [Marconi Medical Systems, Essex UK]. Two energy (kVp) settings, 100 and 120 kVp were used in this study.

Two regions of interest were defined within the vials: a large 13 mm^2 circle and a smaller 7 mm^2 circle. These areas were used as they represent the typical size of

elements used in f-CT analysis. The mean *CT#* along with its standard deviation were recorded within the vials in and out of the phantom.

3.3.2 Theoretical examination of concentration and CT number

The contrast concentration curves in f-CT signals are continuous functions in space and time. But as discussed in Section 3.2, sampling periods and volumes in conventional CT are discrete and finite. Therefore, the true concentration curve may differ from the measured one due to the integrative processes of the CT image acquisition and reconstruction.

To examine these potential differences more closely, consider a normalized gaussian curve with width, s, traveling with a constant velocity, v_z along the z'-axis, much like that described in Figure 3-3. Assume that this curve retains its shape for all time, or is non-dispersive.

In spatial coordinates, the gaussian function is:

$$g(z') = \frac{1}{\sqrt{2\pi s^2}} e^{\left(\frac{z'^2}{2s^2}\right)}. \qquad \textbf{Equation 3-17}$$

If the pulse is moving with some velocity v_z with respect to time, z' can be replaced with $z-v_z t$. One can now describe the time-dependent concentration by combining the left side of Equations 3-9 and Equation 3-17:

$$\bar{c}(t) = \frac{v_z}{W_z T_s} \int_0^{T_s} \int_0^{W_z} \omega(z) \frac{1}{\sqrt{2\pi s^2}} e^{\left(\frac{(z - v_z(t-\tau))^2}{2s^2}\right)} dz d\tau. \qquad \textbf{Equation 3-18}$$

Note here that an extra factor $\omega(z)$ is included to account for the fact that the measured signal intensity is not constant in the imaging plane. Instead, there is a non-

uniform slice sensitivity profile that weights the measured signals as a function of z [Brooks *et al.* 1977]. For theoretical simulations, $\omega(z)$ is set to a constant but during measurements, $\omega(z)$ can be easily measured and modeled. Ignoring slice sensitivity profile, the sampled concentration is:

$$\bar{c}(t)=\frac{v_z}{W_z T_s}\int_0^{T_s}\int_0^{W_z}\frac{1}{\sqrt{2\pi s^2}}e^{\left(\frac{(z-v_z(t-\tau))^2}{2s^2}\right)}dzd\tau, \qquad \textbf{Equation 3-19}$$

where W_z is the slice thickness. With this equation, the effects of various slice thicknesses, scanning times, velocities, and pulse widths, on the true gaussian pulse can be compared. Simulations were also performed for gamma variate curves with form:

$$c(t)=t^{\beta}e^{-\alpha t}, \qquad \textbf{Equation 3-20}$$

where α and β are real numbers, but are excluded here since the results are very similar to those found for the gaussian curves.

The range in velocities depends primarily on the physiology of the human lung. Shown in Table 3-2 are velocities of relevant vessels in this work [Fung 1997]. In these simulations, a wide variety of velocities and pulse widths were simulated. Because a first-pass study is to be delivered, pulse-widths that ranged from 1 to 60 seconds were simulated. Slice thickness of 0.1 to 1.0 cm and sampling periods from 0.1 to 2.0 seconds were simulated, corresponding to the slice thicknesses and sampling periods of both ultra-fast and conventional CT scanners.

	Velocity (cm/s)	
Vessel	**Range**	**Mean**
Ascending Aorta	40-250	120
Pulmonary Artery	*NA*	70
Small Vessels	0.5-1.0	0.75
Capillaries	0.02-0.17	0.07
Vena Cava	15-40	25

Table 3-2: Range and mean velocities of blood in canines (taken from Fung 1997).

3.3.3 Experimental examination

To examine the effects of spatial and temporal averaging during a CT image acquisition, a phantom experiment of a known time-density curve was scanned and compared against the measured one. A cylindrical water phantom (see Figure 3-5, and Figure 3-6) and a rod containing small cylinders of contrast of various concentrations ranging from 150 mgI/ml to water (as in Table 3-1) was constructed. The rod was fed through the bore of the water phantom at 4.0, and 8.0 cm/s during the image acquisition, mimicking the blood flow in a small artery. The CT images were collected using spiral acquisition with 120 kVp, 300 mA, 0.5 cm slice thickness, and employing a standard reconstruction algorithm.

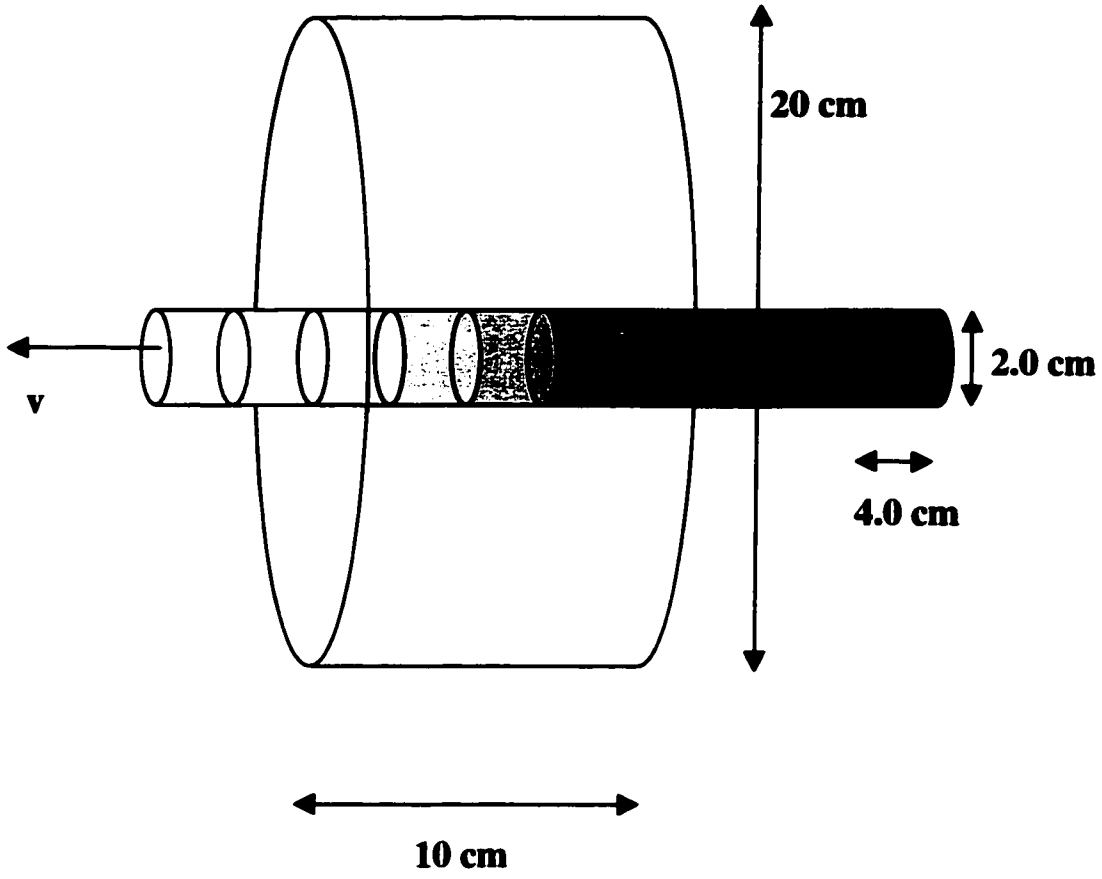

Figure 3-5: Phantom experiment of dynamic CT signal.

Static axial scans were performed on the individual vials to construct the 'true' time-density curve as a function of space and time. Since each image is acquired in one second, the true time-density curve is simply a ladder function of the measured axial scan CT values as a function of distance. A DC motor was calibrated to produce various linear velocities by varying the voltage level and using different gear ratios in order to pull the rod through the phantom. The phantom was then imaged in spiral mode using 0.5 cm slice thicknesses and reconstructing images every 0.5 second.

Computer simulations were then performed to estimate the observed *CT#* using the 'true' time-density function. The *CT#* in the rod was measured and compared against the 'true' and expected (averaged) function. The slice sensitivity profile was measured, fit with a gaussian curve and used as an input to the model [Brooks *et al.* 1977, Polacin *et al.* 1992].

Figure 3-6: Image of phantom geometry. The small cylinders were color-coded with green dye to visually identify the variations in density.

3.3.4 Effects of time-dependent signals external to vessels

The change in concentration during the image acquisition not only affects the value of *CT#* in the vessel, it may also affect the value of *CT#* peripherally [Berninger *et al.* 1979]. The reason for these artifacts is that the projection data contains mixed information of the rod's central density. As a consequence, the reconstruction algorithm may incorrectly estimate the *CT#* not only inside, but also outside the central rod.

In a simple experiment, Berninger and Redington measured these artifacts by passing a high-density object through a tube and measuring the subsequent change in *CT#* in the surrounding water phantom [Berninger *et al.* 1979]. They found that in addition to inaccurate estimates of *CT#* in the vessel, streaking artifacts bloomed from the vessel, perturbing the *CT#* in the surrounding water. This study was limited to a single "plug-flow" bolus, where the density was immediately doubled during the image acquisition.

This doubling in *CT#* is not typically observed in f-CT studies. Rather, there is a rapid increase and then gradual decrease in *CT#*. A "plug-flow" distribution may be relevant in angiography, where the bolus is administered directly adjacent to the vessel of interest. However, deliveries of contrast at a more distal injection site result in smooth time-density curves, similar in shape to gamma-variate functions [Thompson *et al.* 1964, Miles *et al.* 1997].

In many f-CT studies, these blooming artifacts may mask pathologic conditions [Rubin *et al.* 1995]. A number of authors have overcome this difficulty by reducing the injection concentration and using prolonged injection rates [Rubin *et al.* 1995, Costello

et al. 1992]. It remains unclear as to whether these artifacts are due to beam hardening in the high-density contrast or from the reconstruction of the time-varying signal.

To investigate the effects of these artifacts adjacent to the input vessel, the *CT#*s were measured in the water adjacent to the central rod in the previous experiment when the rod velocity was 4 cm/s. The scanning protocol was the same as that described in the previous experiment. To assess whether these artifacts are due to overly attenuated photons in the high-density contrast or due to the time-dependent signal, comparisons of the above values to those found in axial images of the rods at different concentrations were performed.

3.4 Results

3.4.1 Linearity of concentration and CT number

The lower kVp settings resulted in a higher slope in the concentration versus *CT#* relationship. Figure 3-7 displays the *CT#* vs. concentration plots using a 1.0 cm slice thickness, 300 mA, with 0.7 s scanning time. The concentration becomes indistinguishable at a concentration of 0.300 mgI/ml, where the errors in the *CT#* for the concentration overlap with that of the control's (water) error. The data suggest that the assumption of linearity is valid between concentrations of 0.300 mgI/ml to approximately 75 mgI/ml.

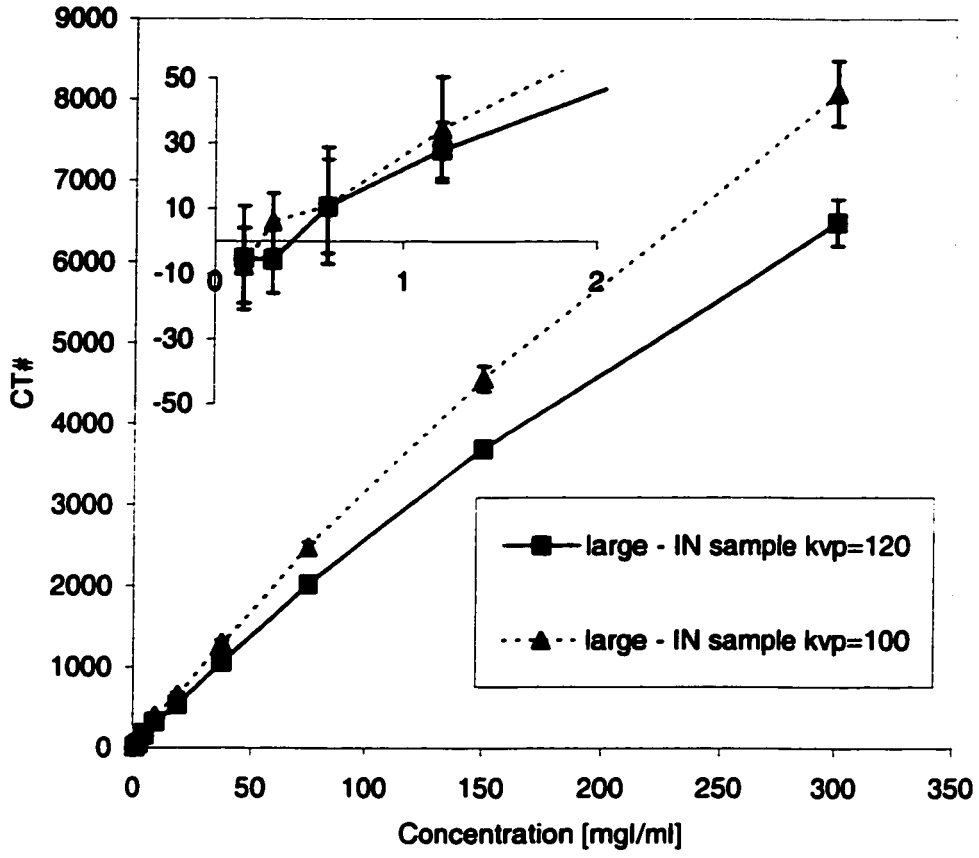

Figure 3-7: Linearity of *CT#* and contrast concentration for 100 and 120 kVp.

Figure 3-8 displays a log-log plot similar to Figure 3-7 but displaying the results for 120 kVp with slice thickness of 0.5 and 1.0 cm. Also shown are linear regressions using a least-squares fit along with the correlation coefficients. Both fits are highly linear and only distinguishable from the measured data in a log-log plot that amplifies small differences in linearity.

Both graphs would suggest that *CT#* and concentration are highly linear for uniform concentrations of Iodine less than 75 mgI/ml.

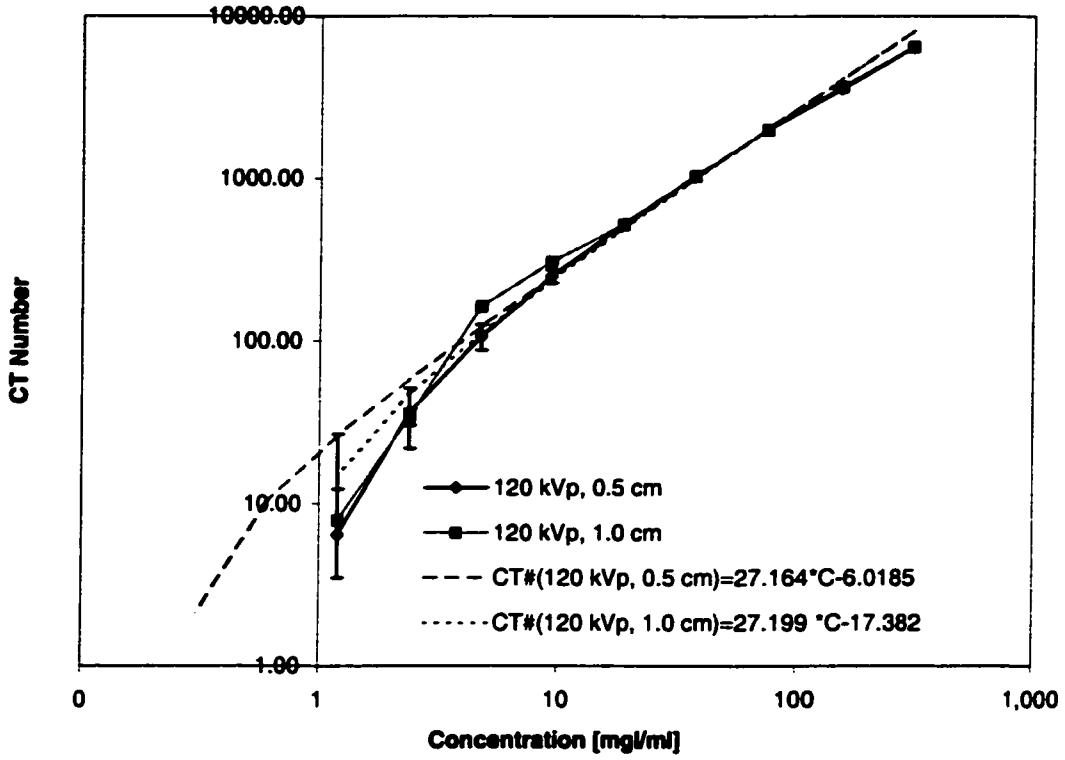

Figure 3-8: *CT#* versus concentration for two different slice thicknesses.

Figure 3-8 also suggests that this linearity does not depend on the slice thickness when the vials do not change as a function of time. For concentrations higher than 75 mgI/ml, the linearity begins to fail.

The reason for this loss of linearity may be from beam hardening within the cylinder. Higher concentrations of Iodine effectively filter lower energies of the x-ray beam's spectrum, making it more penetrating. As a result the mean attenuation of the Iodine decreases. Note also that photon detection is a Poisson process; therefore, the noise in these regions increases, illustrated by the increased magnitude of error for the higher concentrations in Figure 3-7.

3.4.2 Estimation of CT number with time-dependent signals

Shown in Figures 3-9 to 3-15 are the "true" versus "sampled" concentration, or *CT#* (assuming concentration and *CT#* are linear). Note that for the simulations shown here that the "true" signal is identical from the 0.1 second sampling signal for realizable velocities and pulse widths. When interpreting these images, it is important to note that with the given scanning parameters, a single point on the curve becomes the sampled *CT#*. Although the curves are continuous, each measured point is separated by the sampling period. Thus, if one were to repeat a measurement with the given parameters at slightly different start times, one eventually generates the continuous curve.

Shown in Figure 3-9A-C are the sampled *CT#*s when the slice thickness increases from 0.1 to 0.5 and to 1.0 cm. Here, the pulse-width is 5 seconds, which is on the order of expected pulse widths in a f-CT study. The velocity is fixed at 1.0 cm/s, which simulates blood flow in small arteries. Figures 3-9A-C illustrate that the width of the concentration curve remains relatively the same as the slice thickness increases from 0.1 to 1.0 cm. This suggests that with typical CT scanning periods, partial-volume averaging due to finite slice thickness is less important when sampling smaller arteries. Note also that it requires approximately 30 seconds of sampling to observe the curve with these parameters. This makes sense since 99 % of the gaussian pulse width ($2x3\sigma$) travels approximately 30 cm at a rate of 1 cm/s.

A

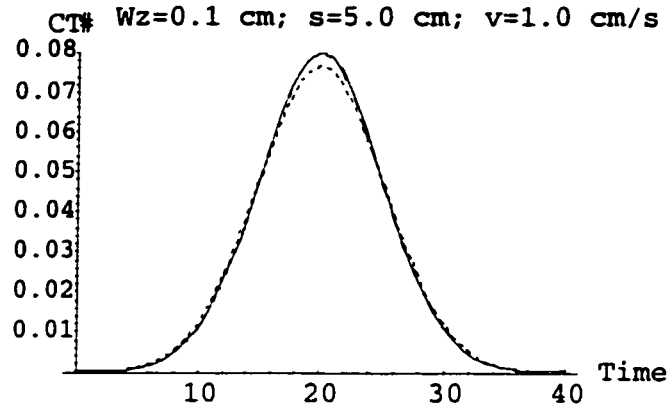

B

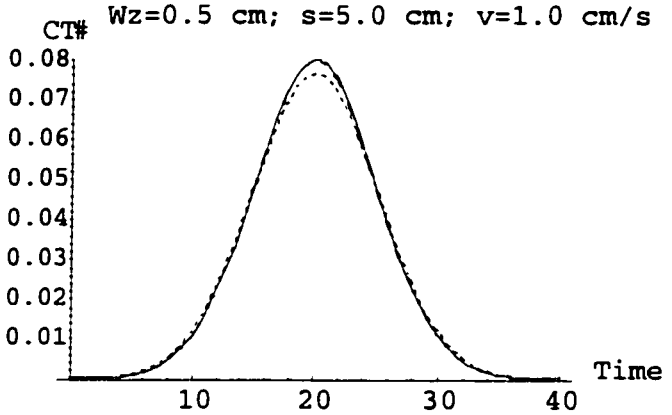

C

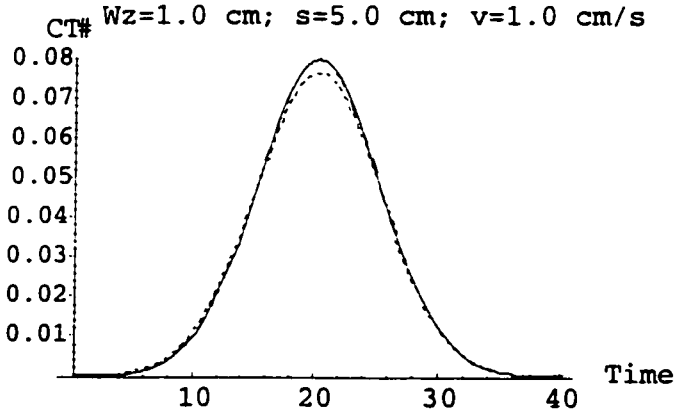

Figure 3-9A-C: Sampled CT signals from gaussian input function for different slice thicknesses. Shown are the true (solid) curve, and T_s=1.0s (large dash), and T_s=5.0s (small dash).

Consider keeping the velocity constant and changing the pulse width from 5.0 to 0.1, 1.0 and 20 cm (Figure 3-10A,B,C, respectively). One can see that the sampled signals can be quite different when scan times are also different. Consider Figure 3-10A. With the pulse width of less than 1 second, one would expect the window of observation to be very small, especially since the curve travels through the scanning plane within a second. Figure 3-10A suggests that the measured *CT#* 'smears' the true *CT#* (displayed in solid). Even though the pulse shape is very narrow, the sampled *CT#* will be quite broad. Note also how the magnitude of the sampled *CT#* also changes within Figure 3-10A. Remember that the magnitude of the *CT#* are relative to the "true" *CT#*. This would suggest that for very small pulses, high precision in both the spatial and temporal domain are required.

For longer pulse widths, shown in Figure 3-10B and 3-10C, the sampled *CT#* remains relatively the same for all sampling durations. Because the pulses are much longer, the magnitudes are obviously smaller and the time required to sample the curves are much longer. Intuitively, one would expect 99 % of the gaussian pulse width ($2x3\sigma$) to be sampled over approximately 0.6, 60, and 120 cm, at a rate of 1 cm/s (which is indeed the case here). This suggests that for blood flow in small arteries, the scanning duration is independent of the pulse width when the pulse width is greater than the minimum scan time.

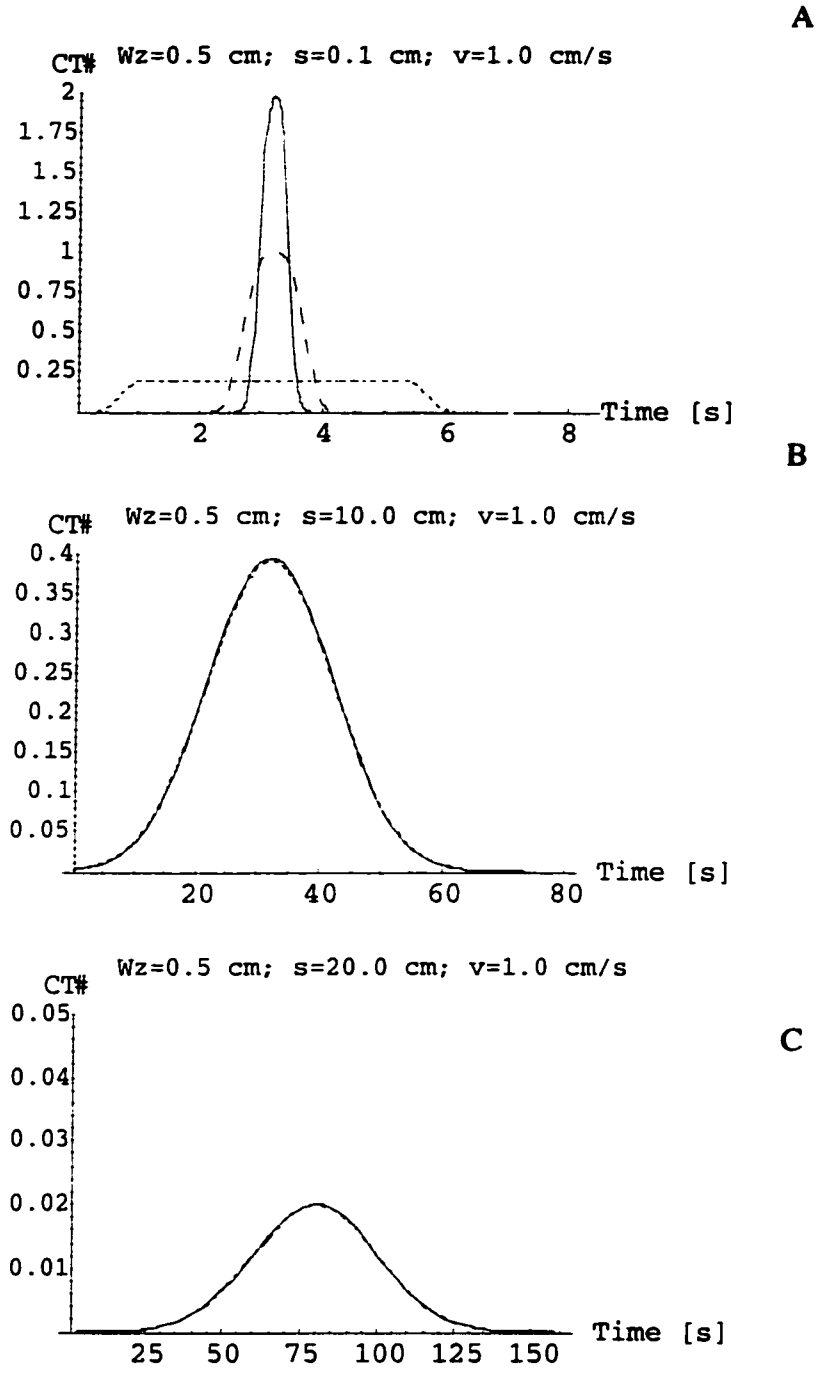

Figure 3-10A-C: Sampled CT signals from gaussian input function for different pulse widths. Shown are the sampled signals when T_s is 0.1 seconds (solid), 1.0s (large dash), and 5.0s (small dash).

Now, consider keeping a small pulse width of 1.0 s and varying the velocity from 1.0 cm/s to 0.01, 0.1 and 10.0 cm/s (Figures 3-11A,B,C, respectively). When the velocity is very slow, such as in the micro-vasculature, as in Figure 3-11A and 3-11B, the sampled *CT#* is independent of scan time, even with a 1.0 second pulse. However, when the velocity is 10 cm/s, such as in perhaps some veins, the sampled *CT#* is not independent of the scan duration. Because the pulse size remains the same and the velocity increases, one would expect the observed concentration curve to exhibit greater 'peakedness' as the velocity increases. This peakedness is observed when the scan times are generally small; however, when the scan times increase from milliseconds to the order of seconds, the sampled *CT#* is much broader than the true concentration curve.

These figures would suggest that the relationship between *CT#* and concentration depends on the velocity and pulse-width of the signal, as well as the scan duration. Since the exact value of velocity is not known during a f-CT study, the loss of fidelity between concentration and *CT#* may result in errors in quantitative analysis.

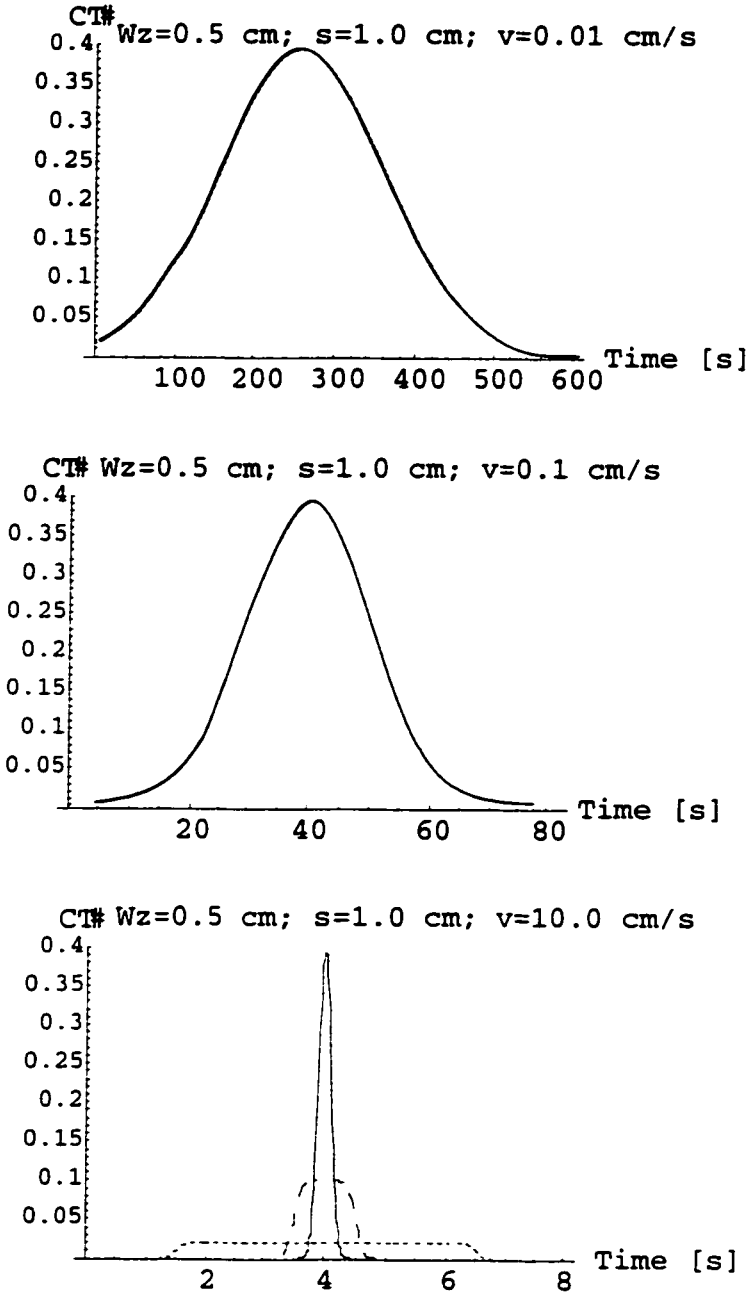

Figure 3-11A-C: Sampled CT signals from gaussian input function for different velocities. Shown are the true (solid) curve, and T_s=1.0s (large dash), and T_s=5.0s (small dash).

To put the magnitude of these discrepancies into perspective, consider more clinically relevant blood-flow velocities and more realistic scanning parameters. Figures 3-12 to 3-16 display the sampled *CT#*s for a more realistic scan duration and slice thickness, with velocities of 250, 70, 20, 0.7, and 0.07 cm/s. For the aorta and pulmonary vessels the measured *CT#* becomes broadened, whereas in the smaller vessels the measured and actual signals are closely approximated.

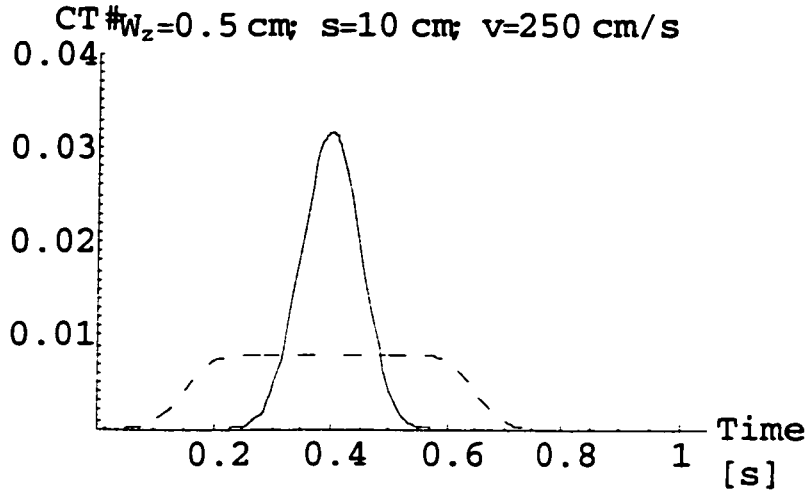

Figure 3-12: Sampled CT signals for the aorta. Shown are the true (solid) curve, and T_s=0.5 s (large dash).

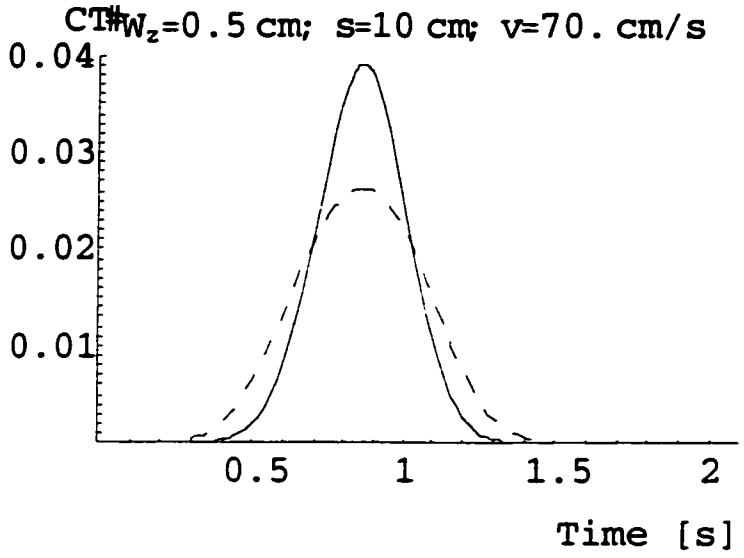

Figure 3-13: Sampled CT signals for the pulmonary artery. Shown are the true (solid) curve, and T_s=0.5 s (large dash).

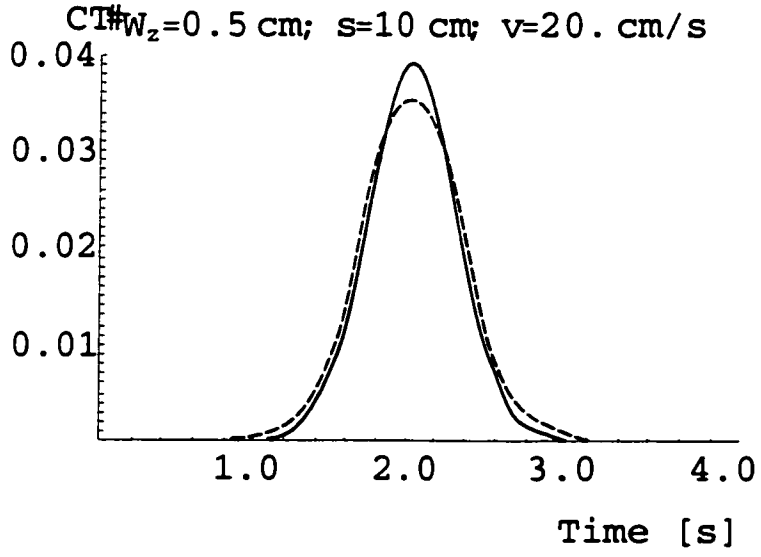

Figure 3-14: Sampled CT signals for a smaller vessel. Shown are the true (solid) curve, and T_s=0.5 s (large dash).

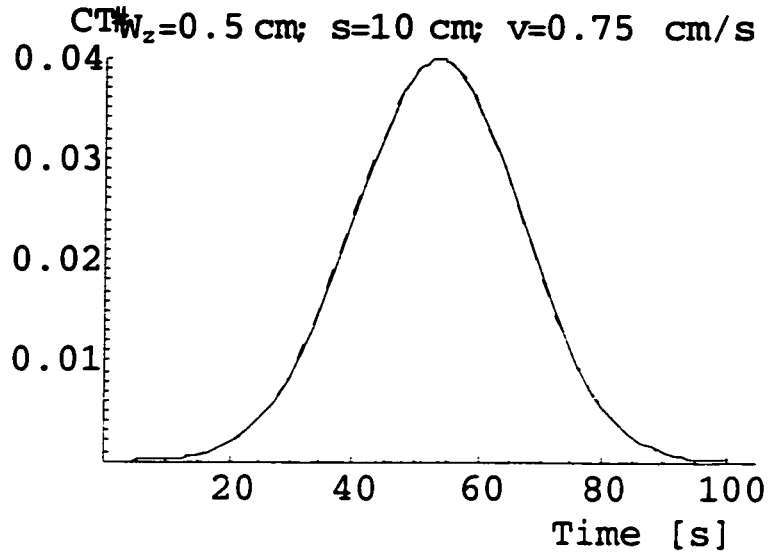

Figure 3-15: Sampled CT signals for the small vessels. Shown are the true (solid) curve, and T_s=0.5 s (large dash).

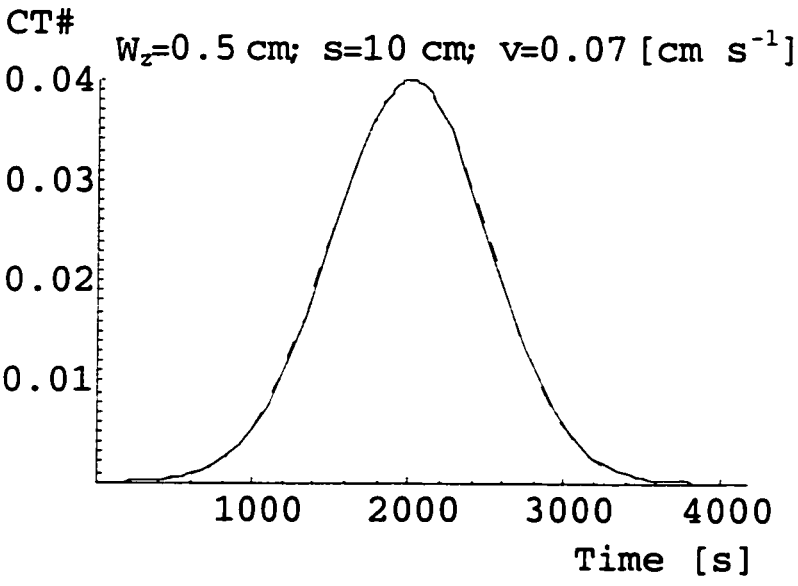

Figure 3-16: Sampled CT signals in the capillaries. Shown are the true (solid) curve, and T_s=0.5 s (large dash).

If it is assumed that the mean velocity of blood flow through the imaging plane approximates the mean velocity of blood within the CT volume, then these simulations suggest that the measured and true concentration curves through the imaging plane are approximately equal. However, in the larger vessels, this does not appear to be the case. In fact, in regions where the blood flow velocity is approximately 70 cm/s or greater, the true and measured *CT#*s are different. This may have implications in studies involving the heart when measuring ejection-fraction [Wolfkiel *et al.* 1987].

3.4.3 Experimental validation

Figure 3-17 illustrates the experimentally measured *CT#* and the effects of time and spatial averaging for a rod moving at 4 cm/s. The measured signal was obtained in spiral mode and reconstructed the image at 0.2 second time intervals. The dashed line indicates the input function as defined from axial slices of the different vials of the time-density curve. Convolving this with the SSP and then performing the time-averaging results in a final *CT#* illustrated in the dark circles. The value of T_s used is equal to one half-second since the images were acquired in spiral mode using half-scan interpolation [Crawford *et al.* 1990]. A similar result is found with velocity of 8 cm/s, shown in Figure 3-18.

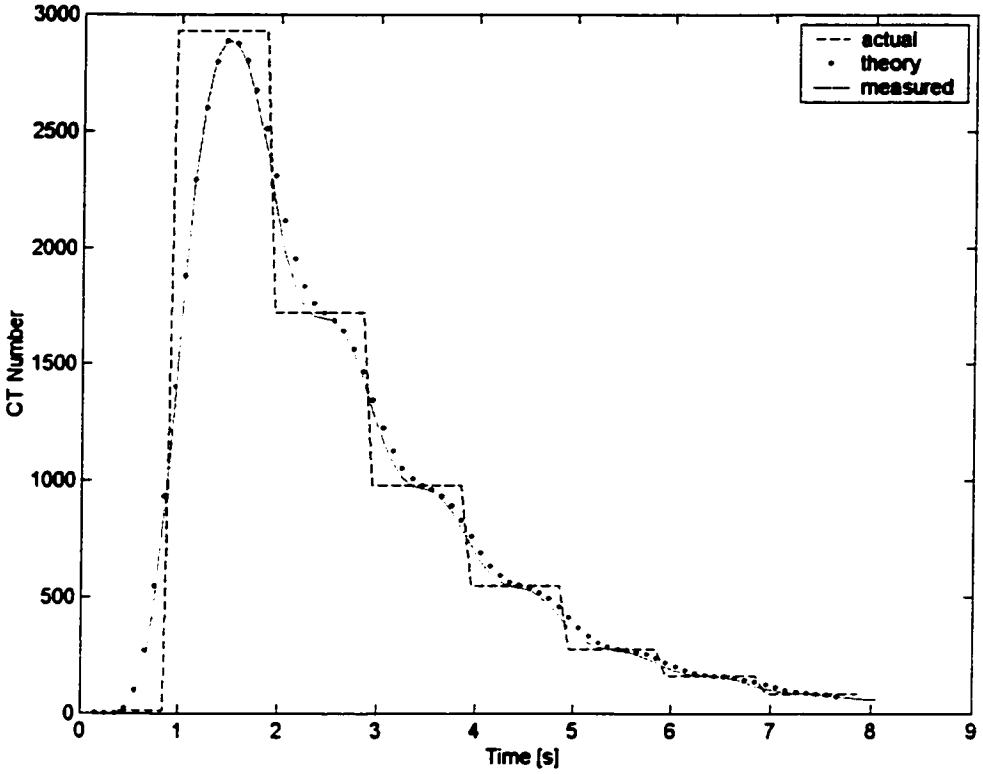

Figure 3-17: Actual, theoretical and measured *CT#* as a function of time when velocity is 4 cm/s.

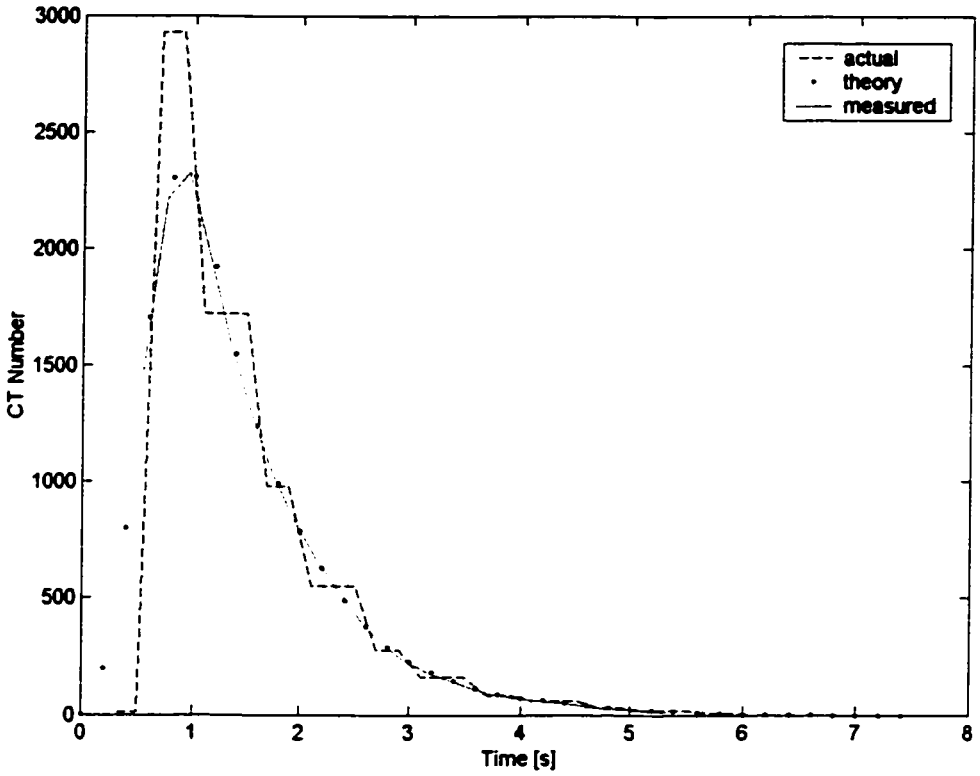

Figure 3-18: Actual, theoretical and measured *CT#* as a function of time when velocity is 8 cm/s.

For the 4 cm/s data, notice that the theoretical and measured *CT#*s are much smoother than the true curve. This is to be expected due to the averaging effects of the signal. Clearly, high-frequency components of the time-density curve become lost when going from the true to measured curves. This loss of high-frequency information is further illustrated for the 8 cm/s data on Figure 3-18. Note also that the absolute maximum of the measured or predicted *CT#*s does not reach the maximum of the true (axial) *CT#*s, again from the averaging effect. In particular, note the actual concentration is nearly 500 *CT#*s greater than the measured and predicted one.

The measured *CT#*s for the 4 cm/s experiment agrees very well with the theoretical results in all regions of density variation. The agreement in the 8 cm/s data is also very good with the exception of the initial large density variations. The agreement between the measured and predicted results seem to be slightly off during the largest changes in *CT#*. This difference is likely due to the data handling features of the reconstruction algorithm. In a separate study in this institute, this was indeed the case [Kay *et al.* 2002].

An important finding in this experiment is that the magnitude of the *CT#* for pulses that are faster than the duration of the image acquisition is less than that of the axial scan. Also, the true concentration in f-CT is modified primarily through a loss of high-frequency information. This loss in information is a function of the velocity of the sampled signal, details of the image acquisition, and the spatial and temporal sampling interval. The decrease in the magnitude of the *CT#* may well introduce a bias in parameter estimates extracted from time-density curves. In particular, parameter estimates which are deduced by examining rise-times and maximums of the CT-time curve may be suspect to errors.

3.4.4 Effects of time-dependent signals external to vessels

The motion of the vessel results in a degradation of image quality and variations in *CT#* peripheral to the vessel. Shown in Figure 3-19 is an example of these artifacts from the spiral image where the contrast changes from 150 to 75 mgI/ml. The image is displayed with window width setting of 1000 centered at 1000 (equivalent to water)

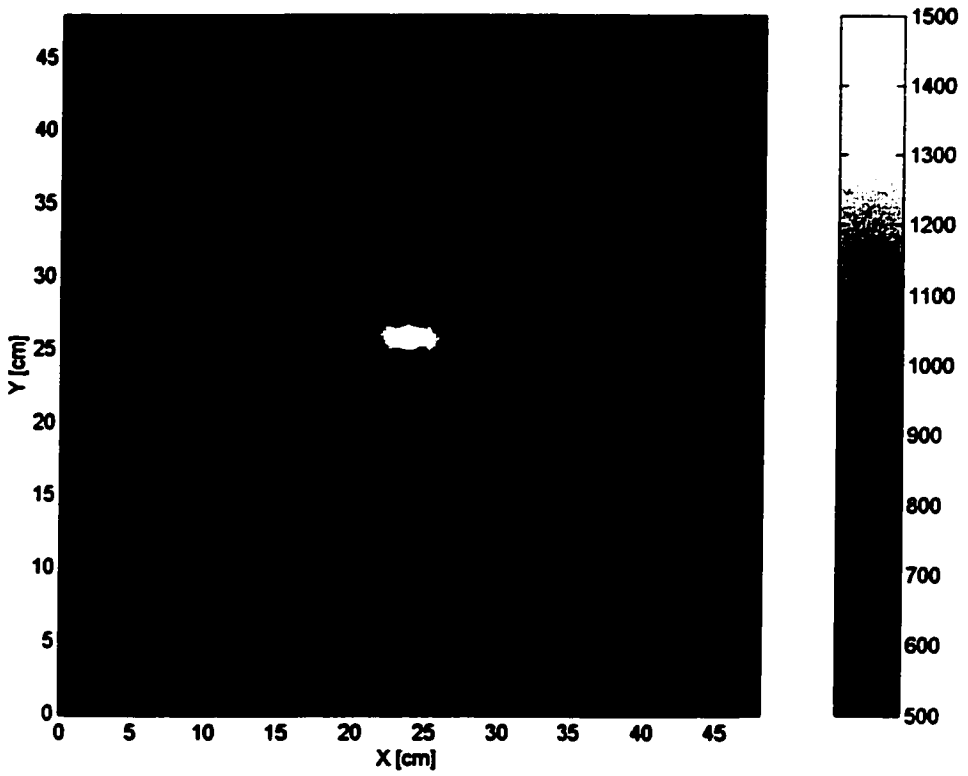

Figure 3-19: An example of CT image artifacts from the time-dependent signal. On the right is the window and leveling of the CT image.

The streaking artifacts result in both increases and decreases in *CT#* peripheral to the vessel. In contrast, only small variations in *CT#* are observed in the spiral image where the contrast changes from 0.300 mgI/ml to water (see Figure 3-20).

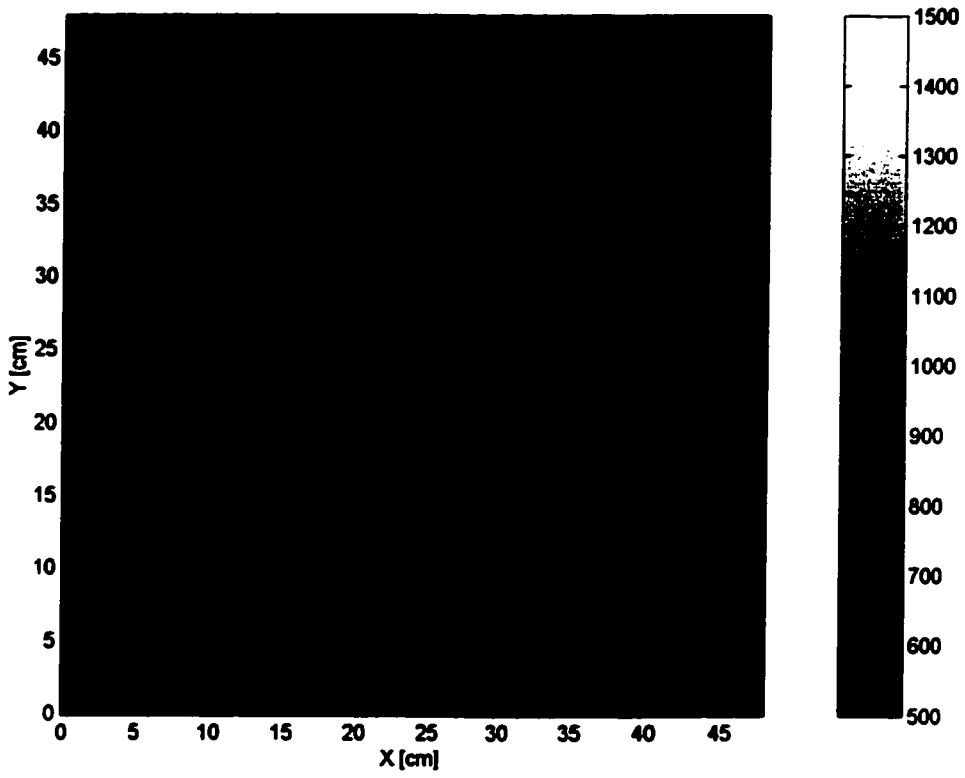

Figure 3-20: An example of CT image artifacts from the time-dependent signal with little density variation.

To examine these artifacts more closely, the *CT#* within small annuli (centered on the rod and equally spaced in annuli from the center outwards) were analyzed. The positions of the streaking artifacts are somewhat unpredictable and are not as important as the magnitudes of the *CT#* variations. Thus, the *CT#* within the annuli were converted into histograms. Here, the numbers of counts of an individual *CT#* (ranging from 0 to 4096) were counted within each annulus. Figure 3-21 displays a histogram of the *CT#* of the stationary (axial) and dynamic (spiral) experiment measured within an annulus bounded by circles with radii (R) of 20 (or 11 cm) from the center.

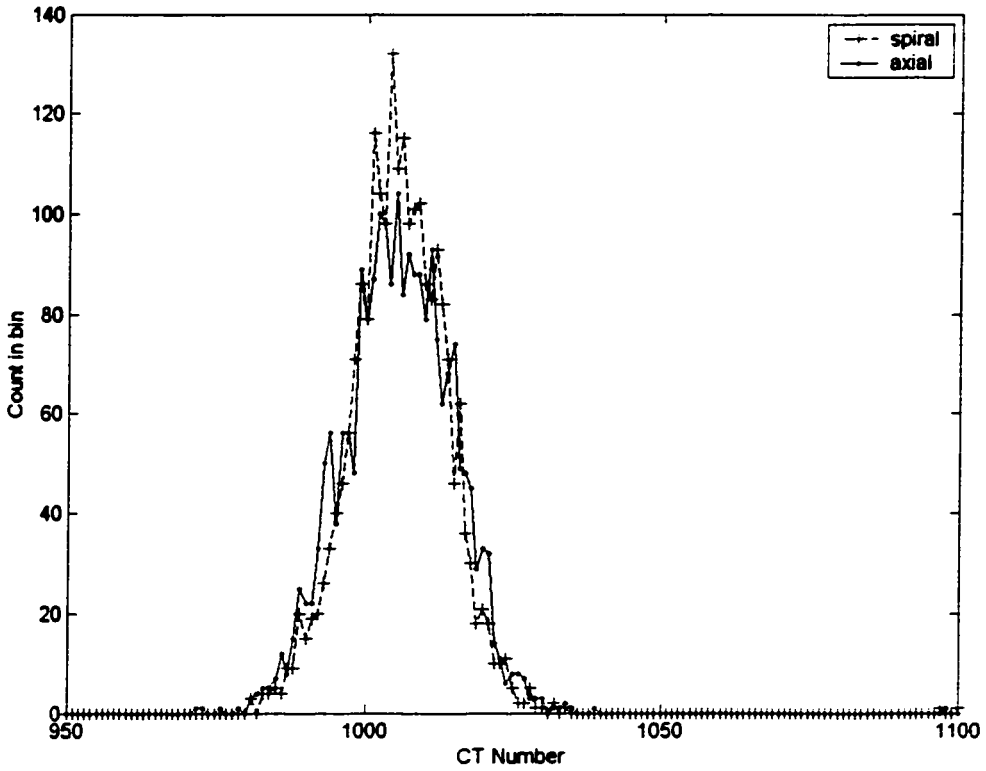

Figure 3-21: Histogram of *CT#* within an annulus far from the central.

As expected, the average *CT#s* within the annulus for both the stationary and dynamic experiments are very close to water (mean=1006 *CT#*) and has approximately a gaussian distribution (standard deviation=13 *CT#*).

In contrast, Figure 3-22 displays histograms of *CT#* when the central vessel changes from 150 to 75 mgI/ml. Instead of having a gaussian-like shape, the spiral histogram appears to have a bi-modal shape, where one curve appears to be centered about 989 *CT#* with a standard deviation of 10 *CT#*, and the second is more broad, centered about 1031 *CT#* with a standard deviation of 14 *CT#*. These results are

reflected in Figure 3-19 where there are bands of higher and lower streaks from the central vessel.

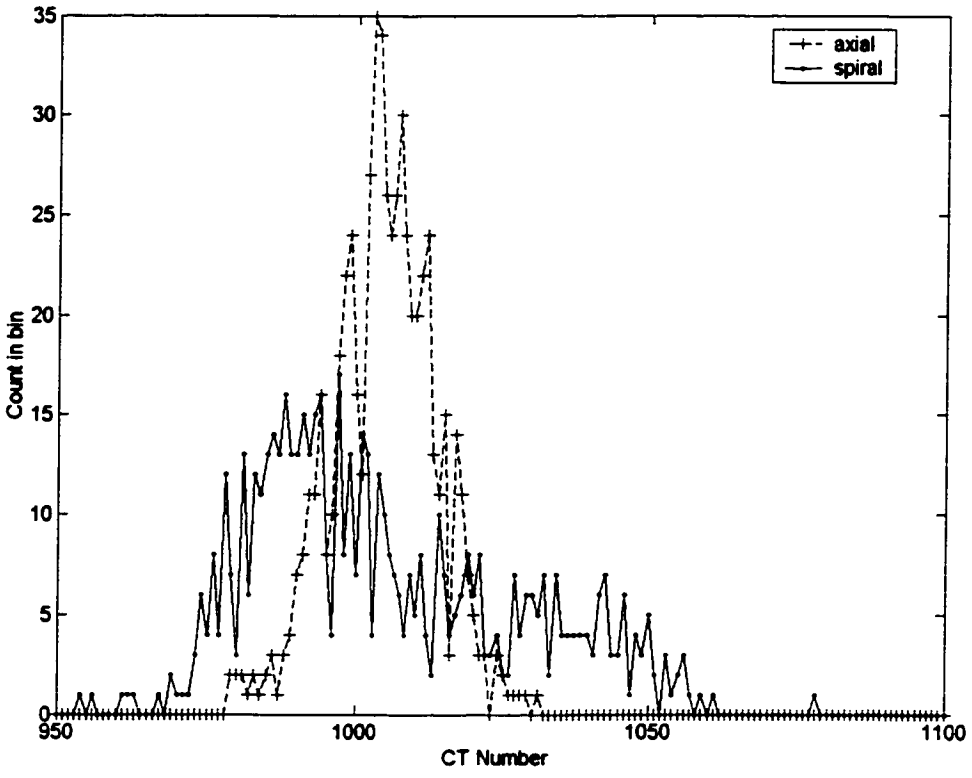

Figure 3-22: Histogram of *CT#s* within an annulus adjacent to the central rod.

Another interesting feature is the difference between the stationary (axial) and dynamic (spiral) images. Beam hardening does not explain the perturbation of the *CT#* since the distribution of the *CT#* in the axial image is very similar to that in Figure 3-21. Clearly, the artifacts present in the dynamic image are due to the reconstruction of the dynamic signal, not beam hardening.

The bimodal feature of the dynamic image data is less pronounced further from the center and when the change in central density are small. For example, Figure 3-23

displays the histograms for annuli of radii of 1 to 10 R when the central density changes from 150 to 75 mgI/ml. The count in the bins is represented as gray scales, as indicated on the colorbar right of the image. As the distance from the central radii increases, the density of the water within the annuli becomes closer to the *CT#* of water.

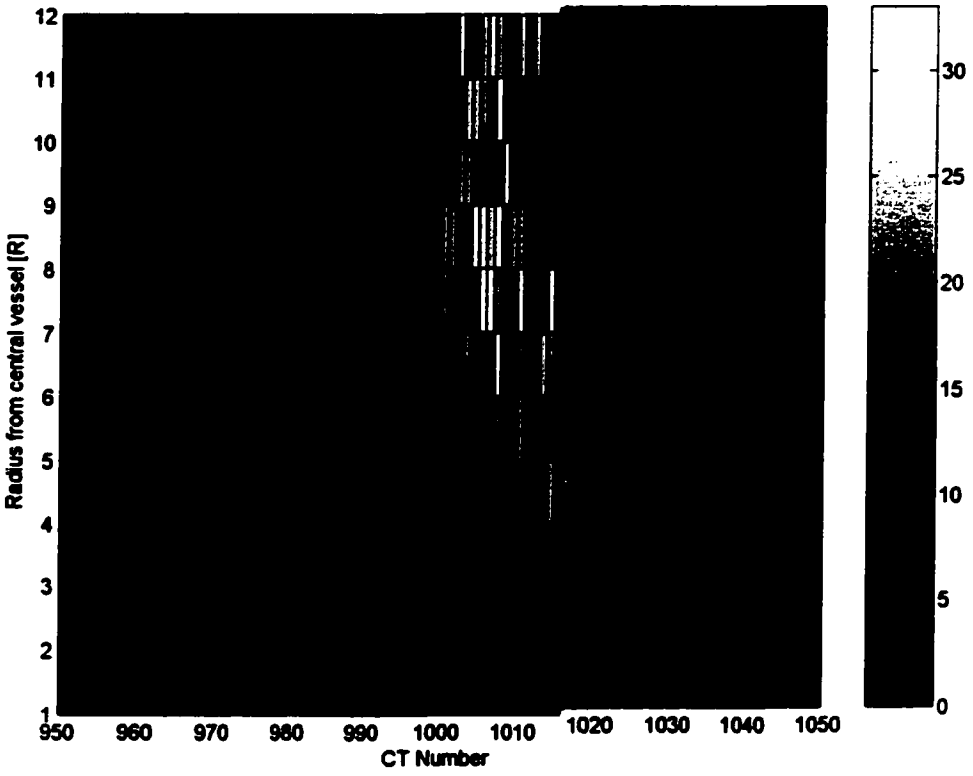

Figure 3-23: Image of 'histograms' for all radii of annuli when central concentration changes from 150 to 75 mgI/ml.

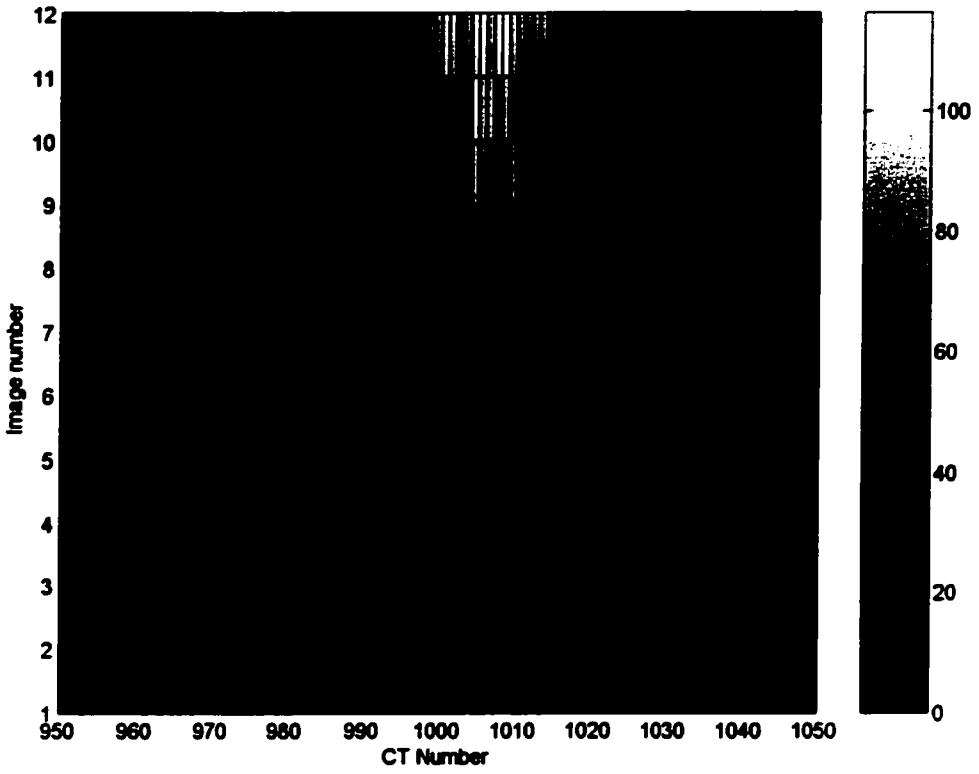

Figure 3-24: Image of 'histograms' for the closest central annulus when central concentration changes from 150 mgI/ml (image 1) to water (image 12).

Figure 3-24 displays the same image but with image number on the y-axis. The histograms in this image are displayed for the annulus closest to the central rod. As the difference in central density decreases, the *CT#* within the annulus approaches that of water. Note the different window and leveling of the image.

3.5 Discussion

Within the limits of most conventional CT scanners, the measured concentration curves do not appear to be very different from the true ones when the length of the input signal is greater than the pulse width multiplied by the velocity of the pulse within the scanning volume. Even when this is not the case, the errors introduced into parameter estimates extracted from the dynamic study appear to be small when the ratio of velocity to pulse variance (v/s) is small (~4 s^{-1}). However, special care must be taken in interpreting data when the concentration changes rapidly. This may be of concern in f-CT methods that rely on rise-times of concentration.

Generally, the concentration curve and *CT#* are related in a complicated way. In many of the simulations and measurements demonstrated here, concentration as a function of distance does not correlate with *CT#* as a function of time. Although this finding was first demonstrated by Cottrall and Lane *et al.* in the 1970s, their findings were not put in the context of typical f-CT study [Cottrall 1977, Lane *et al.* 1975]. Because of these discrepancies, special care should be taken in f-CT analysis of vessels with rapidly changing and/or high blood-flow velocities.

The effects of CT averaging due to finite sampling times and volumes may introduce bias in parameter estimates extracted from a f-CT study. This bias expresses itself primarily through the loss of high frequency components and reduced *CT#* in the actual concentration. One implication of these findings is that f-CT methods that rely on the time-to-maximum *CT#* will be in error. In the dynamic rod experiments, differences between the true and measured *CT#* were as great as 600 over a one second interval in

the 8 cm/s data. This concentration behavior is less likely with an antecubital administration of contrast and in vessels exhibiting lower blood-flow velocities; however, prior to a f-CT study, the magnitude of these velocities is often unclear.

Within the context of using f-CT to measure changes in regional lung perfusion from radiation therapy, special care should be taken in light of these findings. Because contrast administration is a passive process, changes in the velocity distribution within a voxel is not expected; however, it is possible for blood flow velocities to change after the onset of disease or therapy. If f-CT is used as a prognostic tool to assess the efficacy of a certain therapy, it is quite possible for the blood flow velocities to change after the course of treatment. A follow-up concentration curve may well have the appearance of a previous concentration curve but instead have quite a different velocity distribution. The subsequent parameter estimates yielded from these 'before and after' f-CT studies may therefore be erroneous. If the velocity in the voxel decreases, the ratio of *v/s* drops; therefore, the parameter estimate may be reliable. But this may not be true when the ratio of *v/s* increases. To eliminate any potential sources of error, the same f-CT protocol (amount and duration of contrast, injection velocity, scanning parameters, etc.) should be used before and after the therapy.

The CT number in surrounding voxels can be perturbed from their true values when adjacent voxels are experiencing significant changes in density. In the experimental work here, the perturbations are primarily due to the reconstruction and not beam hardening. Beam hardening affects only the *CT#* in those voxels undergoing changes in density, not the external voxels. As a crude estimate, the *CT#* in water may

be perturbed by as much as 40 *CT#*, which approximately 4 % of the *CT#* in water, but may be much greater in lower density tissues such as lung. Assuming the magnitude of these errors also exist in lung tissue, then these errors may be significant. The *CT#* in lung may vary from 0 to 1000, producing a wide range of potential errors. Typically, lung *CT#* are approximately 300, which imply a maximum error in the *CT#* of approximately 40/300 = 13% simply due to these time-dependent artifacts. This error is quite large and may be a significant source of error affecting the calculation of parameter estimates yielded from a f-CT study. These errors become significantly reduced with smaller changes in *CT#* and increased distances from the changing vessel. Therefore, perfusion estimates peripheral to vessels which change dramatically are not expected to be reliable.

4. Parameter estimation with functional CT data

In estimating perfusion from a f-CT study, the CT data must be analyzed and collapsed into a representative perfusion parameter estimate. The purpose of this chapter is provide a review of numerical techniques often employed in f-CT and also to describe a new method of analyzing tomographic images. In the first section of this chapter, a review of common numerical techniques used to generate various perfusion estimates is provided. Because the data-reduction is often unstable, special care must be taken during the numerical analysis. In the second section, a new method of analyzing tomographic images through the use of multiple deconvolutions is described and this method is compared with existing ones.

4.1 Review of numerical techniques in functional CT analysis

4.1.1 Compartmental Analysis

The basic idea behind this approach is to model the system as a set of compartments, to generate a conservation of mass equation for the contrast within these compartments, and to measure the corresponding signals within a single or multiple compartment(s). Compartmental analysis is typically easier to perform than more complex approaches, such as linear systems modeling, and also requires fewer assumptions to be made regarding the response of the system. Typically, an input or output vessel is required in the model.

Vascular flow per tissue volume may be computed with:

$$F\,c(t) = V\,[\int a(t)\,dt - \int v(t)\,dt\,], \qquad \textbf{Equation 4-1}$$

where $c(t)$, $a(t)$, and $v(t)$ are the tissue, arterial and venous concentrations, respectively [Miles *et al.* 1997]. Here, both the arterial and venous time-density curves are required for the analysis. However, if a sharp bolus administration is delivered whose pulse duration is less than the time for the contrast to pass from the tissue to the venous compartment, one can remove the integral in $v(t)$ from Equation 4-1 This may be done by simply limiting the range of integration to some maximum value that is less than the time when the contrast begins to contribute to the venous compartment. Such studies require the rapid acquisition of images within the first few seconds of the bolus administration.

Re-circulation of the blood may take place as early as 20 s from the injection into the system. The result of this re-circulation is a superposition of another time-density curve with the existing curve. Often, these re-circulation artifacts can be removed in the analysis by limiting the time series to regions less than the onset of the re-circulation, or fitting the function to a gamma-variate function [Thompson *et al.* 1964].

Diffusion-type approaches involve the measurement of the contrast agent as it diffuses through the extravascular space. First suggested by Patlak, in Positron Emission Tomography studies, the equation:

$$\frac{c(t)}{b(t)} = \phi_b + (\alpha/V)\frac{\int_0^t b(\tau)d\tau}{b(t)}, \qquad \textbf{Equation 4-2}$$

is used, where $c(t)$, and $b(t)$ is the tissue and blood concentration, ϕ_b is the fractional vascular volume of the tissue, and α is the blood clearance [Patlak *et al.* 1983]. By

measuring a vein or artery, $b(t)$, and the tissue concentration c(t), it is simple to plot the above function with $c(t)/b(t)$ on the Y-axis, and $\left[\int_0^t b(\tau)d\tau\right]/b(t)$ on the x-axis, yielding the fractional vascular volume for the y-intercept and slope equal to clearance over volume, V. Such studies require the contrast to migrate through the extravascular space, and thus the data acquisition typically require several minutes.

Apart from restrictions in the duration of the scan, there are other problems associated with compartmental approaches. Often, a conservation law, such as the total mass of contrast, is required. Since f-CT with conventional scanners do not allow for simultaneous imaging of the ROI over a large volume, a direct measurement of the total contrast is not often possible. This may be possible in some angiography techniques or multi-slice CT imaging, but is much more difficult in conventional CT. Thus, assumptions on the total distribution of mass within the ROI are required, which for the most part, are not unreasonable [Miles *et al.* 1997].

4.1.2 Inverse methods

Inverse theory formalizes the method of reducing data to model parameters based on a series of observations. The "Inverse" problem is the process of estimating, or learning as much as possible, about the model parameters using the initial data. The "Forward" problem is the process of estimating the data based on the model and model parameters. In the f-CT image, one usually obtains measurements of a response based on some measurement, thus making our problem an inverse one.

Let **o** be the data vector, of length N, which in this case represents a time-series measurement of *CT#*. In the mathematical formulation of the problem, a solution based on some existing data and possibly some model parameters is sought. If **o** is the output function, **H** is the operator on the input function that maps the input, **j**, to the output, the generalized integral equation may be represented as:

$$\mathbf{o}(x,y,z,t)=\int \mathbf{H}(x,x',y,y',z,z',t,\tau)\,\mathbf{j}(x',y',z',\tau)\,dx'\,dy'\,dz'\,d\tau \qquad \textbf{Equation 4-3}$$

or using a matrix notation,

$$\mathbf{o} = \mathbf{H}\,\mathbf{j}\,, \qquad \textbf{Equation 4-4}$$

where the dependence of position is noted as a function of anatomic position *x*, *y*, and *z*. By dropping the positional dependencies for simplicity, one can assume that neither the input, output, nor impulse response depends on the position. However, in the case of the lung, various effects, such as gravity and posture, alveolar density, and disease seriously affect diffusion and perfusion, and as such, often provide the rationale for the measurement.

The function **H** may consist of a number of independent model parameters, **m**, which defines a vector.

$$\mathbf{H}=\mathbf{H}(\mathbf{m})\,, \qquad \textbf{Equation 4-5}$$

or assuming linearity,

$$\mathbf{H}=\underline{\mathbf{h}}\,\mathbf{m}\,, \qquad \textbf{Equation 4-6}$$

where $\underline{\mathbf{h}}$ is a I by J matrix and **m** is the model parameter vector, whose rank is equal to the size of the model parameters. When the kernel **H** is simply a function of the difference $(t-\tau)$, the integral becomes a convolution. In this case, the entries of the matrix

H depend only on the i-jth indices, making the matrix **H** a circulant Toeplitz matrix. Toeplitz matrices have constants along all diagonals. Generally, the matrix **H** is ill-conditioned.

When a model-based system is used, the matrix **H** becomes a function of model parameters, called **m**. The model parameters may be of any length; however, for the purposes of simplicity, the length of **m** should be small. Noise may be explicitly entered into this formulation by simply adding an additional vector **n**, of length N, to Equation 4-4:

$$\mathbf{o} = \mathbf{H}\,\mathbf{j} + \mathbf{n}\,. \qquad \textbf{Equation 4-7}$$

4.1.3 Linear Systems Analysis

In the linear systems approach, one assumes the system measured is linear, time-invariant, and homogeneous. Using signal-processing techniques, estimates of parameters such as transit time of the contrast, can be extracted from the measured signals. These techniques often provide more insight into the transit times of the contrast, but requires more data handling, analysis, and sometimes assumptions about the system.

In a linear systems approach, one has:

$$\mathbf{O}(t) = \int \mathbf{H}(t-\tau)\,\mathbf{J}(\tau)\,d\tau\,, \qquad \textbf{Equation 4-8}$$

where $\mathbf{O}(t)$ and $\mathbf{J}(t)$ are the output and input time series, and $\mathbf{H}(t)$ is the impulse response of the VOI. The impulse response, $\mathbf{H}(t)$, fully characterizes the blood flow in the sampling region. It describes the time-density distribution of the system subject to a delta-function input. The shape and form of the impulse response can provide some

information about the physiology of the system measured. The first moment with respect to time, is an estimate of the mean tissue transit time:

$$MTT_h = \int t\, \mathbf{H}(t)\, dt \,/\, \int \mathbf{H}(t)\, dt \ . \qquad \textbf{Equation 4-9}$$

Alternatively, if an arterial and venous supply to a system, s, can be measured, one can calculate:

$$MTT_s = \int t\, \mathbf{O}(t)\, dt \,/\, \int \mathbf{O}(t)\, dt \ - \ \int t\, \mathbf{J}(t)\, dt \,/\, \int \mathbf{J}(t)\, dt. \qquad \textbf{Equation 4-10}$$

The above formulations for the MTT have come under some criticism, based on the arguments that velocity of blood flow and exchange of particles between volumes of interest (VOIs) are not specifically addressed [Doriot *et al.* 1997].

The process of evaluating the response function in f-CT images has been labeled as deconvolution. In a more general mathematical sense however, the problem of extracting H(t) is an inverse problem. In an inverse problem, a suitable form of a kernel function that describes the observations is sought. With the assumption of time invariance, the problem simplifies to a convolution.

There are two approaches used to examine and extract the impulse response. With the first approach, no assumptions about the shape of the impulse response can be made and one can apply some mathematics with the input and output functions to estimate the impulse response. These methods are defined as 'non-model' based techniques. Non-model based techniques include least squares inversion, numerical deconvolution, and transform (such as Fourier, Laplace and wavelet) techniques where little *a priori* information on the shape of the impulse response function is assumed. The second approach is to model the impulse response function in some manner and perform

a numerical fitting of the model function with the observed data. These are defined as 'model' based techniques.

As an aside, of recent interest in the literature are attempts at blind deconvolution, where nothing is known about the input, nor the impulse response [Mignotte *et al.* 2000, Bertero *et al.* 1998]. With some assumptions about the system, it is possible to extract both the impulse and input function through mathematical techniques. This problem occurs extensively within the signal processing venues of the literature [Harikumar *et al.* 1998].

4.1.4 Existence and Uniqueness of a Solution

Before a discussion of the various analysis techniques is given, it is useful to point out some mathematical peculiarities in our inverse problem. In particular, a brief discussion on the existence and uniqueness of a solution is given. For the purposes of our examples and future discussion, the problems to be solved are assumed to be linear.

Mathematically, a solution based on some existing data and possibly some model parameters is sought. As noted above, the impulse response function **H** may consist of a number of independent model parameters, **m**:

$$\mathbf{H}=\underline{\mathbf{h}}\mathbf{m}\,. \qquad \textbf{Equation 4-6}$$

By existence, neither the matrix $\underline{\mathbf{h}}$ nor the vector **m** is null. This is of great importance when estimating parameters within a model-based technique. If $\underline{\mathbf{h}}$ or **m** is null, it would indicate the "incompatibility" of the experimental results: something is amiss in the model. One must ask if there are any necessary or sufficient conditions to ensure a

solution to the problem. Both are based on physical measurements or *a priori* information about the system.

Another important mathematical issue is the question of uniqueness. That is, given our data, is there only one solution? The answer to this question is of paramount importance if the shape of the solution is to be further analyzed. Unfortunately, uniqueness is often very difficult to prove. In the context of f-CT images, this is equally important (and is discussed later). If a parameter is estimated from the curve (ex: MTT from the impulse function) the non-uniqueness of the curve may result in erroneous parameter estimations.

4.1.5 Ill-condition and Uniqueness of the Impulse Response Function

4.1.5.1 Uniqueness of a solution

Generally in f-CT studies, the calculation of the impulse response is an ill-conditioned problem. To better understand this, let the problem be estimating the matrix **H** in the equation:

$$\mathbf{o} = \mathbf{H}\,\mathbf{j}\,. \qquad \textbf{Equation 4-4}$$

We are usually free to choose the dimension of the vector **j** (or **o** depending on the measurement technique), either by interpolation, truncating the data set, or changing the sample rate, but one generally does not choose a different degree of freedom in **o**. The matrix **H** is a circulant Toeplitz matrix which are non-singular, and thus has a unique (non-degenerate) form. Mathematically then, it is possible to extract the exact impulse response of a system given the vectors **o** and **j**.

However, a non-singular matrix can have degenerate solutions if the equations are close to being linearly independent. Furthermore, computer round-off errors in the attempts of finding the solution can undermine our attempts to arrive at the solution. Both sources of error can be easily determined by checking $\mathbf{o}$ against the calculation of the estimate, $\underline{\mathbf{H}}$, operating on the measured input $\underline{\mathbf{H}}\ \mathbf{j}$. But this checking does not guarantee uniqueness. Thus, there may be a unique solution mathematically; however, the correct solution may not be attainable due to computer round-off errors.

4.1.6 Non-Model Based Techniques

An advantage of non-model based techniques is that no assumptions about the nature of the response are made. Non-model based techniques are the method of choice in well-conditioned problems. However, non-model based techniques, such as least squares deconvolution, and transform methods are often plagued with numerical problems such as noise contamination and singularities. Several investigators have addressed these issues by curve fitting, digital filtering, and other signal processing techniques. These techniques are useful and can be based on constraints and limitations of the system analyzed. For instance, one may suppress the unphysical frequency components or remove negative components of the contrast signal by smoothing or filtering, based on physically sound assumptions of the system.

4.1.6.1 Moment Analysis

Bronikowski *et al.* (1983) proposed a method for describing arterial response in lung tissue by 'moment' analysis. There are two fundamental assumptions in the approach:

$$t_o = t_i + t_h \,, \qquad \textbf{Equation 4-11}$$

$$\sigma_o^2 = \sigma_i^2 + \sigma_h^2 \,, \qquad \textbf{Equation 4-12}$$

where, $t_{o,i,h}$ are the mean time of the output, input, and impulse response functions, and $\sigma_{o,i,h}$ are their respective errors. The authors show that by using the above conditions and time-shifting the output function, it is possible to estimate a stable impulse response.

4.1.6.2 Least Squares Deconvolution

A least squares deconvolution is a simple, non-model based, method for extracting a filter, **H**, that can produce the output in a least-squares sense. The theory of least squares deconvolution is generated from constructing the normal equations. The procedure is as follows. First, the auto-correlation of **J** is calculated and transformed into a Toeplitz matrix. The inverse of the Toeplitz matrix is then multiplied with the cross-correlation of **O** with **J**. The result is an estimate of **H**. The method is very simple and easy to implement; however, it is prone to singularities during the inversion of the Toeplitz matrix.

Li and Cutler explored the conditions under which this approach, also called finite-difference method or point-area deconvolution, are stable in pharmacokinetic problems for drug administration [Li *et al.* 1998a, Li *et al.* 1998b]. They suggest that

instead of using the input vector **J**, one can equally use a cumulative input vector, **JC**. This transforms the impulse response matrix into a similar but less ill-conditioned form. They argue that for intra-venous (IV) administration, this approach is stable. They also argue that errors in obtaining the solution are more likely due to sampling errors than to numerical deconvolution.

Regularization methods have also been proposed with success, to provide constraints to the solution. The basic idea is to fit the data with a function such as:

$$\mathbf{E} = \mathbf{A} + \alpha \mathbf{B}, \qquad \textbf{Equation 4-13}$$

where **A** is the reduced Chi-squared statistic based on a trial input function, **B** is some quadratic form and α is a regularization parameter. The matrix **B** may take on several forms, such as first, second, or third order difference matrix; however, the regularization parameter must be selected prior to application. More will be discussed on the selection of a regularization parameter in this chapter. Bronikowski *et al.* (1983) applied such an approach with success in pulmonary physiology studies. Hovorka *et al.* (1998) found that the optimal selection of the matrix **B** depends on the nature of the impulse response: third order difference matrices seem to match highly curved impulse response, where first order difference matrices seem to match monotonically decreasing impulse responses. Verotta (1993) used first order difference matrices with success in pharmaceutical applications. Huesman and Mazoyer (1987) proposed a similar model in analyzing PET images where noise was incorporated in the regularization. Szabo *et al.* (1987) used a similar approach in nuclear medicine studies. They argue that neither a good reconvolution fit, nor a minimal deviation from an 'ideal' impulse response should

be a decisive criterion since model parameters extracted from these curves are usually more important than the shape of the curve.

4.1.6.3 Transform Methods

Equation 4-4 may be easier to solve in another space by applying some transform, solving for **H**, and applying an inverse transform. In particular, let T be such a linear transform. Then assuming existence in **o**, **H** and **j**, through some simple algebra:

$$T\{\mathbf{o}\} = T\{\mathbf{H}\,\mathbf{j}\} = T\{\mathbf{H}\}\,T\{\mathbf{j}\} \qquad \textbf{Equation 4-14}$$

$$T\{\mathbf{o}\} / T\{\mathbf{j}\} = T\{\mathbf{H}\}$$

$$T^{-1}\left[T\{\mathbf{o}\} / T\{\mathbf{j}\}\right] = \mathbf{H}\,.$$

Wirestam *et al.* (2000) used low pass filters with their data to examine cerebral blood-flow with MRI; however, they argue that the use of such filters may affect parameter estimation. Flemming and Kemp (1999) solve this problem in Laplace space to improve image quality of SPECT images by deconvolving the raw data with estimated blurring functions.

Of particular relevance to this thesis is the work of Tajik *et al.* (1998), who performed f-CT analysis with an ultrafast CT scanner in evaluating pulmonary function in dog lungs. They used a Fourier transform technique after fitting the input and output data with finely sampled gamma-variate functions. They found that using an inverted Hanning window, often used in SPECT analysis, enhanced the quality of the measured impulse response functions, resulting in a bi-modal response function: one consisting of faster micro-vascular transport, the other consisting of a slower capillary/alveolar transport. The bi-modal nature is due to the partial volume averaging of the voxels that

have dimensions much larger than the capillary/alveolar regions. More will be said on this in following chapters.

Either Fourier or Laplace transforms can be applied in this non-model based approach. More exotic transforms, including wavelets, may also be used, but their benefit has yet to be found and still remains an interesting venue of research [Xie *et al.* 1995]. Similar issues with singularities arise when using transform approaches. Padding the data with additional zeros, or other signal processing tricks may be used to resolve some of these artifacts [Press *et al.* 1992]. Positivity constraints and filtering may also be applied to ensure the properties of the impulse response are physically meaningful.

4.1.6.4 Optimal Filtering

If an estimate of the noise is possible during the measurement, it is possible to remove the noise component in the signal and use transform methods. The method is discussed elsewhere, and is briefly mentioned here [Press *et al.* 1992]. The process is identical to the transform method discussed earlier; however, filter, Φ, which effectively "undoes" the effects of noise in the original signal is required:

$$T^{-1}[\Phi\ T\{o\}/T\{j\}]=H. \qquad \textbf{Equation 4-15}$$

This is defined as a filter, in a least-squares sense:

$$\Phi_{\cdot}=|T\{o\}|^2/\ [\,|T\{o\}|^2+|T\{n\}|^2\,]. \qquad \textbf{Equation 4-16}$$

Sutton and Kemp applied this approach, in addition to a positivity constraint, in renographic analysis of kidney function [Sutton *et al.* 1992].

4.1.6.5 Recursive Filters

There are many recursive filter-type approaches to the deconvolution problem. Although the reasons for not attempting such an approach in f-CT images are unclear, no such attempts have been recorded in the literature. There have been attempts at such approaches for other medical applications. For instance, Vadja *et al.* employ an ARMA filter approach in estimating the impulse response in pharmacokinetic modeling [Vadja *et al.* 1998].

A primary requirement in estimating the impulse response is that it be causal. This can be done through a combination of zeros and poles in the filter design itself. A second requirement is that the filter be stable; that is, after the last inputs, the output eventually goes to zero or a constant. It can be shown that the transform and filtering techniques discussed earlier are stable filters; but recursive filters may or may not be stable [Hamming 1987]. Lastly, a positivity constraint ensures a physically meaningful solution.

The basic idea behind the recursive filter approach is to calculate a filter that converts the measured input to the measured output. Once the filter is designed, one can apply a delta function to the filter to estimate the impulse response function. Briefly mentioned here are three types of recursive filter approaches. By no means is this a comprehensive list of methods for such approaches. Other comprehensive books on the subject are available [Press *et al.* 1992, Hamming 1987].

An exact inverse transform can be obtained by using a simple recursion relation for:

$$y_k = \frac{1}{b_o}\left[\sum_j a_j x_{k-j} - \sum_j b_j y_{k-j}\right], \qquad \textbf{Equation 4-17}$$

where x_i is the input function, a_i is the output function, b are the coefficients of the filter. This simple formulation is highly sensitive to the initial values of the input function parameters and noise and can often result in negative values in the impulse response.

A special case of recursive filters is where the output depends on only the last input. More precisely, the sequence of possibly dependent random variables x_1, x_2, x_3, ... x_n has the property that the prediction of the value of x_1, x_2, ... x_{n-1} is based on the value of x_{n-1} alone. Filters of this sort are described as Markov Chains, which stem from probability theory. Several authors have found utility in this technique in describing some physiological parameters, but its application has been mostly limited to information theory in blind deconvolution. There is no published work on this approach in analyzing tomographic images.

Maximum entropy methods (MEM) rely on the premise that the process under investigation is an "all poles" process plus a white noise excitation series. This technique is more commonly used in fields such as geophysics and image deblurring, where the impulse response exhibits some type of auto-regressive behavior. Charter and Gull (1987) give a treatise on MEM approaches employing positivity constraints. There are no published reports on MEM approaches in f-CT image analysis.

4.1.6.6 Stochastic approaches

One way to compute the response function is by simply guessing the impulse response function. Monte Carlo techniques perform an exhaustive search of all the

possible types of impulse response functions in the convolution. The approach is a "strong-armed" approach and typically requires massive amounts of computer time and energy. However, it is much more exhaustive and comprehensive than other approaches and does not require the problem to be linear. There are several methods of implementation of such an approach, such as using simulated annealing, genetic algorithms or other approaches [Press *et al.* 1992]. Madden *et al.* (1996) employed a genetic algorithm in deconvolution problems in pharmaceutical applications. There are no reports in the literature on the use of such techniques to analyze f-CT images.

4.1.7 Model Based Techniques

Model based techniques require some underlying assumptions on the shape of the impulse response function. Axel's work in functional CT is an example of this technique [Axel 1980]. A model impulse response is given whose nature and shape is defined through a single parameter or set of parameters. This approach simply convolves the input function with the test impulse response, compares the result with the output, and changes the parameters of the impulse response until the output matches that of the re-convolved test function and input function. One can phrase this as an optimization problem of finding the model parameter(s) that minimizes the variable χ^2:

$$\text{Min}(\chi^2) = \min\left(\left| o(t) - \int H(t-\tau)\, j(\tau)\, d\tau \right|^2 / \sigma(t)^2 \right), \qquad \textbf{Equation 4-18}$$

where $\sigma(t)$ is an optional scaling parameter. The technique is very simple to implement and has thus been heavily employed.

Bassingthwaite *et al.* (1966) first suggested that curve-fitting of the input and output functions result in the most stable calculation of the impulse response. However, limiting the input and output functions to a particular form does constrain the possible range of solutions, thereby reducing the space of possible solutions of the impulse response function.

4.1.7.1 Damped Exponentials Basis functions

Of particular interest in medicine are uses of exponentials to describe physiological behavior. Exponential behavior is commonly observed in pharmacokinetics and other chemical interactions within the body. Veng-Pederson (1980) fitted a sum of exponentials to drug absorption data and developed a general solution to the deconvolution problem. He argues that it is not necessary, and perhaps distracting, to associate clinical significance to these parameters, since the system is often non-linear in such a way that the parameters are non-unique.

4.1.7.2 Basis function projection

Clough *et al.* (1993) used a discrete polynomial method, where polynomial basis functions are used to model the data. Here, orthonormal coefficients are projected through discrete integration with any set of basis functions. Clough *et al.* used Chebyshev polynomials.

4.1.7.3 Curve-fitting

Nakai (1981) used a piecewise curve-fitting approach of the impulse response based on minimizing a reduced chi-squared statistic. The method forces various regions

of the impulse response function to have quadratic forms which initially force the curve through the origin for *t* at zero, (assuming an impulse response which begins with zero), and tapers to zero for *t* at infinity. Although there is no assumption on the shape of the impulse response, there are assumptions about the relative shape of the function over different time intervals.

Verotta (1993) used a curve-fitting approach based on b-spline basis functions and uses information theory to determine the minimum number of parameters (i.e., the number of basis b-splines).

4.2 Use of arterial, tissue and output curves in deconvolution analysis of tomographic imaging studies

4.2.1 Introduction

A common approach in f-CT is to treat the signals as a series of independent causal-linear systems:

$$G(t) = F\int_0^{\infty} H(\tau - t)I(\tau)d\tau \qquad \textbf{Equation 4-19}$$

where $G(t)$ and $I(t)$ are the tissue and input functions, $H(t)$ is a normalized impulse response function where the maximum value is set to one, and F is a constant [Zierler 1965]. With $G(t)$ and $I(t)$ being the observed signals, the objective becomes the non-trivial task of estimating the impulse response function. The input and tissue functions are normally obtained by sampling the density of an artery and tissue on the set of CT images collected during the dynamic study. Each point in an image represents a measure of the density at some time, t, and the time-density curve is generated by repeated sampling of the density from the time-order CT data set.

In tomographic image studies, an arterial and tissue signal is monitored and the deconvolution is performed. However additional information, such as the signals from draining vessels, such as the aorta or vein, are often ignored (see Figure 4-1). For example, when studying perfusion in the brain with f-CT, the coronary artery and brain tissue is deconvolved. But often, the draining coronary vein is also often visible in the CT image.

Results of a deconvolution method that exploits the use of output signals when available in tomographic images are presented in this section. The concept is simple: solve impulse response functions for the input-tissue, while also solving the tissue-output system and enforcing linearity conditions between the two systems to constrain the space of feasible impulse response functions. Although the technique requires two deconvolutions as opposed to one, fewer – if any – restrictions are necessary on the impulse response functions.

This section is organized as follows: First, a description of the deconvolution method is given. Second, a series of numerical simulations of this deconvolution method are performed and compared against more conventional deconvolution methods. Last, this method is applied in an experimental setting.

4.2.2 Theory

This method relies on the principle that in addition to the input and tissue signals in the tomographic image, there also exists an output function, $J(t)$, defined through some impulse response function $H_2(t)$ through system 2 (see Figure 4-1). For clarity, let us pose the deconvolution problem in the framework of a linear inverse problem where I, G, and J are (1 x n) vectors, with noise δI, δG, and δJ, mapped by the Toeplitz matrices H_1 and H_2 (n x n) in series:

$$G + \delta G = H_1(I + \delta I) \qquad \textbf{Equation 4-20}$$

$$J + \delta J = H_2(G + \delta G) \qquad \textbf{Equation 4-21}$$

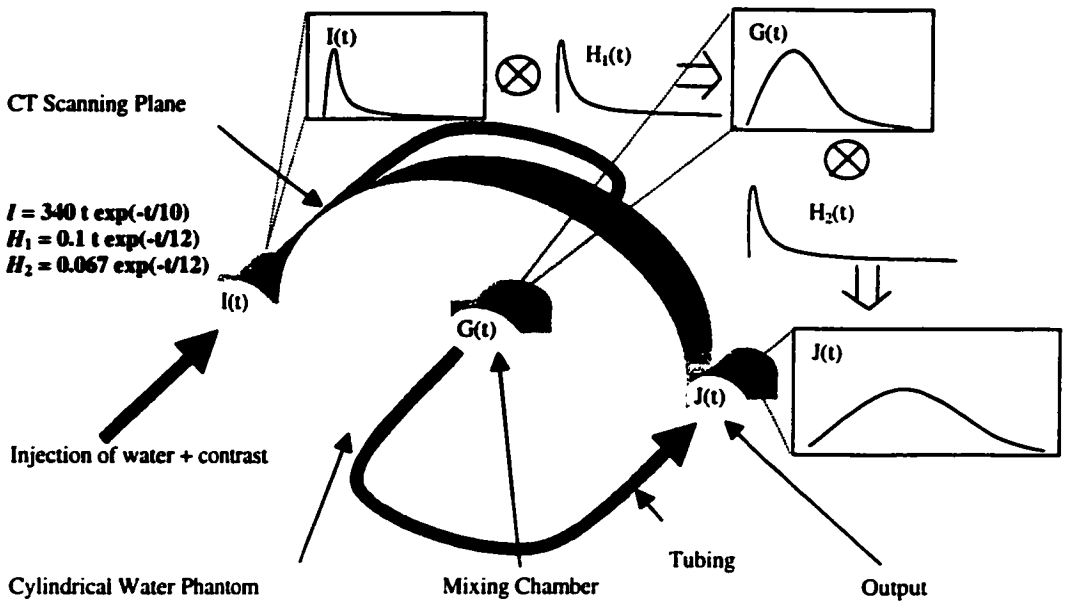

Figure 4-1: Phantom experiment of input, vessel, and output signals.

Our primary goal is to estimate H_1, but with the additional information in J, it would appear that there are two independent systems of equations to solve rather than one.

However, because the system is linear:

$$J + \delta J = H_{21}(I + \delta I), \qquad \textbf{Equation 4-22}$$

where:

$$H_{21} = H_2 H_1 \qquad \textbf{Equation 4-23}$$

The last relationship limits the solution space of both H_1 and H_2 and can therefore be used as a constraint in our attempts to find H_1. Therefore, if an inversion process which uses the relationship in Equation 4-23 is used, it may be possible to obtain

a solution to 1 and 2 which are more robust than the solutions to 1 and 2 arrived at independently. It can be shown that a more stable solution for both H_1 and H_2 can be obtained by solving for the H_{21} system and then decomposing H_{21} for H_1 and H_2, rather than for solving for H_1 and H_2 independently.

To demonstrate this, consider the inverse problem of finding the matrices H_1 and H_2. The stability of any inversion is governed by the degree of ill-conditioning of the matrix to be inverted, whereas the accuracy of the inversion is governed by the degree of the ill-posedness of the matrix to be inverted [Ueberhuber 1997a, Ueberhuber 1997b]. Let us explore here the ill-conditioning, or more precisely, the condition numbers of H_1, H_2, and H_{21} impulse response matrices. Practically, the condition numbers for $H_{(1 \text{ or } 2)}$ can be estimated through the following relationships:

$$\frac{\left|\frac{\delta I}{I}\right|}{\left|\frac{\delta G}{G}\right|} \leq \left|H_1\right|\left|H_1^{-1}\right| = cond(H_1), \qquad \textbf{Equation 4-24}$$

$$\frac{\left|\frac{\delta G}{G}\right|}{\left|\frac{\delta J}{J}\right|} \leq \left|H_2\right|\left|H_2^{-1}\right| = cond(H_2), \qquad \textbf{Equation 4-25}$$

or, conversely, through a calculation of some matrical norm if H is known. In the joint system, the condition number is:

$$\frac{\left|\frac{\delta I}{I}\right|}{\left|\frac{\delta J}{J}\right|} \leq \left|H_{21}\right|\left|H_{21}^{-1}\right| = cond(H_{21}). \qquad \textbf{Equation 4-26}$$

Because the system is linear:

$$H_{21} = H_2 H_1 \qquad \textbf{Equation 4-23}$$

From this equation and by use of the triangle inequality, one must have:

$$\text{cond}(H_{21}) \leq \text{cond}(H_2)\ \text{cond}(H_1), \qquad \textbf{Equation 4-27}$$

In other words, the condition number of the joint system is equal to, or less than, the condition number of the independent systems. Therefore, if one attempts to solve the two systems independently, the condition numbers of the transform mapping systems 1 to 2 and that mapping 2 to 3 is greater than or equal to the condition number of the system mapping 1 to 3. This proves that, likely, a more stable solution for H_1 and H_2 can be obtained by solving for the less ill-conditioned problem of finding H_{21} and then decomposing H_{21} for H_1 and H_2, rather than for solving for H_1 and H_2 independently.

Practically, one can devise a great number of methods to use this additional (output) information to achieve a stable solution. An efficient method for solving this system would be to first estimate H_{21} and then solve for either H_1 and H_2 based on the estimates of:

$$\left|\frac{\delta I}{I}\right| \Big/ \left|\frac{\delta G}{G}\right|,$$

or;

$$\left|\frac{\delta G}{G}\right| \Big/ \left|\frac{\delta J}{J}\right|,$$

and finally deduce the corresponding system by using the linearity condition in Equation 4-23. This approach is preferable when the relative errors in each of the systems are not the same, which may often be the case. Numerically, however, the decomposition of H_{12} may pose difficulties.

In our application, the relative errors in the input, tissue, and output are relatively the same and thus there is no clear advantage of first solving one and then the other. Therefore, an iterative method was chosen which solves H_1 and H_2 while using the linearity condition in Equation 4-23 as a constraint. This method avoids the pitfalls associated with decomposing the H_{12} matrix while ensuring that the linearity condition between the two systems is maintained.

4.2.3 Methods and Materials

A deconvolution technique based on the concepts generated in the theory section was compared to four commonly used deconvolution methods: exact least squares, Fourier transform, model-based fitting, and constrained optimization with regularization. Because these methods are well known and better described in the literature, a brief discussions of the methods are given with more attention to the details of the algorithm. When possible, only the 'raw data' was used in each of the deconvolution methods. There are two reasons for this. First, any pre-conditioning of the data, such as re-scaling

or manual tweaking of the inversion, may both adversely affect the impulse response estimate and potentially bias any resulting parameters. Second, a method that has as little 'user-intervention' as possible is preferable since in practice, a very large number (100-10000) of deconvolutions are to be performed in succession during tomographic image analysis. All methods were implemented using programs developed on MATLAB numerical analysis software [The Mathworks Inc. Natick MA].

4.2.3.1 Exact least-squares inversion

The exact least-squares method is a direct inversion technique that is generated from the normal equations in the standard fashion [Anton and Rorres, 1987]. The method requires the inversion of the autocorrelation matrix of I, multiplied with the cross-correlation of J and G. For the following sections in this chapter, this method is defined as the 'LS' method.

4.2.3.2 Fourier Transform

In this approach, Fourier transforms, $\Im$, are used to estimate H through:

$$H = \Im^{-1}\left[\frac{\Im[G]}{\Im[I]}\right] \qquad \textbf{Equation 4-28}$$

The Fourier transforms were implemented with a Fast Fourier Transform (FFT) contained within the MATLAB software. To reduce aliasing, data vectors were padded with zeros of length equal to the original data vector before transforms were applied. A number of Butterworth filters with various filter widths and decibel settings were also

tested. No special treatment of the 'DC' components during the transform was performed. For the following sections, this method is defined as the 'FFT' method.

4.2.3.3 Model-based fit

Here, it is assumed that the estimated impulse response function, $\hat{H}_1$, for system 1 has the form of a gamma-variate function:

$$\hat{H}_1 = A(t-\tau)^n e^{-(t-\tau)/T_p}, \qquad \textbf{Equation 4-29}$$

with unknown amplitude, A, relaxation parameter, T_p, and power factor, n. All parameters are assumed to be bound on the set of positive real numbers. Then a minimum to the following scalar function:

$$\xi = \sum \left[\frac{G - I \otimes \hat{H}_1}{\sigma_2} \right]^2 \qquad \textbf{Equation 4-30}$$

is sought, where ξ is the goodness-of-fit measure. The values of F, A and T_p are bound on the set of real-positive numbers and the minimization is implemented using a simple line-search. The minimum and maximum step-sizes for each trial parameter were fixed at 0.0001 and 1.0, respectively. For the following sections, this method is defined as the 'FIT' method.

4.2.3.4 Optimization using regularization

By treating the convolution integral as an inverse problem, a minimum of the following scalar function:

$$\xi = \chi^2[\hat{G}] + \lambda\Omega[\hat{H}_1], \qquad \textbf{Equation 4-31}$$

is sought, where χ^2 is a chi-squared functional and Ω is a regularizing functional with regularizer λ, and $\hat{G}$ is the estimated tissue response obtained by a convolution of the trial impulse response, $\hat{H}_1$, and input function I. In this implementation, χ^2 is the weighted sum of the squares between the output function and the convolution of the trial function with the input function. The regularizing functional selected was the norm of the Hessian matrix multiplied by the trial function. By selecting such a regularizer, it is assumed the first derivative of the impulse response function is smooth. Because the cost function is a bound-quadratic, any minimum is assured of being the global minimum when the correct value of λ is used [Hovorka *et al.* 1998]. Despite the assurance of a global solution, the selection of λ proves to be a non-trivial task [De Nicolao and Liberati 1993]. There are several methods of finding the optimal choice of λ. In this implementation, the discrepancy principle is employed, which assures equal weighting between the chi-squared functional and regularizing functional. The minimization is implemented with a line-search using minimum and maximum step-sizes for each trial parameter fixed at 0.0001 and 1.0, respectively. For the following sections, this method is defined as the 'REG' method.

4.2.3.5 Constrained optimization using input, tissue and output curves

To solve for $H_1(t)$ and $H_2(t)$ the optimization toolbox described above, where the trial function is a 2 x N matrix, is used. In its implementation, a cost function, ξ_{12}:

$$\xi_{12} = \chi^2[\hat{G}] + \lambda_1\Omega[\hat{H}_1] + \chi^2[\hat{J}] + \lambda_2\Omega[\hat{H}_1] + \chi^2[I \otimes \hat{H}_1 \otimes \hat{H}_2 - J],$$

Equation 4-32

is employed in the minimization, and $\hat{J}$ is the estimated output function, based on the trial impulse response function $\hat{H}_2$. Note that this cost function is identical to that defined in the constrained regularization, with an additional term that uses the linearity in H_1 and H_2 to constrain the form of the trial impulse response functions. The regularization parameters, λ_1 and λ_2, were each determined from the discrepancy principle. Values of the trial functions were bound on the set of real-positive numbers. The minimization is implemented using line-search using minimum and maximum step-sizes for each trial parameter fixed at 0.0001 and 1.0, respectively. For the following sections, this method is defined as the 'REG2' method.

4.2.3.6 Numerical simulations

The interest in deconvolution is motivated by their implementation in f-CT studies in highly perfuse organs, such as the lung. In these studies, contrast injections are sharply defined with the rise and fall of tissue contrast concentration within a matter of a few seconds. A number of computer simulations were conducted to test the accuracy of each of the aforementioned deconvolution method.

The input CT-concentration curve, I, of the pulmonary artery was digitized from Ono *et al.*, who administered an antecubital Iodinated contrast injection for 5 second at 4 ml/s (see Figure 5-2). Figure 4-2 describes the two test impulse functions, H_1 and H_2, used in the simulations. Note that the magnitudes of the impulse response functions are different in order to achieve the relative magnitudes in the expected signals in the lung tissue and draining vessel. The shape of this curve is similar in shape to the test

functions used in other papers testing deconvolution methods [Madden *et al.* 1996]. The functions G and J were then obtained by convolution of the test impulse functions with the input function I. Pseudo-random noise, sampled from a normal distribution centred about the origin, was added to each data point in the functions I, G and J (see Figure 4-3) with σ equal to 0, 10, 50 and 100. One hundred simulated data-sets were deconvolved at each noise level and the best estimate of the impulse response function, $\hat{H}_1$ and $\hat{H}_2$ were determined from the average of these results. Because the noise is gaussian, one expects the error in the impulse response functions to be approximately $100^{-1/2}$, or 10 %.

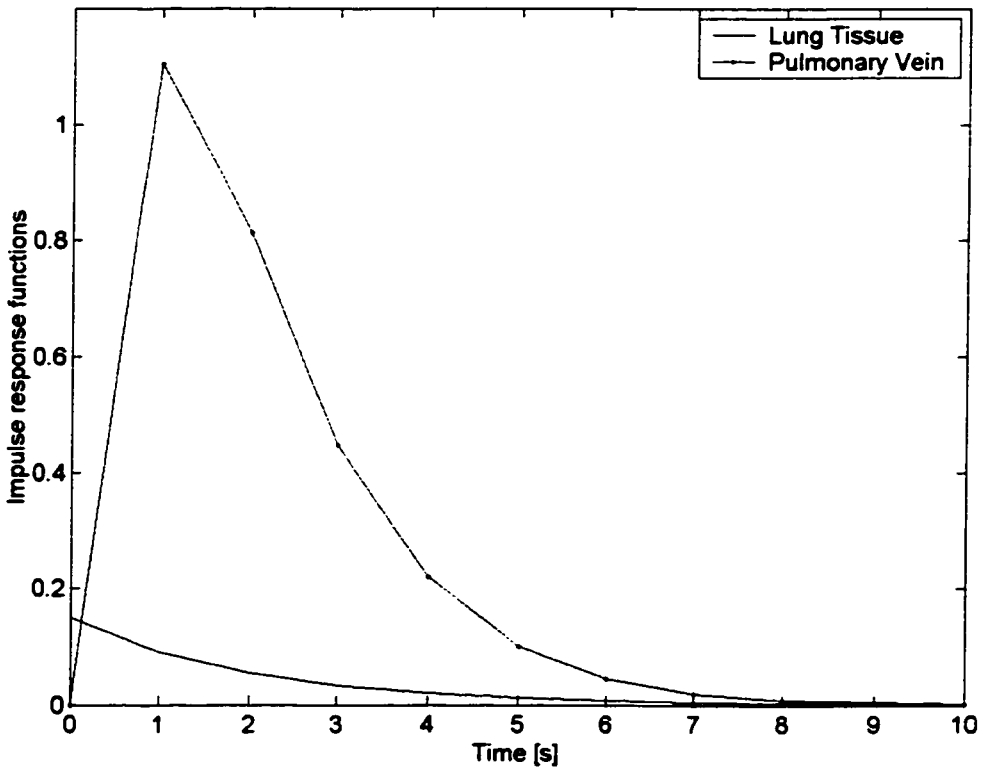

Figure 4-2: Impulse response of tissue and output signals.

Metrics defined by Madden *et al.* (1996) were used to assess the quality of the deconvolution. To estimate goodness-of-fit between the estimated, $\hat{H}$, and simulated, H, impulse response functions, a chi-squared statistic was computed:

$$\mu_1 = \left\| H - \hat{H} \right\|^2 .$$

This statistic is the most direct and least confusing method of comparing the closeness of match between the estimated and theoretical impulse response function for each of the deconvolution methods. This assumes that each point in the time-series is as equally important. Also computed was the statistic:

$$\mu_2 = H(t_i) - \hat{H}(t_i) . \qquad \textbf{Equation 4-33}$$

Because 30 points were used in the time-series, each estimate produces 30 values, which are then averaged over the 100 simulations to give $\overline{\mu_2}$. This is then averaged over the total number of time-series points giving,

$$\overline{\overline{\mu_2}} = \frac{1}{30} \sum_i \overline{\mu_2(t_i)} . \qquad \textbf{Equation 4-34}$$

The parameter $\overline{\overline{\mu_2}}$ represents the overall bias in the estimate of $\hat{H}$. The last measure estimates the sensitivity of the deconvolution method to the noise through an estimate of the variance:

$$\mu_3 = \frac{1}{n-1} \left(\sum_i \mu_2^2(t_i) - n \overline{\mu_2(t_i)}^2 \right) . \qquad \textbf{Equation 4-35}$$

Each value of $\mu_3(t_i)$ is then summed:

$$\overline{\mu_3} = \sum_i \mu_3(t_i) . \qquad \textbf{Equation 4-36}$$

The parameter $\overline{\mu_3}$ estimates the variation in the solution of each deconvolution method.

Often, the impulse response function is analyzed to yield physiologically meaningful statistics such as the mean tissue transit time (*MTT*) blood volume (*BV*) and flow (*F*) defined by:

$$MTT = \frac{\int_0^{\infty} t \cdot H(t)dt}{\int_0^{\infty} H(t)dt}, \qquad \textbf{Equation 4-37}$$

$$BV = \int_0^{\infty} H(t)dt, \qquad \textbf{Equation 4-38}$$

$$F = \max\{H(t)\}. \qquad \textbf{Equation 4-39}$$

The values of *MTT*, *BV*, and *F* derived from the estimates of the impulse response functions from each of the deconvolution methods were compared to theory.

4.2.3.7 Phantom Experiment

A phantom experiment using a f-CT data set was used to test the utility of the proposed deconvolution method. The experiment consisted of a hollow cylindrical water phantom as in Figure 3-6 (with connective tubing as in Figure 4-1, rather than a rod) with a mixing vessel in the centre connected to input and output tubing. Water continuously flowed through the tubing and mixing vessel and a short 5 second injection of Iodinated contrast was introduced at the input. The phantom was scanned in the axial plane such that the input, mixing vessel and output signals were within the scanning plane. The images were obtained with a Marconi PQ5000 CT scanner at one second

intervals while the contrast flowed through the input, mixing vessel, and output [Marconi Medical Systems, Essex UK]. Because of the complex geometry of the mixing vessel and difficulties in maintaining a constant flow rate, the theoretical impulse response functions could not be computed. However, the system is closed and passive and thus the impulse response function must be a positive function. Preliminary observations and tests using colour-dye suggested that the contrast remains in the vessel for only a few seconds.

The CT images were then exported from the image acquisition station to a personal computer for further analysis. The mean *CT#* of a small region of the input, mixing vessel, and output were obtained for each image in the time-series. Estimates of the impulse response functions H_1 and H_2 were then obtained by performing deconvolution using the methods described earlier.

4.2.4 Results

4.2.4.1 Simulations

Figure 4-3 displays typical values of the input, tissue and output signals in the deconvolution when σ=50 *CT#*. Tables 4-1 to 4-3 display results of μ_1, $\overline{\overline{\mu_2}}$, and $\overline{\mu_3}$. Each of the methods performed very well at the lower noise levels. However, as noise increases, the FFT and REG methods display large errors when compared to the FIT, LS, and REG2 methods.

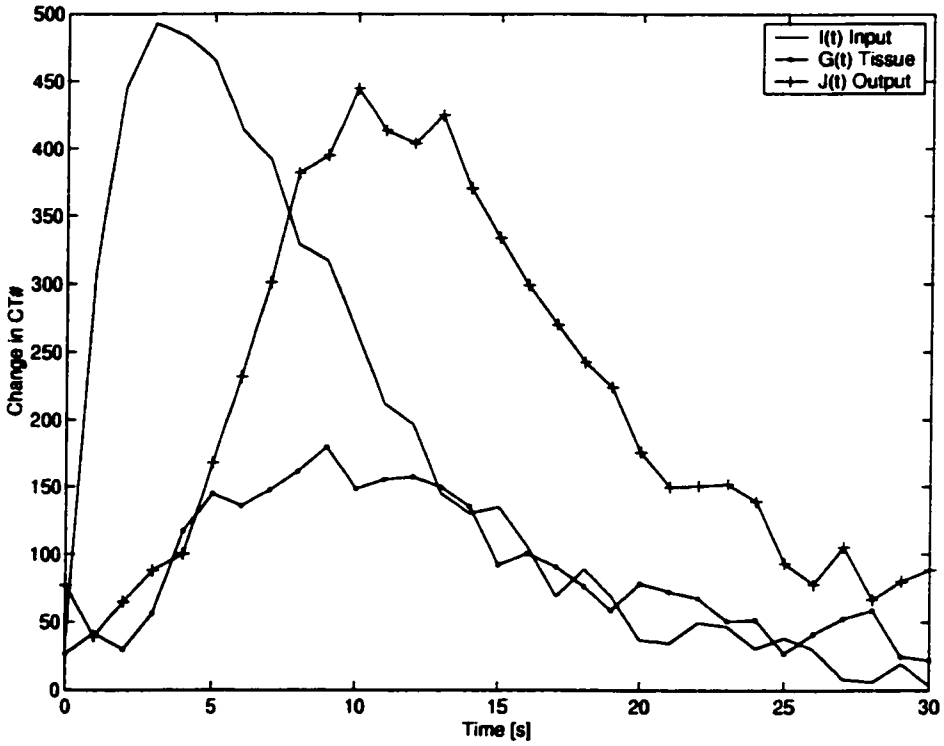

Figure 4-3: Typical simulated data with σ = 50 CT#.

Table 4-1: Values and ranks of μ_1 from each deconvolution method, which measures the goodness of fit in the impulse response function.

	NOISE IN H_1				NOISE IN H_2			
Method	**0**	**10**	**50**	**100**	**0**	**10**	**50**	**100**
LS	116.6 [3]	866.5 [5]	2,802.5 [4]	5,923.0 [3]	15.9 [5]	84.7 [5]	204.9 [4]	380.9 [3]
FFT	114.0 [1]	804.7 [1]	5,726.0 [5]	9,187.8 [5]	15.2 [4]	81.9 [4]	216.4 [5]	444.8 [5]
FIT	116.7 [4]	842.2 [3]	2,432.7 [1]	5,158.0 [1]	6.8 [1]	52.3 [1]	138.3 [1]	280.7 [1]
REG	116.2 [2]	858.0 [4]	2,676.8 [3]	6,318.7 [4]	12.3 [3]	80.6 [3]	190.9 [3]	406.4 [4]
REG2	118.5 [5]	832.3 [2]	2,438.8 [2]	5,411.4 [2]	10.8 [2]	60.4 [2]	155.4 [2]	299.1 [2]

Table 4-2: Values and ranks of $\overline{\overline{\mu_2}}$ from each deconvolution method, which measures the bias in the impulse response function.

Method	NOISE IN H_1				NOISE IN H_2			
	0	**10**	**50**	**100**	**0**	**10**	**50**	**100**
LS	0.6447 [2]	2.0167 [4]	3.6845 [4]	5.8314 [3]	0.2352 [4]	0.6273 [3]	1.0153 [3]	1.3867 [2]
FFT	0.6144 [1]	1.9123 [1]	3.9896 [5]	7.7531 [5]	0.2774 [5]	0.9451 [5]	1.7289 [5]	2.6540 [5]
FIT	0.6475 [5]	1.9914 [2]	3.5147 [1]	5.3497 [1]	0.2168 [1]	0.5844 [1]	0.9701 [1]	1.3834 [1]
REG	0.6463 [3]	2.0179 [5]	3.6889 [3]	5.8423 [4]	0.2195 [3]	0.6755 [4]	1.1460 [4]	1.7363 [4]
REG2	0.6472 [4]	1.9983 [3]	3.5768 [2]	5.5337 [2]	0.2173 [2]	0.5976 [2]	1.0051 [2]	1.4473 [3]

Table 4-3: Values and ranks of $\overline{\mu_3}$ from each deconvolution method, which measures the variance in the impulse response function.

Method	NOISE IN H_1				NOISE IN H_2			
	0	10	50	100	0	10	50	100
LS	1.64 [3]	5.05 [5]	9.14 [5]	14.38 [5]	0.62 [3]	1.55 [4]	2.53 [4]	3.63 [4]
FFT	0.74 [1]	2.23 [1]	3.44 [1]	4.21 [1]	0.62 [3]	1.55 [4]	2.53 [4]	3.64 [5]
FIT	1.64 [3]	4.98 [4]	8.53 [3]	12.36 [2]	0.34 [1]	0.90 [1]	1.27 [1]	1.52 [1]
REG	1.61 [2]	4.95 [2]	8.78 [4]	13.46 [4]	0.63 [5]	1.12 [2]	2.20 [3]	3.30 [3]
REG2	1.65 [5]	4.95 [2]	8.51 [2]	12.63 [3]	0.50 [2]	1.28 [3]	2.06 [2]	2.84 [2]

As expected the model-based fit provides the best rankings. Not only do the solutions from the fit produce a better match with the simulated data, the solutions are also less biased and more stable. Clearly then, if the nature of the impulse response function is well understood, then model-based fitting would be the deconvolution method of choice.

If very little is known about the form of the impulse response function, non-model based deconvolution methods must be used. Based on rankings of μ_1, $\overline{\mu_2}$, and $\overline{\mu_3}$, the REG2 method out-performs all other non-model based methods at most noise levels. The FFT method achieves slightly more stable solutions at various noise levels and better estimates from the FFT method could be achieved with customised filtering.

Table 4-4: Percent error and ranks in estimates of mean transit time (MTT).

Method	NOISE IN H_1				NOISE IN H_2			
	0	10	50	100	0	10	50	100
LS	-6.9% [5]	5.8% [2]	29.0% [2]	105.2% [3]	-18.7% [2]	-5.7% [2]	-9.6% [2]	-18.7% [2]
FFT	5.2% [4]	16.2% [4]	82.9% [4]	68.5% [1]	58.9% [4]	8.5% [3]	35.2% [4]	58.9% [4]
FIT	-0.7% [1]	13.9% [3]	33.9% [3]	70.1% [2]	6.2% [1]	13.6% [4]	8.9% [1]	6.2% [1]
REG	-2.3% [2]	45.8% [5]	145.4% [5]	518.6% [5]	195.5% [5]	112.1% [5]	152.0% [5]	195.5% [5]
REG2	-2.6% [3]	4.4% [1]	27.1% [1]	127.6% [4]	39.0% [3]	3.6% [1]	16.7% [3]	39.0% [3]

Table 4-5: Percent error and ranks in estimates of flow (F).

Method	NOISE IN H_1				NOISE IN H_2			
	0	10	50	100	0	10	50	100
LS	0.4% [3]	116.1% [5]	290.1% [5]	513.5% [5]	-64.5% [2]	-40.0% [2]	-10.0% [2]	29.2% [3]
FFT	-0.9% [5]	-22.9% [2]	17.9% [1]	67.6% [1]	-81.7% [3]	-60.8% [4]	-45.8% [4]	-28.7% [2]
FIT	0.2% [1]	-0.7% [1]	208.9% [3]	323.8% [3]	-59.4% [1]	-31.7% [1]	-4.4% [1]	45.0% [4]
REG	-0.7% [4]	110.6% [4]	266.5% [4]	463.3% [4]	-97.4% [5]	-94.8% [5]	-93.2% [5]	-90.1% [5]
REG2	0.2% [1]	87.3% [3]	193.1% [2]	316.7% [2]	-73.5% [4]	-55.1% [3]	-32.7% [3]	-9.0% [1]

Table 4-6: Percent error and ranks in estimates of blood flow (BV).

Method	NOISE IN H_1				NOISE IN H_2			
	0	10	50	100	0	10	50	100
LS	-40.4% [5]	23.5% [2]	100.3% [1]	192.5% [1]	-60.3% [4]	-19.5% [2]	23.5% [2]	68.7% [1]
FFT	-4.0% [4]	100.6% [3]	326.4% [5]	700.0% [5]	-47.2% [1]	43.4% [4]	128.0% [5]	233.8% [5]
FIT	-0.5% [1]	1.8% [1]	231.1% [2]	383.0% [2]	-60.1% [3]	-20.1% [3]	22.9% [1]	69.1% [3]
REG	-0.7% [2]	109.4% [5]	258.6% [4]	445.5% [4]	-94.3% [5]	-88.0% [5]	-79.5% [4]	-68.7% [1]
REG2	-0.5% [1]	105.5% [4]	239.5% [3]	402.2% [3]	-60.0% [2]	-18.1% [1]	27.2% [3]	77.6% [4]

The comparison between theory and the parameter estimates suggest similar results (see Tables 4-4 to 4-6). Again, the FIT method achieves the most accurate parameter estimates and the REG2 method out-performs the other non-model based methods in estimating *MTT* and *F*. The LS method performs very well at estimating the *BV*, but poorly at *MTT and F*. For all non-model based deconvolution methods, the REG2 method appears to consistently provide the least error in all parameter estimates.

Estimates of H_1 and H_2 when $\sigma = 0$ and 100 are displayed in Figures 4-4 through 4-7. Note that the quality in the estimates of impulse response functions differ. In estimating H_1, all methods apart from the FFT method appear to perform well when there is no noise. In the presence of noise though, the FFT method appears to perform well. In estimating H_2, the FIT and LS methods perform quite well at both noise levels. The REG2 method appears to perform relatively well in both of these situations. It appears that some methods are better at estimating the impulse response function under different noise settings and with different forms of the impulse response function.

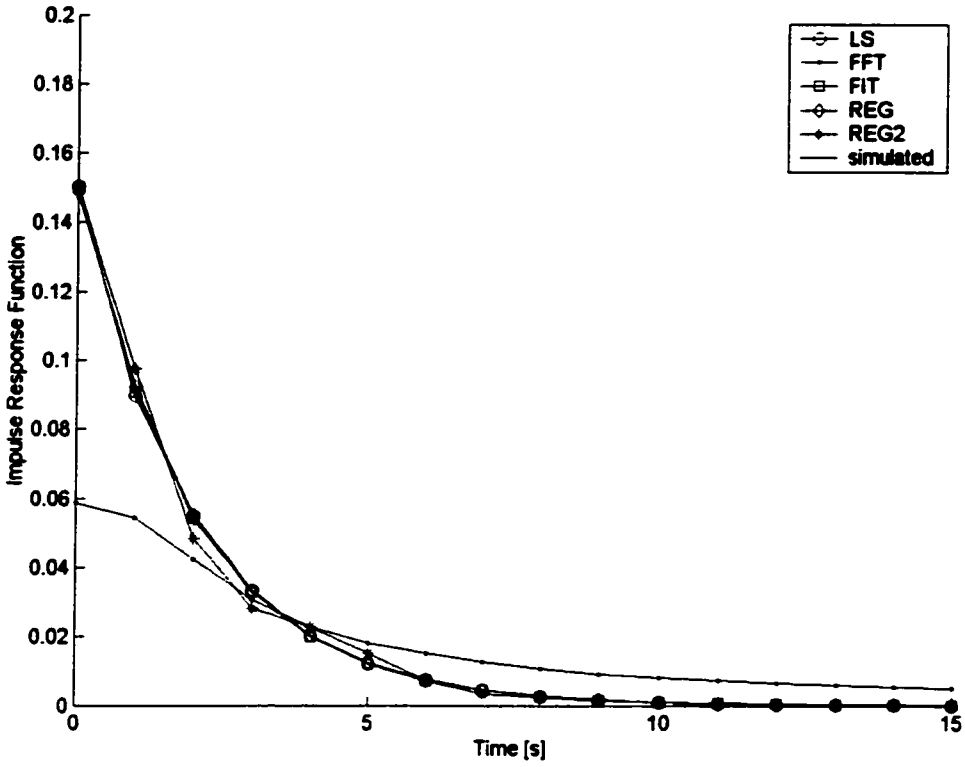

Figure 4-4: Estimated impulse response of H_1 with $\sigma = 0$ *CT#*.

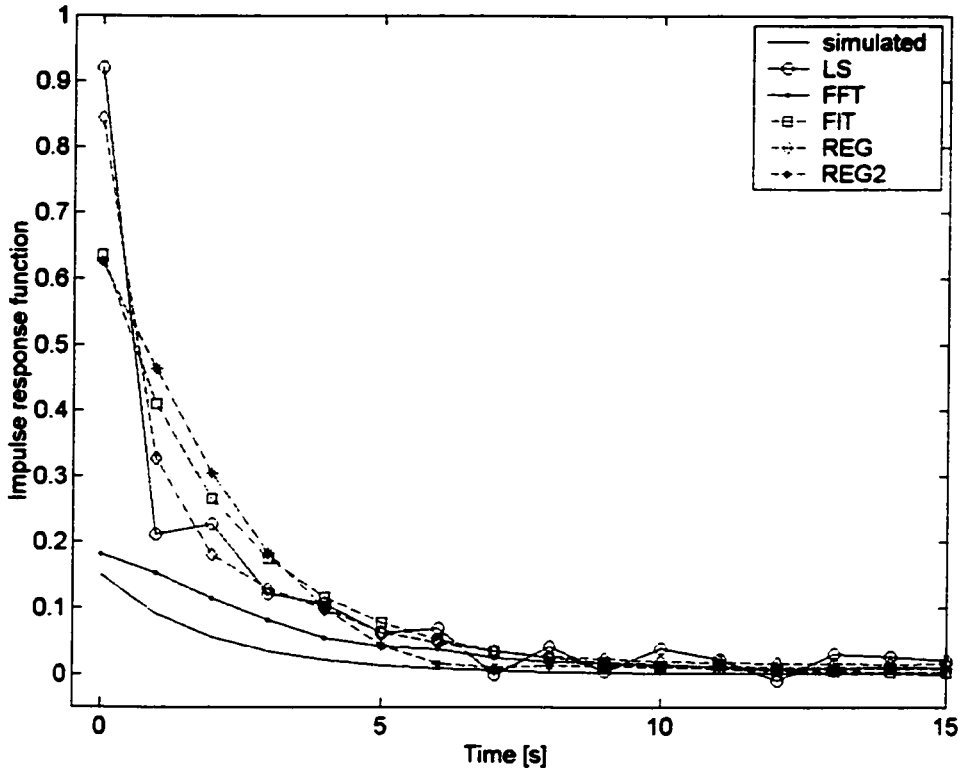

Figure 4-5: Estimated impulse response of H_1 with $\sigma = 100$ *CT#*.

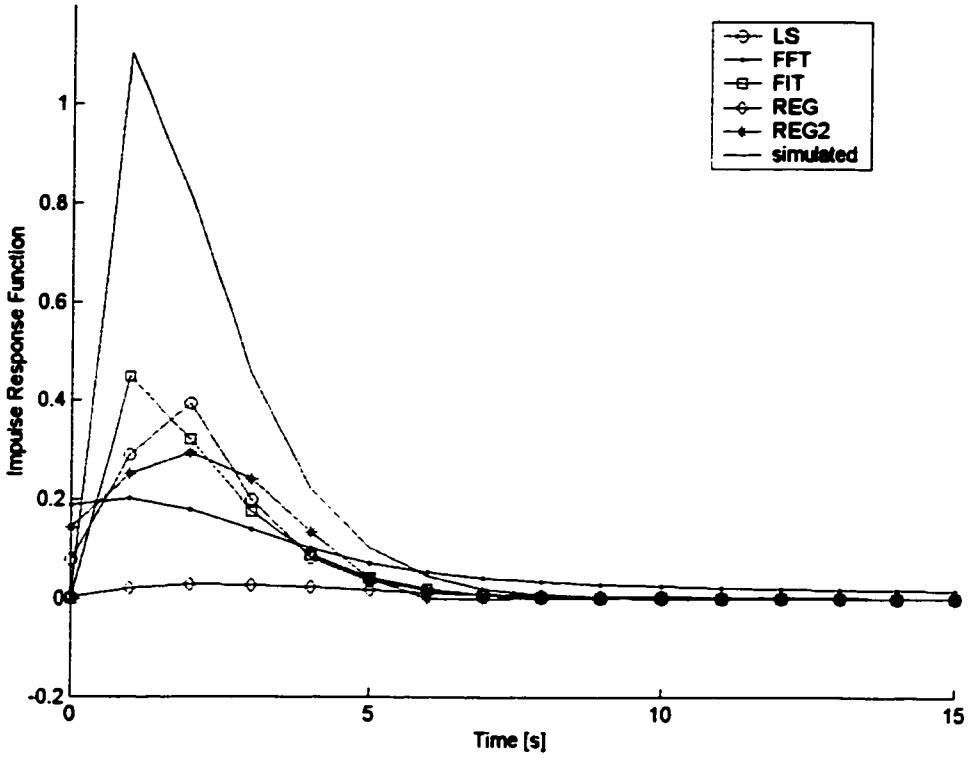

Figure 4-6: Estimated impulse response of H_2 with $\sigma = 0$ *CT#*.

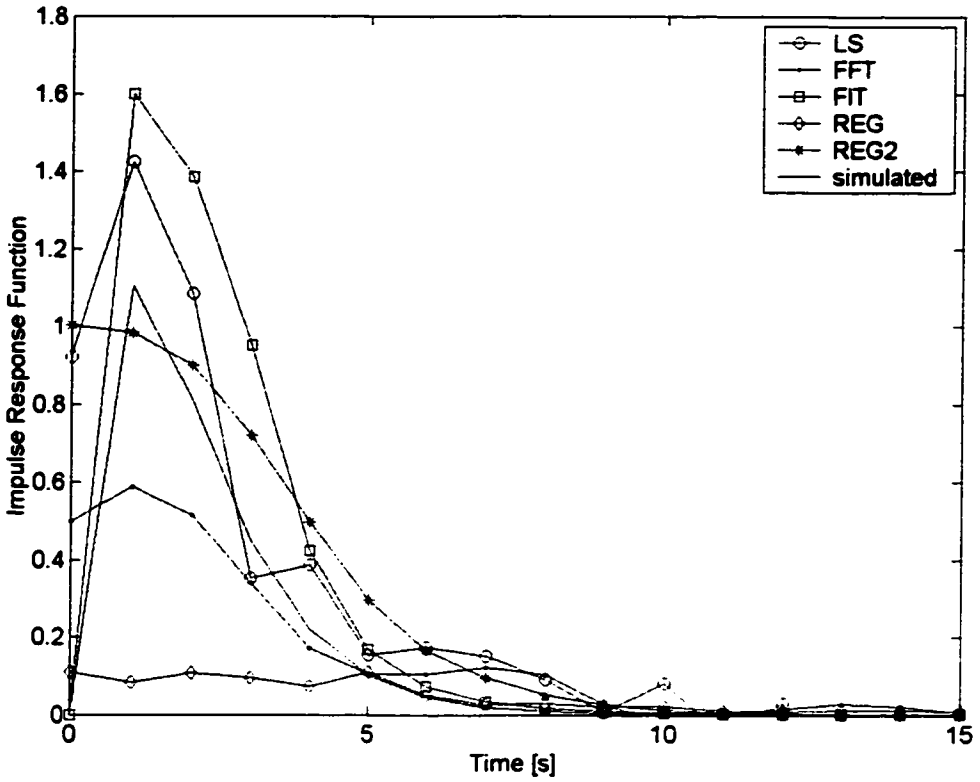

Figure 4-7: Estimated impulse response of H_2 with σ = 100 *CT#*.

4.2.4.2 Phantom Experiment

To generate the time-series functions from the f-CT data set, small regions of interest (ROI) were drawn on the input (I), mixing vessel (V), and output (O) vessels. An ROI of approximately 13 mm^2 was used to define the input, vessel and output vessels. Figure 4-8 displays the measured *CT#* signals as a function of time for the phantom experiment. The average standard deviations for the input, mixing vessel, and output signals, which were all too small to plot, were approximately 10, 14, and 11 *CT#*.

Because the impulse response functions in this system are unknown, the forms of the estimated impulse response functions and the estimates of the vessel and output signal were compared for each of the deconvolution methods. The estimates of the vessel and output response functions are displayed in Figures 4-9 and 4-10. Note the oscillatory behaviour of the LS deconvolution for both response functions. The LS, FFT, REG and REG2 methods seem to suggest that a secondary peak occurs in the vessel response approximately 10 seconds after the initial arrival of the signal. This secondary peak cannot be observed from the model-based fit, since the gamma-variate is a uni-modal function. As for the output response, one would expect a uni-modal and sharply decaying function since there is very little mixing between the vessel and the output tubing. This appears to be observed in all estimates of the impulse response function, with the exception of the LS method.

The difference between the estimated and measured vessel and output are displayed in Figures 4-11 and 4-12. The chi-squared errors between the estimated and measured vessel for the LS, FFT, FIT, REG, and REG2 methods are 1335, 1.128×10^6, 3.401×10^4, 3068, and 5233, respectively. The chi-squared error between the estimated and measured output for the LS, FFT, FIT, REG, and REG2 methods are 1241, 1.551×10^6, 7.649×10^4, 4.109×10^6, 1.019×10^4 and respectively.

Here, the LS method produces the best fit between the estimated and measured signals. However, the forms of the impulse response functions are not physically meaningful since they oscillate wildly. In contrast, the vessel response estimates from the FIT and FFT appear to be physically meaningful, but do not achieve a good match

with the vessel signal. The output response estimates from the FFT and REG methods also appear to be physically meaningful but also do not achieve a good match with the output data. Only the REG2 method provides physically meaningful estimates of the vessel and output response functions while also maintaining a good match with the measured data.

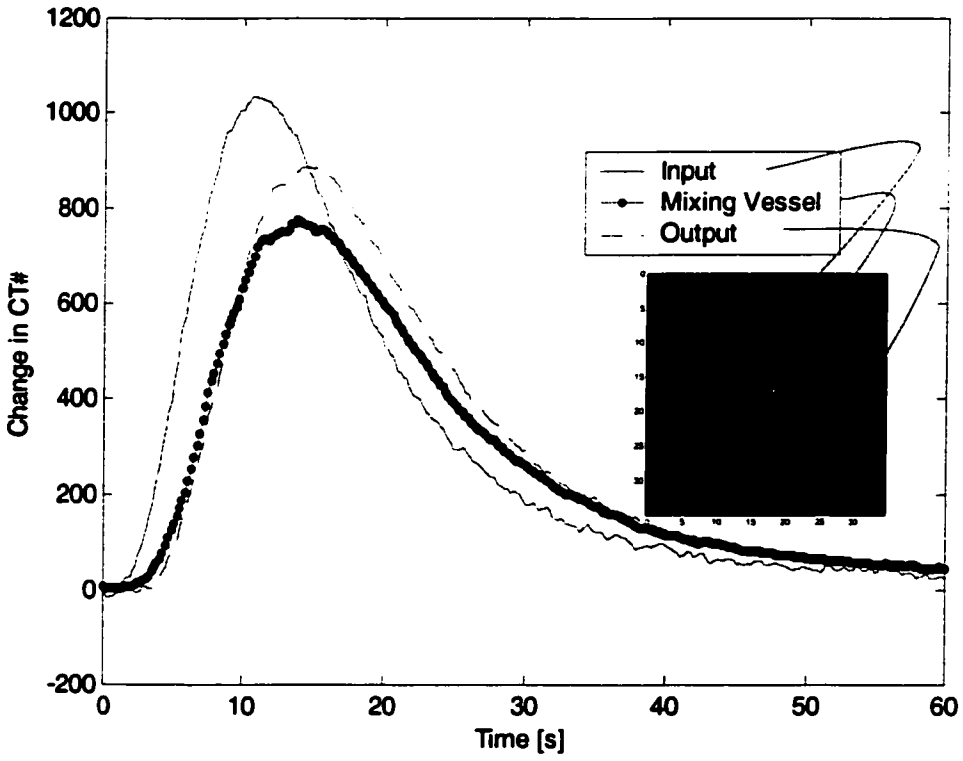

Figure 4-8: Measured input, mixing vessel and output signals from phantom experiment.

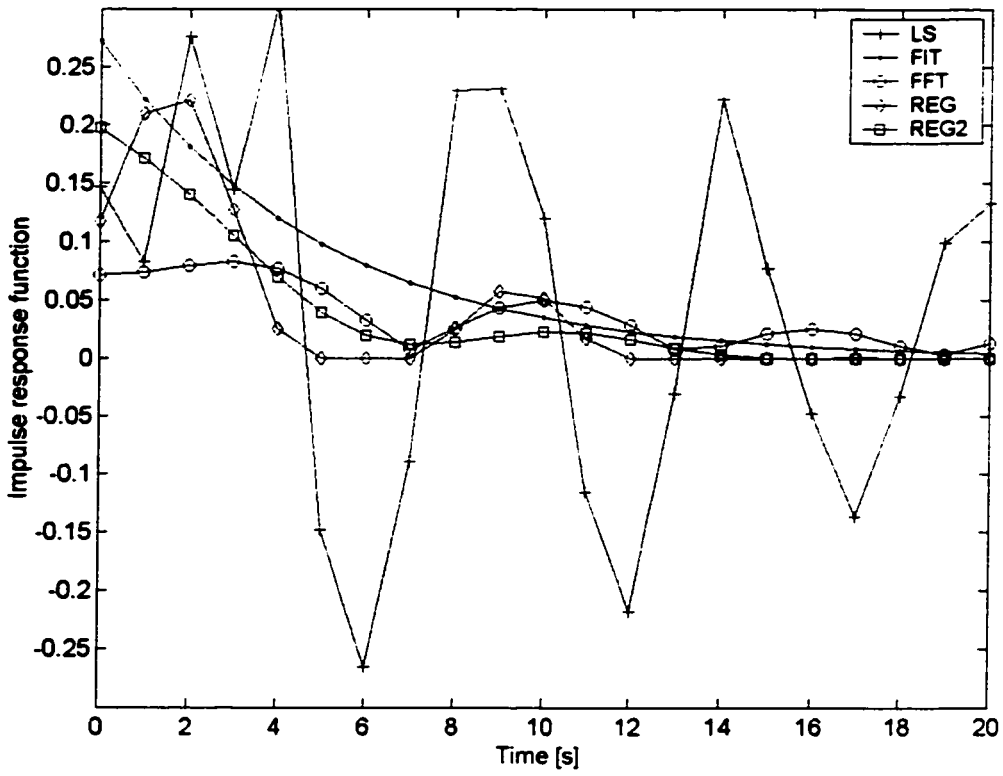

Figure 4-9: Estimated vessel response function of phantom experiment.

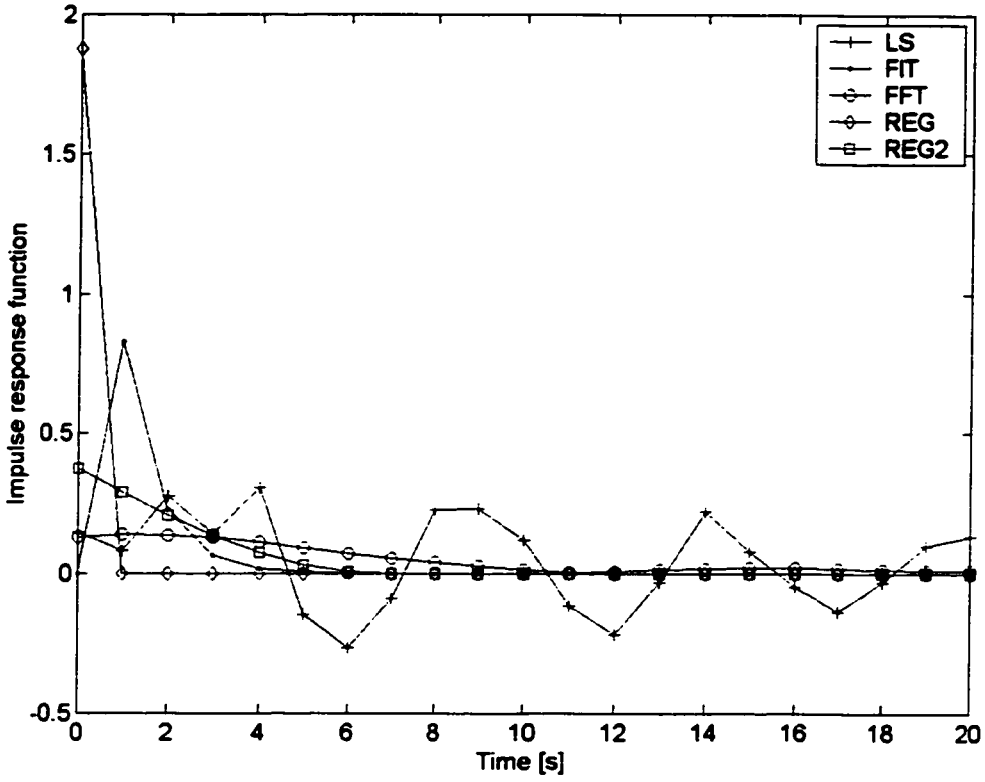

Figure 4-10: Estimated output response function of phantom experiment.

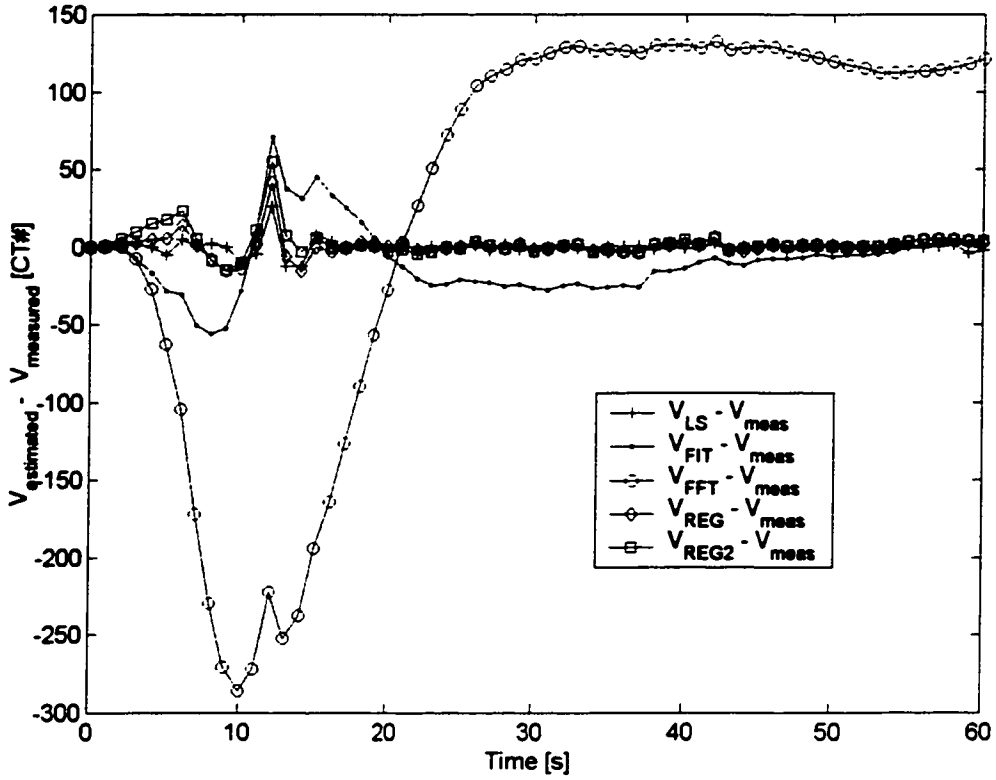

Figure 4-11: Difference between measured and estimated vessel response.

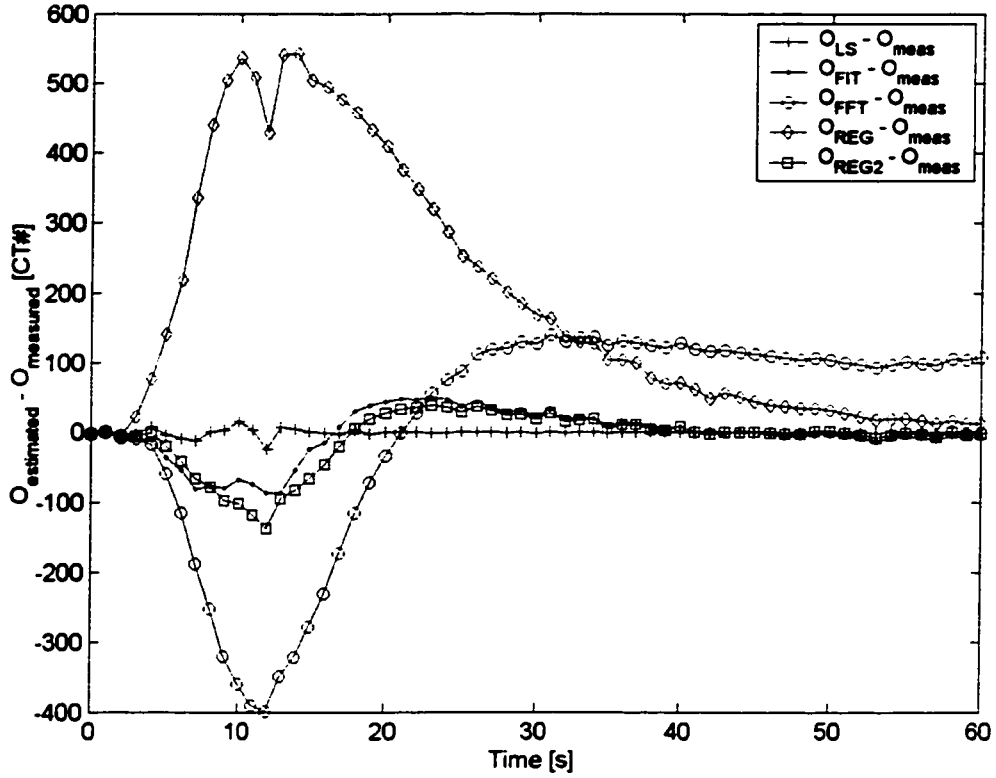

Figure 4-12: Difference between measured and estimated output response

4.2.5 Discussion

Based on ranking, the FIT method out-performs all non-model based deconvolution methods. Of the non-model based deconvolution methods, the REG2 method consistently achieves a good match between measured and estimated output while also producing physically meaningful forms of the impulse response function.

As illustrated, the REG2 method prefers smoother solutions and may introduce bias. This bias, however, is most likely from the incorrect selection of the regularization parameter [De Nicolao *et al.* 1994]. The discrepancy principle is not a very sophisticated

method to determine the value of λ and more precise methods such as the L-curve method, which assures a global minimum in the cost function, may also be applied [Hansen and O'Leary, 1993]. Inherently, the regularization prefers smoother solutions and thus the deconvolution method is biased. More precise methods of selecting λ may reduce this bias.

Despite the apparent goodness of fit of the output curve, the parameter estimates yielded from the result of the deconvolution may be erroneous. These results suggest that certain deconvolution methods may be better at estimating certain parameters. Regardless, special care must be taken when interpreting parameter estimates obtained from deconvolution.

One practical drawback of the REG2 method is increased computation time. The REG2 method takes approximately 4 times longer than the REG method. On a PC operating at 300 MHz, the REG2 method takes approximately 60 seconds per deconvolution. In contrast, the results from the LS and FFT method are almost immediate. However, with everyday increases in processing speed, the difference in computing times for the REG and REG2 method likely will soon become indistinguishable.

There are additional and perhaps more reliable methods of performing non-model based deconvolution, such as system identification, maximum entropy, genetic algorithm, constrained deconvolution using spline basis functions, and other methods [Vadja *et al.* 1988, Charter and Gull 1987, Verrota 1993]. In their comprehensive report of 6 deconvolution methods, Madden *et al.* found that maximum entropy and spline

methods perform well for many forms of the input and impulse response functions. Further, significant improvements to the FFT method may also be devised through customized filtering. It should be noted that the use of output information can be easily incorporated in any cost function and therefore used in maximum entropy, genetic algorithm, or other similar iterative approaches, such as the one described here. The approach outlined here is not intended to replace, but to improve existing deconvolution methods. Note that it is a simple exercise to demonstrate that this formalism above can be generalized for systems greater than two.

5. Feasibility of functional CT in the lung

A number of phantom experiments were performed to assess the feasibility of f-CT in lung. In section 5.1, a variety of phantom measurements and simulations that examine the optimal CT scanning parameters are described. Also described is a method of obtaining as much f-CT data as possible while reducing noise in spiral data sets. The results of these findings are presented in section 5.2. Last, in section 5.3 a demonstration of the use of f-CT to measure regional lung perfusion in a patient study is given.

5.1 Methods and Materials

5.1.1 Optimal scanning parameters in lung

In a CT imaging protocol, there are a wide variety of parameters that may be used to ensure a high quality image. Some of the more important parameters available are CT energy (kVp), current (mA), scan time (s), slice thickness, pixel size, and reconstruction algorithm. The selection of parameters is often a reasonable compromise between patient dose and image quality, which are unfortunately competing quantities. For instance, a lower photon energy may increase contrast and result in lower dose, but at the expense of increased noise. Likewise, a higher photon energy may decrease noise, but at the expense of patient dose.

To determine those settings which achieve the highest signal to noise ratios (SNR), CT images of lung phantoms were taken at a variety of tube energies (100, 120, and 140 kVp) tube currents (200, 300, and 400 mAs) and slice thicknesses (3, 5 and 10

mm). Measurements of noise in lung and water were obtained from CT measurements of a RANDO anthropomorphic phantom in the thoracic region [Radiology Support Devices, Long Beach USA]. All CT measurements were performed with a Marconi PQ5000 CT scanner [Marconi Applied Technologies, Essex UK]. The density of the water and lung were approximately 1.00 and 0.30 g/cm^3.

To simulate lung, small styrofoam balls (diameter approximately 1mm) were inserted into a thin vial containing water to produce an average density of 0.33 g/cm^3. The mean and standard deviation of a 30 mm^2 region of interest were calculated using the statistical analysis features available on the CT scanner. A figure of merit (FOM) described by Lee *et al.* was defined as: FOM $=\alpha/\sigma$ where α is the slope of the *CT#*–concentration curve at some tube energy, and σ is the noise, represented as the standard deviation [Kearfott *et al.* 1983, Lee *et al.* 1990].

Because measurements of μ are experimentally difficult to perform in low density materials with reliability, μ was estimated through a series of steps. First, the *CT#*–concentration curve in water at a single tube energy was measured. This was measured with vials of Iohexol-water mixtures, placed in the alignment holes of the anthropomorphic phantom [Omnipaque, Amersham, Little Chalfont UK]. Second, the *CT#*–concentration data for each tube energy was fit with a mono-energetic linear attenuation value. The parameter μ in water could then be estimated by taking the ratio of linear attenuations of Iodine and water at the respective energy.

The linear attenuation of lung given some fixed volume of air, blood, parenchyma, and contrast in the voxel may be estimated by using Equation 3-10 with various amounts of tissue, shown in Figure 5-1.

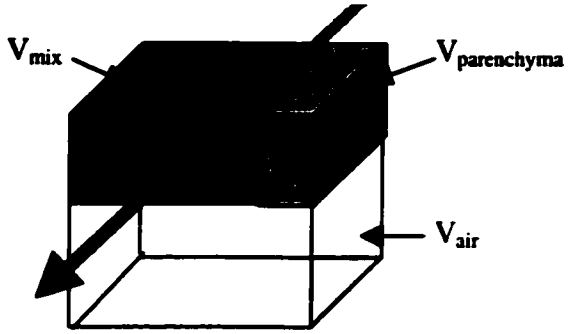

Figure 5-1: Diagram of voxel volumes used in simulation of linear attenuation of lung.

The mass attenuation coefficient in lung is the mass attenuations of the blood-iodine mixture (mix), air (A), and non-contrast enhanced parenchyma (p) multiplied by their respective mass fractions:

$$(\mu/\rho)_{lung} = f_{mix}\,(\mu/\rho)_{mix} + f_A\,(\mu/\rho)_A + f_P\,(\mu/\rho)_P . \qquad \textbf{Equation 5-1}$$

[Johns *et al.* 1983]. But the fractional volume by mass is:

$$f_A = m_A / m_T = [\rho_A V_A] / m_T \text{, and } \rho_{lung} = m_T / V_T . \qquad \textbf{Equation 5-2}$$

Thus:

$$(\mu/\rho)_{lung} = [\rho_{mix} V_{mix}\ (\mu/\rho)_{mix} + \rho_A V_A (\mu/\rho)_A + \rho_p V_p (\mu/\rho)_p] / m_T , \quad \textbf{Equation 5-3}$$

or simplifying:

$$\mu_{mix} = \left(\frac{V_{mix}}{V_T}\right)\left[c_i\left(\frac{\mu}{\rho}\right)_i + c_b\left(\frac{\mu}{\rho}\right)_b\right] + \left(\frac{V_a}{V_T}\right)\mu_a + \left(\frac{V_p}{V_T}\right)\mu_p . \quad \textbf{Equation 5-4}$$

where (μ/ρ), V, and ρ are the mass attenuation, volume and density of contrast (i), blood-Iodine mixture (mix), air (a), and parenchyma (p) and c is the contrast (i) and blood (b) concentration, respectively. Rather than using absolute volumes in the expression, V_i is replaced with the ratio V_i / V_T or v_i, giving the constraint:

$$v_{mix} + v_A + v_P = 1. \quad \textbf{Equation 5-5}$$

Further, note that:

$$\rho_{lung} = \rho_{mix}\, v_{mix} + \rho_A v_A + \rho_p v_p , \quad \textbf{Equation 5-4}$$

or solving for v_A and using the volume constraint:

$$v_A = (\rho_{lung} + \rho_{mix}\, v_P - \rho_p v_p - \rho_{mix}) / (\rho_A - \rho_{mix}). \quad \textbf{Equation 5-5}$$

Thus, one has:

$$\mu_{lung} = (1 - v_A - v_p)\, \mu_{mix} + v_A \mu_A + v_p \mu_p . \quad \textbf{Equation 5-6}$$

where v_A is defined as a function of v_p and ρ_{lung}. From this, it is possible to estimate the linear attenuation of a voxel of lung with various densities, amounts of parenchymal tissue, and concentrations of Iodine. Since the linear attenuation coefficients are a function of the x-ray photon energy, these may be determined through experiments. It is assumed that the linear attenuation of the parenchymal tissue is equal to water. The mass-attenuation coefficients for blood and tissue were approximated with Hubbell's data of photon mass attenuations [Hubbell 1995].

Once the linear attenuation of lung is calculated, it is simple to compute the expected *CT#* by using the formula:

$$CT\# = 1000(\mu_{lung} - \mu_{water})/\mu_{water}. \qquad \textbf{Equation 5-7}$$

The theoretical values of *CT#* were compared against CT measurements in water to verify the model.

5.1.2 Noise reduction via increased sampling of spiral CT images

F-CT analysis requires repeated CT image acquisitions in a single slice of the patient. Because the total number of images in the f-CT is limited to patient's breath-hold duration, each image must be obtained as rapidly as possible. Finite times for image acquisition and gantry rotation limit the sampling rate of axial-CT scans. Higher rates of data sampling may be possible through batch processing of spiral-CT once the raw projection data has been collected. This is done by processing the data with an index less than the slice thickness while keeping the table at a fixed location. Some CT scanners allow spiral data to be collected with no table motion while others, such as the Marconi PQ5000, may not. However, spiral data can be collected with the scanner by deactivating the belt mechanism of the CT couch. By increasing the number of samples taken within a gantry rotation and averaging the samples within the gantry rotation time interval, the noise can be reduced by a factor of $N^{1/2}$.

For example, assuming a total scan time of 30 seconds, a 5 mm slice thickness, and a fixed gantry rotation period of 1 second per scan, 150 CT images can be obtained by processing the data with an index of 1.0 mm. Therefore, five images are acquired within a one second interval, rather than one. If the density estimate in a voxel of the CT image has a noise of σ, then assuming statistical independence, the density estimate in

the averaged data set becomes approximately $0.447\,\sigma$. Note that this statistical independence may not always hold true [Hanson 1979].

5.1.3 Estimating the impulse response in the lung

Maseri *et al.* (1970) used a linear-systems approach to model the pulmonary vascular system to estimate the MTT in 10 anaesthetized dogs. They note that MTT estimates, which ranged from 3.3 to 10.3 seconds, were independent of heart-rate and small movements, but sensitive to re-circulation artifacts.

Assuming a time-invariant and linear system, the impulse response function of the pulmonary vascular system may be modeled with combination of the input, alveolar, and output vessels convolved with the arterial input function. Since the mean-velocity of blood in a CT voxel in both the feeding and draining vessels is significantly higher than that through the alveoli, the impulse response functions in these regions is tightly peaked [Fung 1997]. On the other hand, the transit time through an alveolar sheet is on the order of several seconds [Fung 1997].

The pulmonary response function is, by definition, the measured response of the lung tissue when the input function is a delta function. If one use a delta function as the input function, the measured *CT#* will not be the impulse response function but rather a time-averaged impulse response function. Furthermore, the intensity of the signal will be reduced due to partial volume effects within the lung tissue and air volumes.

Given that the vascular transit time is significantly shorter than the alveolar transit time, St. Lawrence and Lee's Capillary Adiabatic Tissue Homogeneity (ATH) model may be used to model the regional pulmonary impulse response function [St.

Lawrence *et al.* 1998a, 1998b, Fung 1997]. They describe a model that displays both vascular and capillary tissue properties of the tissue of interest by using a Heaviside function plus damped exponential:

$$H(t) = H_v(t) + H_p(t) \qquad \textbf{Equation 5-8}$$

where,

$$H_v(t) = \begin{cases} 1 & 0 \le t \le T_c \\ 0 & t \ge T_c \end{cases}$$

$$H_p(t) = \begin{cases} 0 & 0 \le t \le T_c \\ Ee^{-\frac{EF}{V_E}(t-T_c)} & t \ge T_c \end{cases} \qquad \textbf{Equation 5-9}$$

The ATH model has four independent parameters, T_c (mean vascular transit time), E (extraction coefficient in the parenchyma tissue), F (blood flow), and V_E (volume of contrast in the parenchyma tissue per mass of tissue). Applying this model to the lung, the vascular impulse response function is represented by $H_v(t)$, and the alveolar impulse response function is approximated by $H_p(t)$. The extraction coefficient, E, represents the fraction of indicator retained in the alveolar space during the indicator's transit (which may vary according to the regional distributions of alveolar tissue) within the scanning geometry through the voxel. The parameter V_E, which represents the alveolar volume in the voxel, will vary from zero to a $V_E|_{max} = \rho_{CT}V_{CT}$ since the maximum volume that the alveolar space can attain is the volume of the voxel itself. The blood flow, F, within a voxel can range from 2 ml/s in the pulmonary artery to 0.0001 ml/s in the capillaries [Fung 1997].

This model is similar to the results of Tajik *et al.*(1998), who estimate the impulse response within a CT voxel as the superposition of a fast microvascular transport function plus a slower alveolar transport function, and also the work of Fung and Sobin (Fung 1997) who theoretically modeled the alveoli with a linear combination of a delta function plus two damped exponentials.

Because each voxel will contain blood vessels in a variety of orientations and pathlengths, the vascular transit times will be distributed with some probability density function of width σ_v. Furthermore, the alveolar membranes will have a variety of orientations and pathlengths within the CT voxel and will also be distributed with some probability density function of width σ_A. As a first approximation, it is assumed that σ_v and σ_A are zero.

Since the lung has a dual blood supply, a more accurate description of the response would necessitate an additional compartment in the model fed from the bronchial arteries. In healthy lung, the volume of blood delivered from the bronchial arteries is very small and is ignored in these simulations [Ganong 2001]. It is well known however, that in pulmonary disease this is not true [Littleton *et al.* 1990].

Simulations of the time-density plots were performed using Equations 5-8 and 5-9 to estimate the response of the lung tissue subject to some bolus contrast injection. In addition to variations in the four parameters of the ATH model, the input function, lung density and CT scanning parameters may also vary. Since the procedure of injecting contrast directly into the left atrium used by Tajik *et al.* and Maseri *et al.* is highly

invasive, it is preferable to administer the bolus at a more peripheral site, such as the antecubital vein.

An injection at such a site will cause significant amounts of mixing prior to and within the left atrium, resulting in a bolus distribution which is less peaked. In the input signal from the data of Oguchi *et al.* (1996), who sampled the human pulmonary artery while injecting 50 ml of 300 mgI/ml Iodinated contrast material at a rate of 5 ml/s, the antecubital vein was used. Note that the CT scan parameters in this study were 120 kVp, 200 mA, 3 mm thickness, and 1 second per scan (Oguchi *et al.* 1996). This data was then fit with a gamma-variate curve, $I(t) = 340te^{-t(0.27)}$, and used as an input function in the simulation. Figure 5-2 displays a gamma-variate fit of Oguchi *et al.*'s data during the first-pass of the contrast.

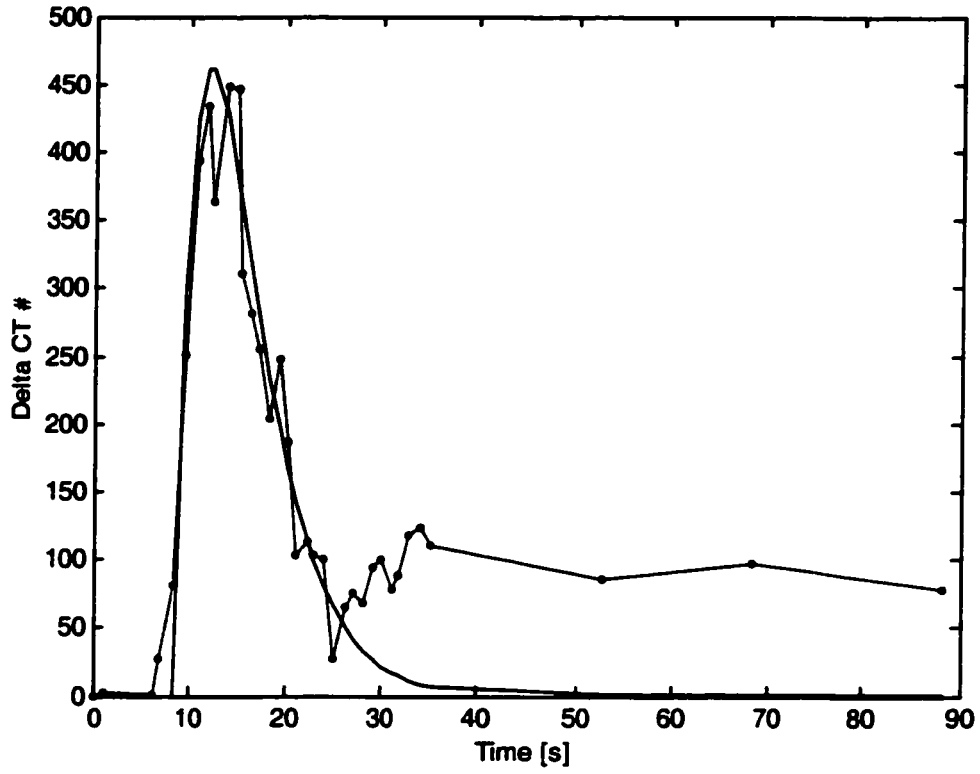

Figure 5-2: Measured and fitted pulmonary artery curve from Oguchi *et al.* (1996)

The input signal was then convolved with a normalized ATH impulse function to obtain the theoretical response in the lung tissue. To estimate the effects of the reduced lung density, assume that the signal in lung tissue is a linear function of the lung density. Since lungs can take on a variety of densities, the parameter α was also obtained theoretically by noting that the linear attenuation of a voxel in the lung may be approximated by:

$$\mu_{mix} = \left(\frac{V_E + V_v}{V_T}\right)\left[c_i\left(\frac{\mu}{\rho}\right)_i + c_b\left(\frac{\mu}{\rho}\right)_b\right] + \left(\frac{V_a}{V_T}\right)\mu_a + \left(\frac{V_p}{V_T}\right)\mu_p \text{ , Equation 5-10}$$

where (μ/ρ),V, and ρ are the mass attenuation, volume and density of contrast (i), blood (b), air (a), parenchyma (p), alveolar (E), vascular (V), and c is the contrast (i) and blood (b) concentration, respectively. Note here that V_E plus V_V is the volume of blood with the voxel and that $V_E + V_v + V_a + V_p = V_T$ is constant. The mass-attenuation coefficients for blood and tissue were approximated with Hubbell's tissue-equivalent values [Hubbell 1995]. Linear attenuation values generated from Equation 5-10 were multiplied by $(1000/\mu_{water})$ to yield a number similar to the CT number. The theoretical values of μ_{mix}/μ_{water} were compared against CT measurements to verify the model.

5.1.4 Reducing motion artifacts with Active Breathing Control

To investigate the reliability of lung position with ABC device during a f-CT study, the position of landmarks on the patient can be tracked in each of the images. External markers can be placed on the patient to measure external displacements, and internal markers were identified to measure internal displacements. To measure external displacements, three thin triangular plastic strips were designed for placement on the patient's sternum and along the sides of the chest wall. To measure in-plane external motion, the absolute positions of the center of the markers were recorded and the maximum difference and standard deviations of the position were calculated. To measure out-of-plane external motion, the areas of the markers were measured. Prior to a study, the area was calibrated against displacement in the cranial-caudal direction. If no external motion in the axial plane occurs, the length of the marker on the CT images

should remain constant throughout the image sequence. If the marker moves in the axial plane, larger or smaller lengths of the marker become imaged.

Let w and l be the half-width and height of the triangle and let the slice thickness be s (see Figure 5-3). Initially, the area scanned is equal to $A = \frac{1}{2} s^2 (w/l)$. If the triangle moves a distance ξ in the axial direction, the area scanned is equal to:

$$A' = \frac{1}{2}(s+\xi)^2\left(\frac{w}{l}\right) - \frac{1}{2}\xi^2\left(\frac{w}{l}\right).$$

Thus, the change in area scanned is $\Delta A = (w/l)s\xi$. In other words, the change in area is proportional to the axial displacement (ξ), the slice thickness (s), and the ratio of the axes of the triangle (w/l). To verify this, triangles with ratios of 1:10, 5, 2, and 1 were measured while the triangles were moved in 1 mm increments.

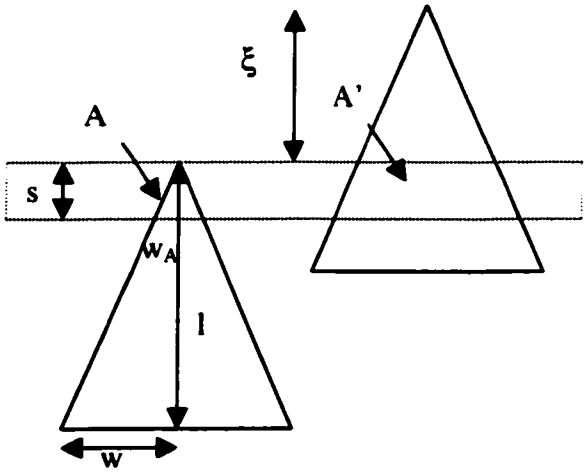

Figure 5-3: Schematic of CT image plane for the reference triangles with axial displacement of ξ.

Since the motion of internal structures is three-dimensional in nature, measuring displacements of the lung tissue is difficult. To measure internal in-plane motion, the absolute coordinates of the apex of the esophagus, and a major vessel in the left and right lung can be recorded. From this, the maximum difference and standard deviations of the position can then be calculated.

5.2 Results

5.2.1 Optimal scanning parameters in lung

Figure 5-4 displays the measured *CT#*-concentration data (displayed with error bars) and the corresponding mono-energetic fits (solid lines). Since beam hardening occurs in concentrations greater than 75 mgI/ml, linear fits were performed in these regions only. Figure 5-4 suggests that the100, 120 and 140 kVp beams can be characterized with mono-energetic approximations of 65, 72 and 78 keV photons, respectively.

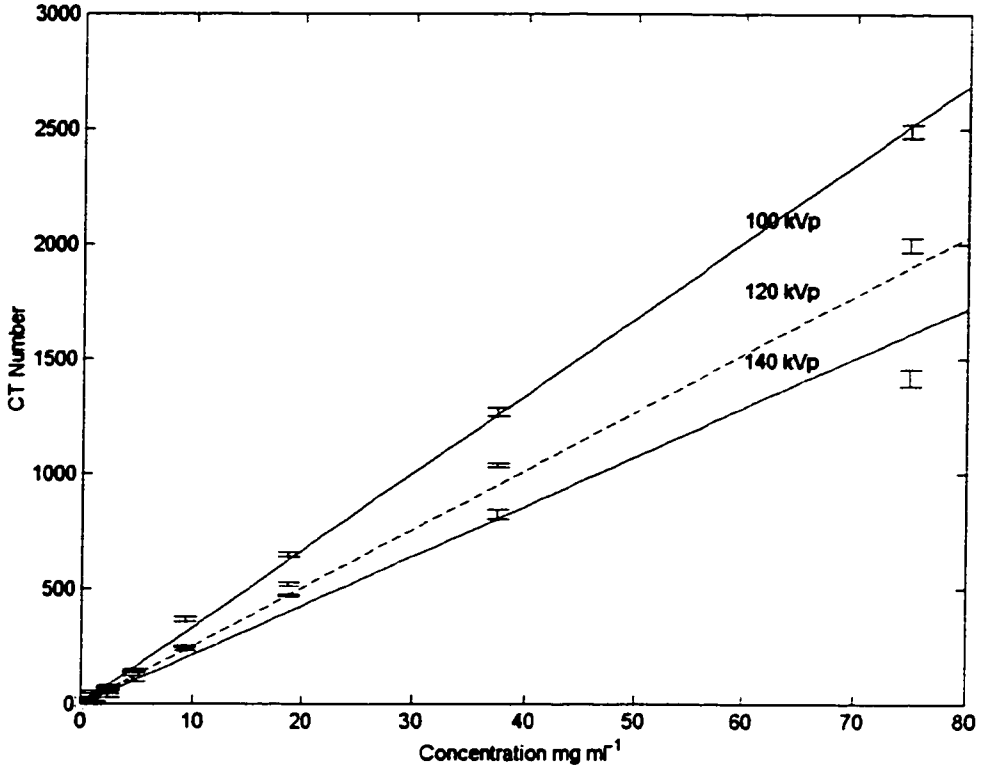

Figure 5-4: Measurements (error bars) and mono-energetic approximations (lines) for three different energies.

Figure 5-5 illustrates the effect of two lung densities for different values of concentration with a 120 kVp source. Since Equations 5-7 and 5-10 demonstrate that *CT#* is linear with concentration and fraction of blood in the CT voxel, it is not surprising that the slope of the *CT#* versus concentration curve in lung is linear. The lighter lines represent the *CT#* if the non-contrast enhanced parenchyma volume constitutes 20% of the CT voxel. The darker lines represent the *CT#* when the parenchyma volume is 0% of the total CT voxel volume. As the parenchyma volume increases, the net density of the CT voxel increases. However, the increased volume of

the parenchyma tissue results in less volume for the contrast. This is illustrated by the reduction of the slope for the larger volumes of parenchyma. During a f-CT procedure, it often is unclear what fraction of the CT voxel contains non-blood flowing volumes. The presence of this non-blood flowing volume may affect the contrast change during a f-CT procedure. The parenchyma volume in healthy tissue is expected to be much less than 20% of the voxel volume. In such circumstances, one may ignore the effect of parenchyma volume on the *CT#* hereafter and note only the small offset in attenuation introduced from the parenchyma tissue. This may not be the case in pathological conditions, such as lung fibrosis or pulmonary edema.

With the mono-energetic approximation in photon energy, the slope (α) of the *CT#* versus concentration curve can be calculated for various lung densities and lung volumes. In the lower density lung, one can expect lower values in attenuation in the lung due to the presence of air.

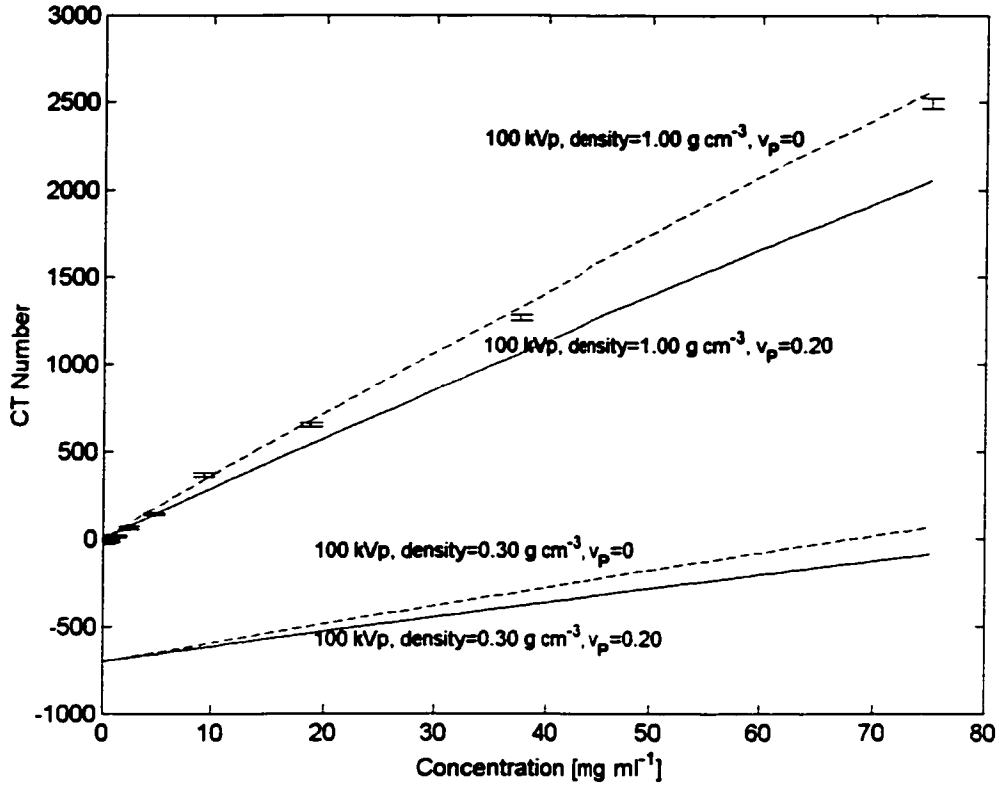

Figure 5-5: Effects of increased parenchyma volume in the *CT#*-concentration relationship.

A table of FOMs is presented in Table 5-1 when the parenchyma volume is set to zero. The FOM results suggest that for typical f-CT scanning, it is advantageous to use lower energies in order to exploit the higher linear-attenuation values.

KVp	Density	α [CT#/mgI/ml]	Noise [CT#]	FOM
100	1.00	32.7 +/- 0.3	9.9 +/- 2.1	3.3 +/- 0.7
100	0.33	10.8 +/- 0.1	3.3 +/- 0.7	3.3 +/- 0.7
120	1.00	25.4 +/- 0.2	6.4 +/- 0.4	3.3 +/- 0.3
120	0.33	8.4 +/- 0.1	2.6 +/- 0.5	3.2 +/- 0.5
140	1.00	21.5 +/- 0.2	6.4 +/- 0.4	3.4 +/- 0.3
140	0.33	7.1 +/- 0.1	2.8 +/- 0.4	2.5 +/- 0.4

Table 5-1: Figure of merit statistic for various photon energies and densities.

In water, these results agree with those found by Lee *et al.* (1990); however in lung, the effect of noise is not as significant as it is in water.

To assess the effects of slice thickness, measurements of noise in lung and water were performed with the anthropomorphic phantom using slice thickness equal to 0.3, 0.5 and 1.0 cm with 120 kVp photons. The respective standard deviation in *CT#* was 3.0, 2.6, and 2.0 *CT#* in lung and 10.2, 6.4, and 5.8 *CT#* in water. Although the change in noise is significantly reduced with large slice thickness in water, the change is less significant in lung. This may be due to a larger number of photons reaching the detector due to decreased attenuation in the lung tissue.

5.2.2 Estimating the impulse response in the lung

Figure 5-6 to 5-8 illustrate the effects of various impulse-response parameters convolved with the input function. The output function was arbitrarily set to begin 2.5

seconds after the beginning of the contrast signal. Apart from the reduction in signal due to reduced density, the most notable feature is the broadening of the response curve as F decreases and T_c or V_E increases. The broadening of the output function will result in a signal whose duration is longer than the input signal. If the f-CT procedure is done under breath-hold, there may be a truncation of data points at the tails of the output distribution. With the exception of very low flow rates, the rise and onset of fall of the output function may be measured within a typical breath-hold scan of 20 s. There is also the potentially significant problem of contrast re-circulation, occurring approximately 15 s after the arrival of contrast. This re-circulation further complicates the data analysis. The intensity of the re-circulation artifact will be significantly lower than the first-pass signal but may still result in an over-estimation of the MTT.

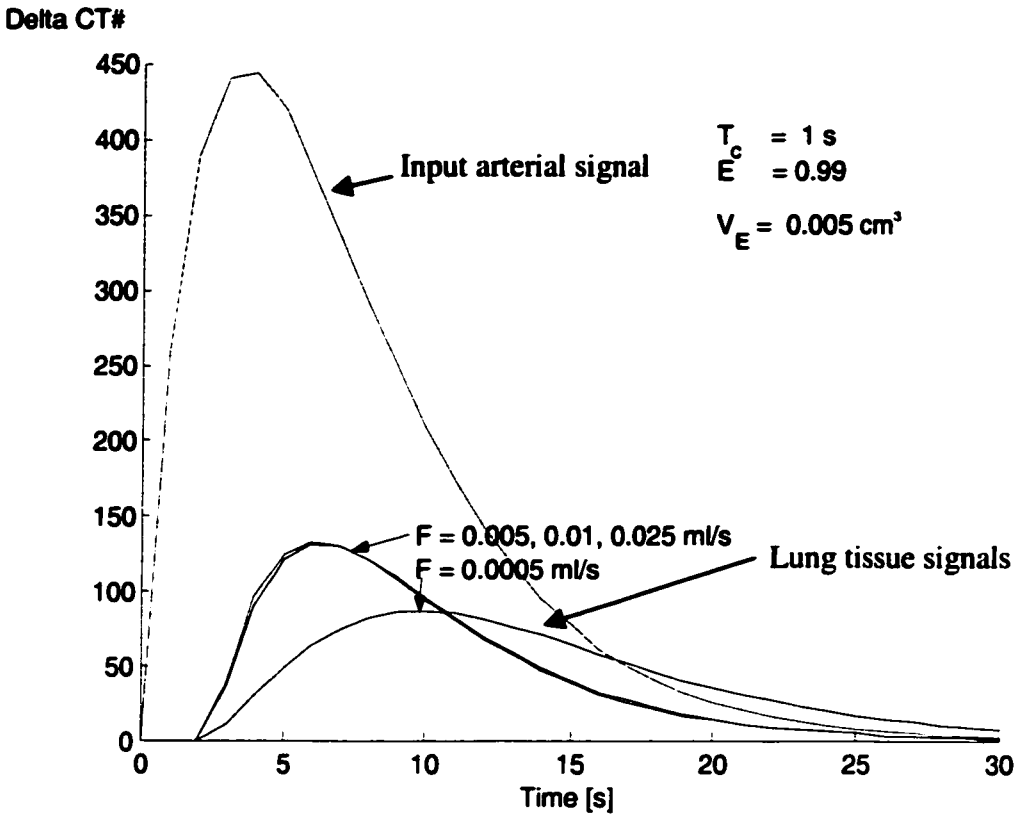

Figure 5-6: Estimate of lung tissue response using ATH model for various flow rates (F).

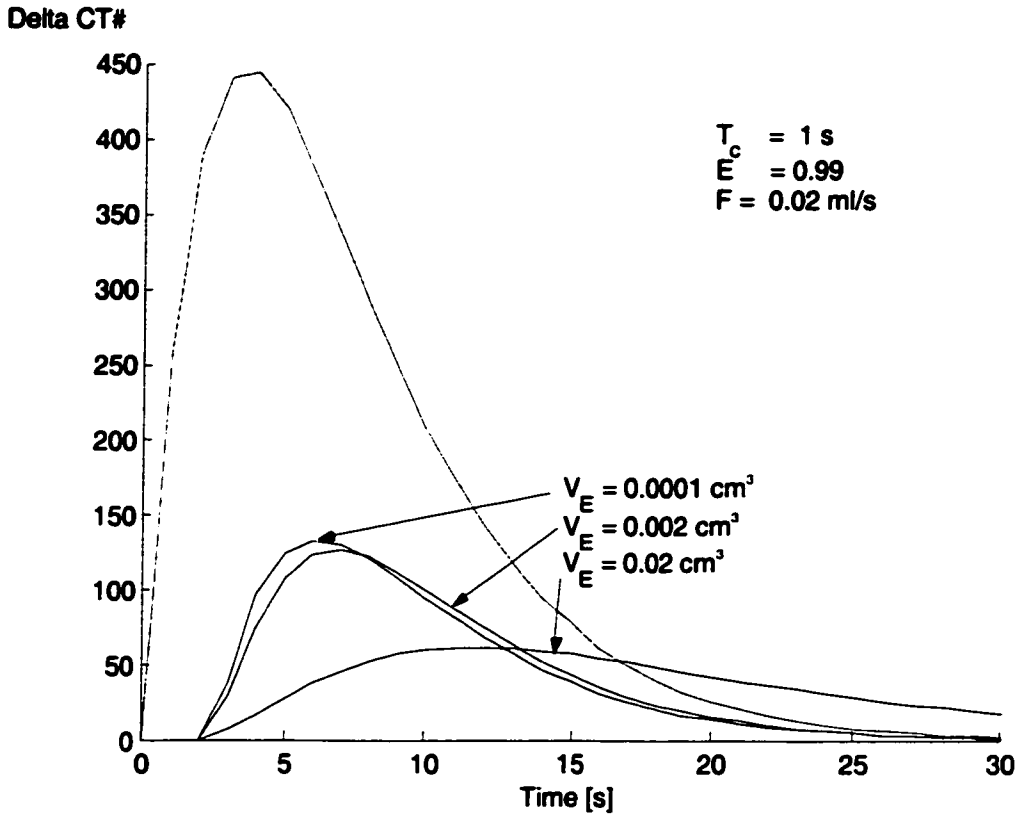

Figure 5-7: Estimate of lung tissue response using ATH model for various extra-vascular volumes (V_E).

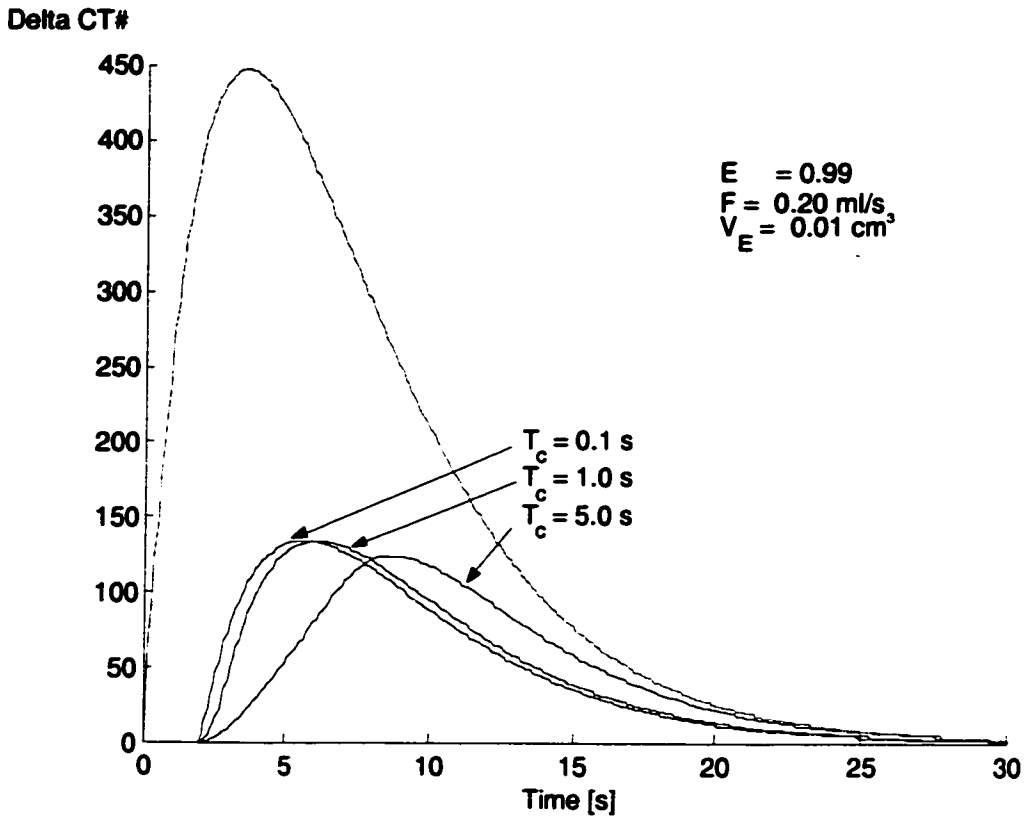

Figure 5-8: Estimate of lung tissue response using ATH model for various mean vascular transit times (T_c).

These simulations suggest that a perfusion signal may not be present in lung tissue when the fraction of vascular blood volume is not greater than 0.02 cm^3.

5.2.3 Reducing motion artifacts with Active Breathing Control

Figure 5-9 shows the measurements of triangle lengths as a function of axial displacement. As expected, each of the triangles exhibits linear behavior. The slopes of these lines represent the change in length, on the CT image, per axial displacement. Obviously, the 1:10 triangles are most sensitive to changes in axial distance. However, the noise associated with the length measurements is large (see Table 5-2). Triangles

with a ratio of 1:5 were used in this experiment as they provided a high 'axial' resolution while also being practical in size.

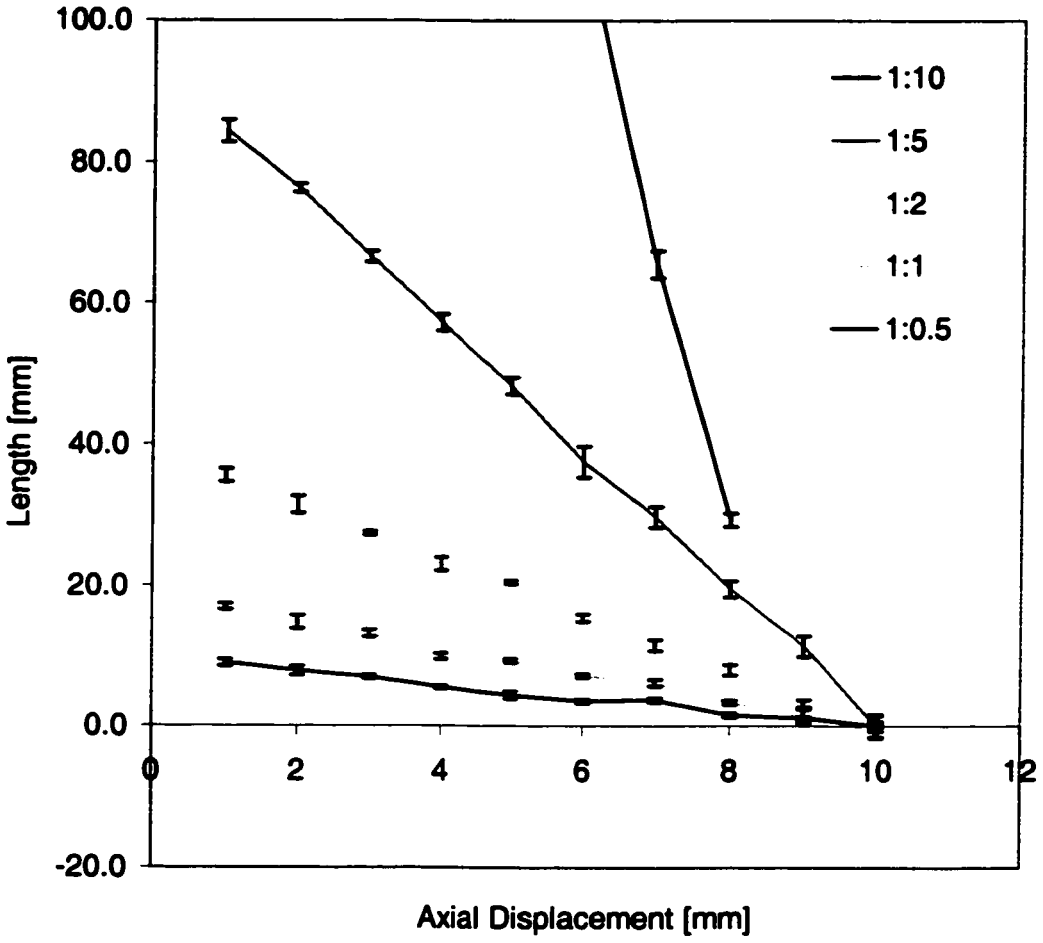

Figure 5-9: Calibration of triangles in the detection of in-plane motion.

Table 5-2: Slopes and errors of different ratios in detecting in-plane motion.

Ratio	Slope [mm_{CT}/mm_{axial}]	Average Error [mm]
1:10	46	3.0
1:5	9.4	1.0
1:2	4.0	0.8
1:1	1.9	0.5

5.3 Clinical example

We briefly present the results of a f-CT study performed on a patient. Consent was received pursuant to our institutional ethics policy. The patient was diagnosed with esophageal cancer and was to receive radiation therapy. The patient was given a 10 minute training session with the ABC device prior to the study and was prepared for an antecubital autoinjection of the contrast agent.

This study was done in conjunction with a routine CT exam for the purpose of radiation treatment planning. The patient was positioned supine on the couch (the treatment position) with arms placed over the head. Because the injection point was not in the field of view, streaking artifacts from the antecubital injection prior to mixing were avoided.

A scout view and full thorax CT image set was taken while using ABC. Then, a slice was selected for the f-CT study near the anterior aspects of the lungs and heart. Once the patient was ready, the patient was instructed to take a deep breath and the

autoinjector, ABC device, and CT were activated simultaneously. The non-ionic Iodine agent with concentration 350 mgI ml^{-1} was delivered at 4 ml s^{-1} for 5 seconds.

The scanning protocol used was 100 kVp, 300 mAs, with 5 mm slice thickness for 30 seconds. Images were acquired for 30 seconds and processed in batch mode such that 5 images were processed within a one second window. The 150 images, each sampled 0.2 seconds apart, were reduced to 30 images by averaging 5 images in a 1 second interval. The images were then exported from the CT scanner to a personal computer for further analysis.

Figure 5-10 displays the cross-section of the f-CT study. The CT values in the lung tissues range from 0-300 *CT#*, with an average of approximately 150 *CT#*. Within the lung volumes, the arterial and venous blood vessels are visible and provide sources of arterial and venous signals in the analysis.

The CT images were processed at 512 x 512 pixels resolution with 0.9375 mm square pixel dimensions. To reduce the effects of motion artifacts and to reduce computation time, the CT images were reduced by a factor of 4, increasing the square pixel size from 0.9375 mm to 3.75 mm. The time series functions from these 'super-pixels' were used in the f-CT analysis.

Through the use of breathing control, displacements of the external chest wall were 0.2 cm in both the medial-lateral and anterior-posterior direction. Motion in the superior-inferior direction was measured at 0.2 cm, which is less than half the slice thickness used in this study. For each of the super-pixels within the lung the signal due to contrast flow was significantly higher than the reference CT signals.

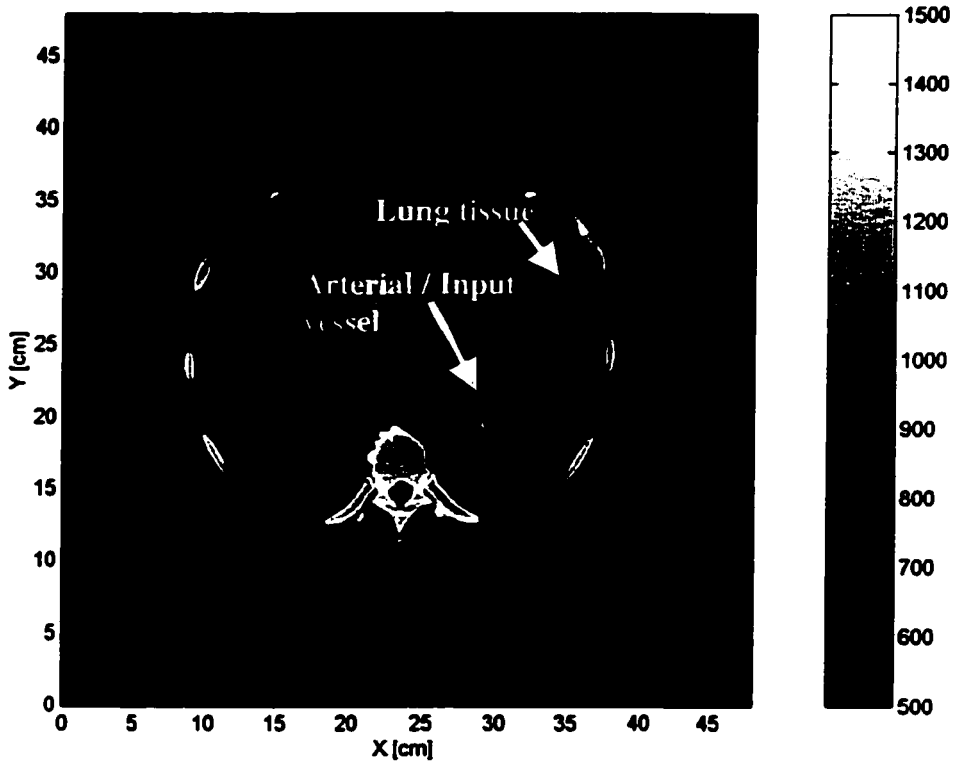

Figure 5-10: A CT image of the patient during the dynamic CT procedure.

Due to a miscalculation in the timing of the imaging sequence and breath hold, the arrival of the contrast material was not measured. Figure 5-11 displays an average of the arterial signals within the lung. This function was obtained manually by examining the time-density curves of small regions of interest such as that shown in Figure 5-10. Also shown is an example of a tissue response signal on the periphery of the lung where large vessels are not present. These functions are the averages of the pixel intensities in a small (9 mm^2) region of interest in the images for each of the images in the time series minus the signal in the non-contrast enhanced (reference) image. Also displayed are the

standard deviations of each of the measurements. The lung tissue signal is typical of the signals observed in lower density regions of the lung.

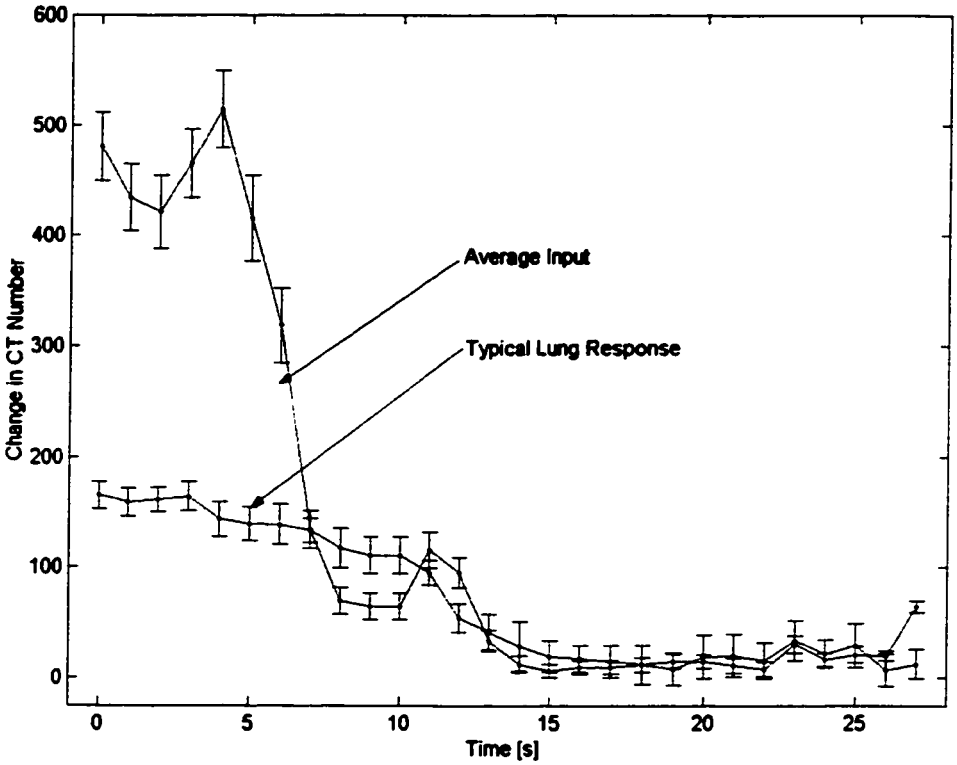

Figure 5-11: Arterial and lung tissue signal within the lung.

The image data was then re-sampled to a super-pixel data set for further analysis. It is assumed that the shape of the arterial input function is similar to the shape of the true input function feeding the lung tissue. Diffusion of the concentrate from the pulmonary artery to the imaging plane is assumed to be negligible. Deconvolutions were then performed on the super-pixel data set using the REG2 deconvolution method described in Chapter 4.

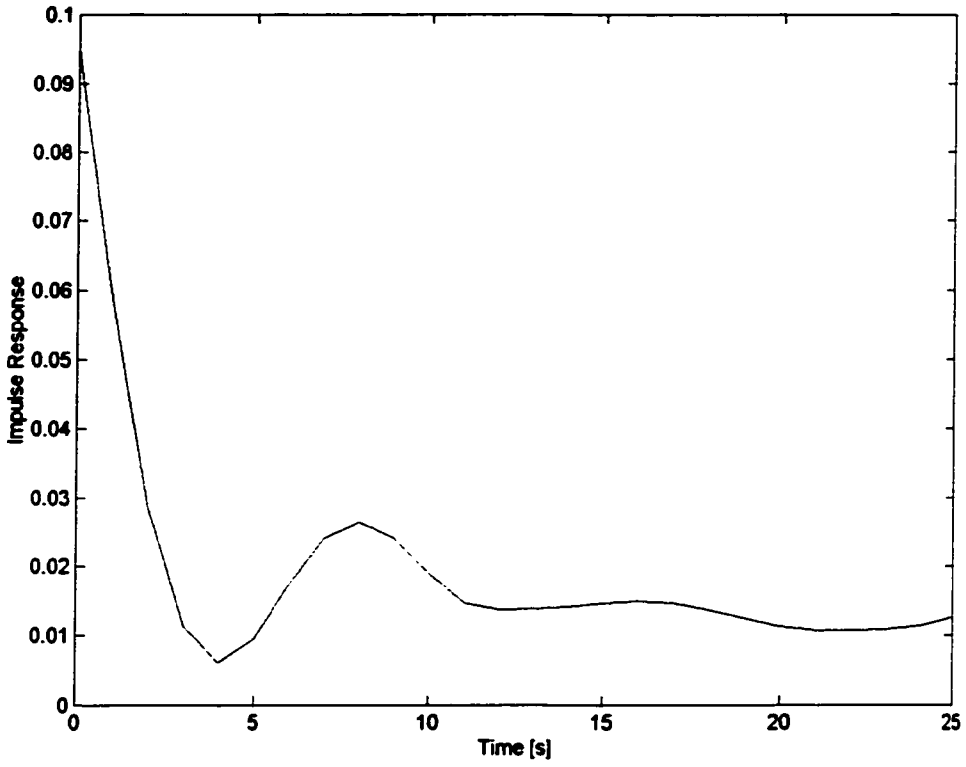

Figure 5-12: Typical impulse response of the lung.

Figure 5-12 illustrates a typical impulse response function obtained from the deconvolution of an arterial input function and tissue function. Note that the shape of the response function exhibits a sharp initial pulse followed by a smaller but broad pulse. The initial peak suggests rapid flow of contrast, possibly from partial volume effects of smaller feeding vessels within the super-pixels. The secondary pulse centered about 7 seconds was also observed by Tajik *et al.*, who suggest that the secondary peak is a measure of the micro-vascular transport through the alveoli and small vessels, as opposed to the initial peak, which is from partial volume measurements of arterial input

signals within the ROI. It is unclear whether the third peak is a deconvolution artifact or perhaps more complex blood flow patterns within the human lung parenchyma than the traditional exponential behavior.

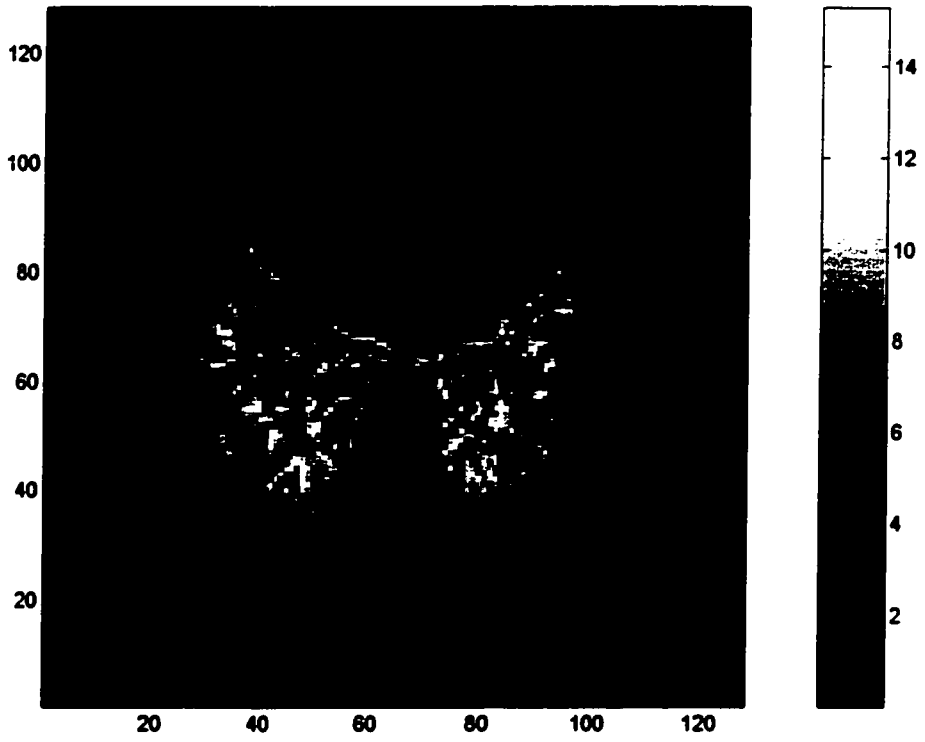

Figure 5-13: Estimates of mean tissue transit times in the lung. Units are in seconds (s).

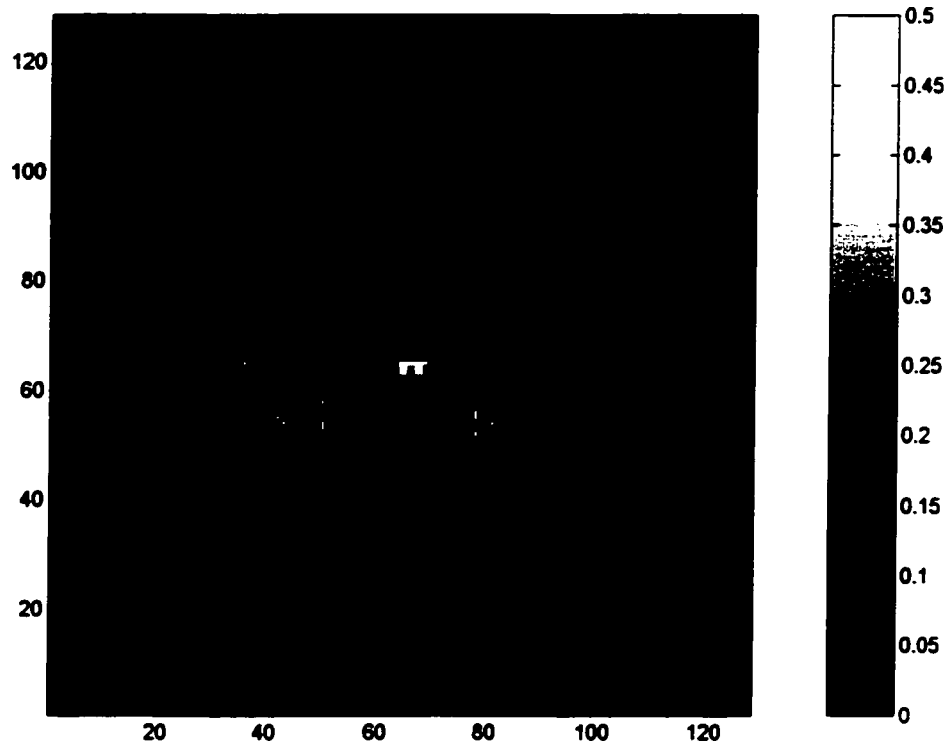

Figure 5-14: Estimates of lung blood flow. Units are in ml of blood flow per second, per ml of lung tissue (ml/s /ml).

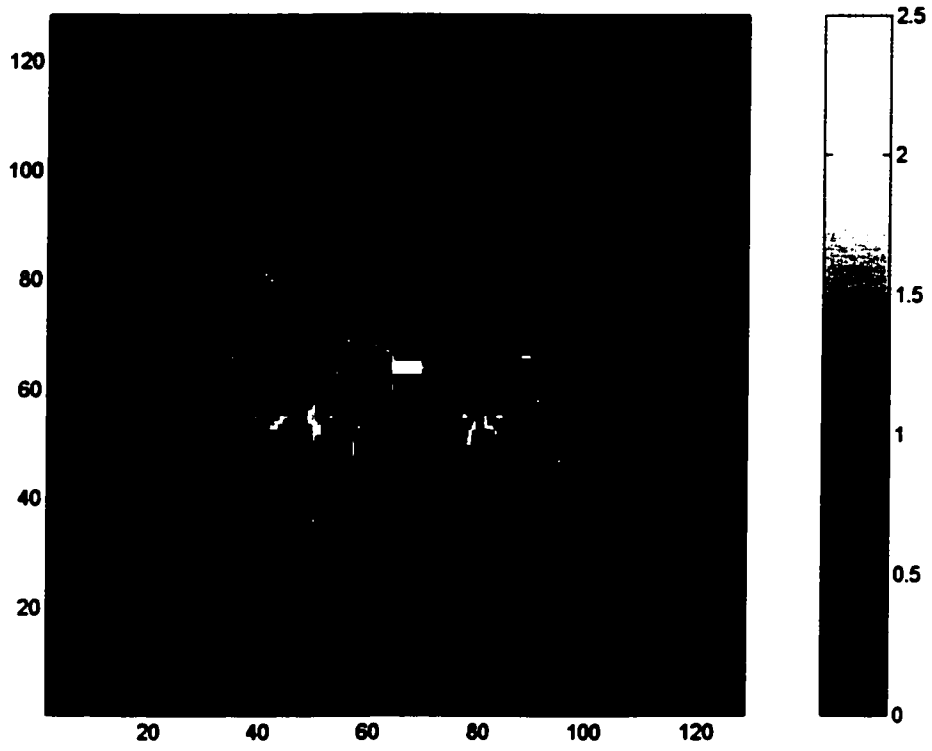

Figure 5-15: Estimates of lung blood volume. Units are in ml of blood volume per ml of lung tissue (ml / ml).

Figure 5-13 to 5-15 display the estimates of MTT, LBF, and LBV based on the analysis of the super-pixel data set. Note the difference in window and level settings of each of the images. The LBF and LBV images illustrate the vessel structure of blood flow and volume in the central regions of the lung lobes, and less vessel structure along the periphery of the lung, where smaller vessel and alveoli are believed to exist. The MTT image suggests that the mean tissue transit time of blood through the super-pixels ranges from 3 to 10 seconds. These values are slightly higher than the results of Maseri

et al. and Tajik *et al.*, the latter performed f-CT measurements in dog-lung, but are approximately equal to values predicted by Fung (1997). Note however, that the estimate of the MTT may depend on the total duration of the estimated impulse response function. That is, if more time-samples were used to estimate the impulse response function, different values of MTT may be obtained. Alternative methods of computing MTT may also be used [Miles *et al.*1997].

5.4 Discussion

In f-CT studies, the assumption of linearity between concentration and *CT#* is valid only for concentrations where beam hardening is not a concern, which is roughly about 75 mgI/ml. The lower limit of detectability for contrast concentration is no less than 0.300 mgI/ml. As the photon attenuation in the rod increases, the total number of photons reaching the detectors decreases and results in larger noise.

In f-CT of the lung, a larger signal to noise ratio is achieved when either 100 or 120 kVp photons are used in the scanning protocol. The kVp settings of 100, 120 and 140 kVp may be approximated by a mono-energetic photon with energies of 65, 72 and 78 keV. The effects of non-blood flowing volumes within the CT voxel may result in a net increase in *CT#* but reduced contrast enhancement. Although the effects of slice thickness are significant in reducing noise in water, they are less significant in lung. The fact that the noise in lung tissue is less than that in water may be due to the decreased radiological pathlength and therefore increased number of photon detections during the imaging sequence. The expected error in the *CT#* of stationary (non-moving nor blood flowing) lung is approximately 3 *CT#*.

In a f-CT study, there are potentially two sources of uncertainty when estimating the *CT#*. First, there will be uncertainty in the *CT#* of the lung tissue without contrast. Second, there is uncertainty in the tissue estimate due to streaking artifacts caused by the time-dependent contrast flow. In Chapter 3, the maximum error in *CT#* peripheral to a time-dependent vessel was approximately 40 in water. If it is assumed that these errors are independent, then the total error in the *CT#* in a water phantom may be as large as 41. Despite this large error, a signal should still be detectable in the lung.

The lower attenuation in lung tissue results in increased complexity in estimating the noise. It remains unclear what role the reconstruction algorithm plays in the noise estimate. But because the noise in the lung is smaller than in water, it is plausible that the uncertainties in *CT#* due to the time-dependent signal may also be lower. If this is true, then as a crude approximation, if it is assumed that the noise in the lung due to reconstruction is reduced by a fraction of the density (as is somewhat the case in the noise due to sampling), then the maximum total noise in the lung may be $[(40 \div 3)^2 + 3^2]^{1/2} \sim 14$ *CT#*. If it is assumed that the *CT#* in lung is approximately 300 *CT#*, then this suggests that the maximum error in the *CT#* of the lung is approximately 5 % for 120 kVp photons. As this is a worst-case scenario, this error would apply only to those voxels peripheral to a major vessel experiencing dramatic changes in density. Thus, the error in the *CT#* in lung in a f-CT study would be less than 5% proximal to large arteries, and much less farther from arteries.

Using a lower (100 or 120 kVp) photon energy ensures a higher signal to noise ratio primarily due to the increase in attenuation at lower energies. This would make

sense since fewer emitted photons are required to achieve the same signal to noise level in the lung than in, for example, the brain or abdomen due to the differences in radiological pathlength. Despite this, the reduction of noise in lung does not imply increased accuracy in *CT#* in the lung. A higher density resolution may be achieved by using a larger scanning volume and smoother kernels in the reconstruction algorithm [Kemerink *et al.* 1997].

The effects of the parenchyma tissue may be significant if the relative volume of the parenchyma tissue is large. Increasing the relative volume of parenchyma tissue would result in a decrease in the parameter α by a factor roughly equal to the fraction of parenchyma tissue in the CT voxel. For example, when the ROI contains only contrast and water, α is measured at 32.7. A crude estimate of α when 20% of the volume contains non-blood flowing volumes would be 32.7 x (1-0.2) = 26.2, which is displayed in Table 5-3 in parentheses.

Theory would suggest that, given a variety of tissue response parameters (as defined by the ATH model), a signal much greater than the noise should be measurable. Further, perfusion-like parameter estimates should be attainable in most circumstances. The limiting factor in the analysis is the duration of the image acquisition. In tissues containing large extra-vascular volumes the relative amounts of contrast uptake will be small, resulting in a lower signal to noise ratio.

Density	α [CT#/mgI/ml]	Noise [CT#]	FOM
ρ=1.00 g/cm^3 , v_p=0.00	32.7 +/- 0.3	9.9 +/- 2.1	3.30 +/- 0.73
ρ=1.00 g/cm^3 , v_p=0.20	27.4 +/- 0.3 (26.2)	9.9 +/- 2.1	2.77 +/- 0.63
ρ=0.33 g/cm^3 , v_p=0.00	10.8 +/- 0.1	3.3 +/- 0.7	3.27 +/- 0.72
ρ=0.33 g/cm^3 , v_p=0.20	8.2 +/- 0.1 (8.6)	3.3 +/- 0.7	2.48 +/- 0.56

Table 5-3: Figure of merit statistic with v_p =0.0 and 0.2 for 100 kVp photons. In parentheses is the relative volume of non-parenchymal (1- v_p) space multiplied by α when v_p is zero.

We show through a patient study that it is indeed possible to measure increases in lung tissue signals when a sharp contrast bolus is administered through the antecubital vein. Signals in the lung can then be used in deconvolution analysis to yield perfusion-like parameters.

In all f-CT studies, dose to the patient is a concern. Thermoluminescent dosimeters were used to measure the dose in typical f-CT scan in the lung. Typical doses for 5 mm slice thickness and 120 kVp ranged from 2-2.5 cGy. Thus, for a 30 second study, total dose within a slice is approximately 60-75 cGy. Although this dose may seem fairly high, it is fractional compared to dose ranges in radiation therapy.

Because little is known about the impulse response in the lung, a non-model based method was chosen for the deconvolution. The deconvolution method suggested here provides more stable estimates of the impulse response function than other non-

model based approaches. However, parameter estimates from this deconvolution may be biased [Madden *et al.* 1996]. Model based approaches may also be used to describe the impulse response to yield more stable results [King *et al.* 1996, St. Lawrence *et al.* 1999b]. These are areas of future research. Regardless, it should be noted that the quantitative analysis itself is not limited to the linear systems approach used here. There are a large number of additional, and perhaps simpler, methods available for interested users [Miles *et al.* 1997]. However, methods based solely on rise-times of sharp contrast boluses would not be recommended.

6. Conclusions

6.1 Summary of major findings

6.1.1 Use of ABC to reduce respiratory motion

The Active Breathing Control device can reproduce the position of the diaphragm within an imaging study. Because of this, the quality of diagnostic exams and radiation therapy may be improved. It is recommended that patients be carefully screened before a decision is made to use this device for diagnostic or therapeutic purposes.

Using this device, diaphragmatic motion becomes reduced by approximately 1.1 cm. Assurances must be made that the margin allotted for respiration does not increase from conventional margins when using ABC. These margins may be assessed during the initial simulation session. If the ABC device is used prior to imaging or treatment to screen patients whose range in motion is greater with the ABC device, significant reductions in diaphragm motion can be expected.

As discussed in Appendix A, Active Breathing Control was successfully implemented in the radiation therapy of a metastatic lesion in the liver. The ABC device significantly reduced the amount of healthy-tissue margins normally allotted in radiation therapy. Significant reductions in dose and volume of healthy tissue, most notably the heart, were observed when using ABC. It is likely that given the dose-volume constraints, adequate coverage of the planning target volume would not have been attainable were it

not for the use of ABC. Based on the results of this patient, the standard deviation of the diaphragm displacement was 2 mm.

The resource implications of using ABC routinely in the clinic are minor. Three additional hours were required to implement and deliver the ABC plan, while at least one additional person was also required throughout the course of therapy. A well-trained therapist or dosimetrist may easily deliver ABC plans with the aid of a trained simulation and therapist crew.

6.1.2 Fidelity of concentration to CT number

In f-CT studies, the assumption of linearity between concentration and *CT#* is valid only for concentrations less than 75 mgI/ml. The lower limit of detectability for contrast concentration is 0.300 mgI/ml. As the concentration increases, beam hardening in the rod also increases; therefore, the total number of photons reaching the detectors decreases, which results in increased noise.

A model for spatial and temporal averaging of dynamic CT signals has been developed. This model can accurately predict the signals when the details of the time-density curve are known beforehand. A result of this spatial and temporal averaging is that high frequency components of the true time-density curve become lost. When there are large changes in the density during the image acquisition, there no longer remains the simple linear relationship between contrast concentration and *CT#*.

The effects of this spatial and temporal averaging are small for most conventional CT scanners for most blood flow velocities that one would expect in f-CT studies of the lung. In larger vessels, however, the spatial and temporal averaging may become a

concern. A better understanding of the velocity field within the CT voxel would greatly improve the reliability of parameter estimates yielded from f-CT procedures.

There is a potential pitfall when using f-CT as a prognostic tool. Unless it is certain that the velocity of the contrast within the voxel(s) remains the same before and after the therapy, there may be errors in f-CT perfusion estimates. Within the context of radiation therapy, it is quite possible for the blood-flow velocities to change after the course of treatment. The subsequent parameter estimates yielded from these 'before and after' f-CT studies may therefore be erroneous.

In f-CT, the *CT#* of voxels surrounding major vessels containing the contrast may be perturbed due to the CT reconstruction of a time-dependent signal. In water, these perturbations may change the *CT#* estimates by as much as 40 *CT#* in water; subsequently, perfusion estimates derived from perturbed data sets are subject to errors. Therefore, special considerations should be taken when examining tissue immediately adjacent to vessels carrying contrast.

6.1.3 Parameter estimation in the lung

Because the fidelity of contrast concentration and CT number remains uncertain when there are large changes in density, f-CT methods which rely on the rise-time of the CT data are prone to errors. In these situations, other methods, such as linear systems analysis, may be preferable.

When the form of the impulse response function is known, model-based techniques are suggested for use in deconvolution analysis of tomographic images. In situations where little is known about the impulse response function, the use of output

information can be very useful in estimating the impulse response function. In the method described in Chapter 4, two – rather than one – deconvolutions are performed, which requires more computation time. Integrating the use of input, tissue and output data in deconvolution analysis of tomographic images provides more physically meaningful and stable forms of the impulse response functions while also providing good matches with measured data. This method can be easily adapted to other, and perhaps more reliable deconvolution methods.

6.1.4 Feasibility of f-CT in the lung

If a small but concentrated injection of contrast is delivered antecubitally, a f-CT signal in the lung should be observable. Because the lung tissue consists primarily of air, efforts should be made to ensure that the optimal CT scanning parameters, which maximize the signal to noise ratio, are used. In attempting f-CT of the lung, a large signal to noise ratio can be achieved when either 100 or 120 kVp photons are used in the scanning protocol. Although the effects of slice thickness are significant in reducing noise in water, it appears to be less critical in lung.

If performing f-CT on a patient, some consideration should be given to the expected amount of non-blood flowing volumes within the lung. In a first-pass CT study, the non-blood flowing volume may increase the *CT#* in the voxel(s), but it also reduces the relative contrast enhancement in the lung. The expected error in the *CT#* of stationary (non-moving nor blood flowing) lung is estimated at approximately 3 *CT#*.

F-CT was performed on a cancer patient who was to receive radiation therapy in the lower thorax. Perfusion estimates were obtained by using a protocol of 350 mgI/ml of

Iodinated contrast administered antecubitally at an injection rate of 4 ml/s for 5 seconds. The timing of the contrast delivery (via autoinjector), the CT image acquisition, and the respiratory immobilization is critical in this study. However, when these issues are accounted for, perfusion estimates can be obtained in the lung.

6.2 Implications of this work

Because CT scanners are readily available in most clinics, and because the implementation of f-CT requires only slight modifications to existing imaging protocols, it is possible to obtain both anatomical and functional lung data within a single CT session. The protocol requires only 20 ml of contrast agent which is well below the tolerance, as opposed to more conventional volumes of approximately 100 ml or greater. Thus, toxicity from the contrast is not a major concern.

Further, the costs of breathing control and auto-injectors are marginal compared to other modalities of perfusion imaging such as functional MRI, and nuclear medicine techniques. The f-CT images in this study were limited to a single slice due to the limitations of the CT scanner. However, volumetric perfusion measurements can be obtained with commercially available multi-slice CT scanners.

Patients do receive an additional source of radiation as a result. However, the additional dose received during an f-CT study of the lung is fractional (tens of centiGray) compared to the dose ranges typically given to radiation therapy patients (tens of Gray). In the clinical example discussed in this work, the f-CT study contributed 2% of the total dose the patient received, which is equal to the margin of error in the treatment machine calibration.

6.3 Future work

This thesis focused on developing a method to measure lung tissue damage from radiation therapy. Thus, future work may focus on performing f-CT on patients after they have received radiation therapy and correlating the loss of perfusion with local dose. Today, techniques which decrease dose to healthy tissue, such as respiratory gating and intensity modulated radiation therapy, are being developed and implemented in the clinical setting. Because of its high precision, f-CT in the lung can be used to gauge the effectiveness of respiratory gating and intensity modulated radiation therapy in reducing normal tissue complications.

F-CT may also be applied to measure the perfusion of lung tumors during or after the course of therapy. That is, this method may also be applied to obtain a better understanding of tumor response to radiation. A signature of cancer is abnormal blood flow patterns. Changes in cancerous blood-flow may be observable if f-CT is used during or after the course of therapy.

Outside the context of radiation therapy, there are a wide class of diseases and lung disorders that could benefit from f-CT analysis. F-CT of the lung can be used to diagnose other pathological conditions in the lung indicated by abnormal perfusion patterns. For example, perfusion patterns in conditions such as pneumonia, tuberculosis, asthma, and pulmonary edema may be better understood with f-CT.

It is demonstrated here that f-CT of the lung can be used in the diagnosis and prognosis of a large number of diseases in and around the lung which alter the pulmonary blood flow. Our interest is to better understand how lung tissue responds to radiation

during the course of radiation therapy. Functional CT in the lung may not only be used as a tool to measure regional radiation damage in the lung, but it may also be used to guide practitioners in the treatment and prognosis of cancer.

References

Anderson E, Bai Z, Bischof C, Blackford S, Demmel J, Dongarra J, Du Croz J, Greenbaum A, Hammarling S, McKenney A, Sorensen D 1999 "LAPACK User's Guide" 3rd Edition, SIAM, Philadelphia

Anton H, Rorres, C 1987 "Elementary Linear Algebra With Applications" John Wiley & Sons Inc. Toronto

Armstrong J G, Burman C, Leibel S A, Fontenla D, Kutcher G J, Zelefsky M and Fuks Z 1993 "Three-dimensional conformal radiation therapy may improve the theraputic ratio of high dose radiation therapy for lung cancer" *Int. J. Radiat. Oncol. Biol. Phys.* **26** 685-9

Axel L 1980 "Cerebral blood flow determination by rapid-sequence computed tomography" *Neuroradiology* **137** 679-86

Basran PS 1997 "Optimization of lung cancer treatment" MSc Thesis University of Alberta

Bassingthwaighte J B, Ackerman F H, Wood E H 1966 "Applications of the lagged normal density curve as a model for arterial dilution curves" *Circ. Res.* **18** 398-415

Berninger W H, Redington R W 1979 "Dynamic computed tomography" in *Radiology of the skull and brain, Vol V: Technical aspects of computed tomography* Newton, T H and Potts D G (Editors) 4261-4285 C.V. Mosby, New York

Bertero M, Bindi D, Boccacci P, Cattaneo M, Eva C and Lanza V 1998 "A novel blind-deconvolution method with an application to seismology" *Inverse Problems* **14** 815-33

Boersma L J, Damen E M, de Boer R W, Muller S H, Roos C M, Valdes Olmos R A, van Zandwijk N and Lebesque J V 1994 "Dose-effect relations for local functional and structural changes of the lung after irradiation for malignant lymphoma" *Radiother. Oncol* **32** 201-9

Bronikowski T A, Dawson C A, Linehan J H 1983 "Model-free deconvolution techniques for estimating vascular transport functions" *Int. J. Bio-Medical Computing* **14** 411-29

Brooks R A, Di Chiro G 1977 "Slice geometry in computer assisted tomography" *J. Comput. Assist. Tomogr.* **1** 191-9

Brugmans M J, van der Horst A, Lebesque J V and Mijnheer B J 1999 "Beam intensity modulation to reduce the field sizes for conformal irradiation of lung tumors: a dosimetric study." *Int. J. Radiat. Oncol. Biol. Phys.* **43** 893-904

Bushberg J T, Seibert J A, Leidholdt E M, Boone J M 2001 "The essential physics of medical imaging" Lippincott Williams & Wilkins 2nd Edition Baltimore USA

Charter M K, Hull S F 1987 "Maximum entropy and its application to the calculation of drug absorption rates" *J. Pharmacokin. Biopharm.* **16** 85-107

Chao K S, Deasy J O, Markman J, Haynie J, Perez C A, Purdy J A, Low D A 2001 "A prospective study of salivary function study in patients with head and neck cancers receiving intensity-modulated or three-dimensional radiation therapy: initial results" *Int. J. Radiat. Oncol. Biol. Phys.* **49** 907-16

Charter, M.K., Gull, S.F. (1987) "Maximum entropy and its application to the calculation of drug absorption rates" *J. Pharmacokin. Biopharm.* **15** 645-655

Clough A V, Dayong C, Linehan J H, Krenz G S, Dawson C A and Maron M B 1993 "Model-free numerical deconvolution of recirculating indicator concentration curves" *J. Appl. Physiol.* **74** 1444-53

Coulam C M, Warner H R, Marshall H W, Bassingthwaighte J B 1967 "A steady-state transfer function analysis of portions of the circulatory system using indicator dilution techniques" *Comput. Biomed. Res.* **1** 124-138

Cottrall M F 1977 "Considerations of the application of indicator dilution methods to the measurement of the flow rates of fluids" *Phys. Med. Biol.* **22** 693-713.

Costello P, Dupuy D E, Ecker C P, Tello T 1992 "Spiral CT of the thorax with reduced volume of contrast material: a comparative study" *Radiology* **183** 663-6

Cox J D, Barbor-Derus S, Hartz A J, Fischer M, Byhardt R W, Komaki R, Wilson J F and Greenberg M 1986 "Is adenocarcinoma/large cell carcinoma the most radiocurable type of cancer of the lung?" *Int. J. Radiat. Oncol. Biol. Phys.* **12** 1801-1805

Crawford C R, King K F 1990 "Computed tomography scanning with simultaneous patient translation" *Medical Physics* **17** 967-82

Davies S C, Hill A L, Holmes R B, Halliwell M 1994 "Ultrasound quantitation of respiratory organ motion in the upper abdomen" *British Journal of Radiology* **67** 1096-1102

De Nicolao G, Liberati D 1993 "Linear and nonlinear techniques for deconvolution of hormone time-series" *IEEE Trans. Biomed. Eng.* BME-40 440-455

De Nicolao, G 1994 "Nonparametric deconvolution of physiological systems: a stochastic approach" In Modeling and control in biomedical systems. Proceedings of the IFAC symposium, Patterson B W, Editor Omnipress, Madison 1994, 252-253

Dean P B, Plewes D B 1984 "Contrast media in computed tomography." In: Radiocontrast Agents M. Sovak (Editor) Berlin Springer-Verlag New York

Doriot P A, Dorsaz P A, Dorsaz L and Rutishauser W J 1997 "Is the indicator dilution theory really the adequate base of many blood flow measurement techniques?" *Medical Physics* **24** 1889-98

Emami B, Lyman J, Brown A, Coia L, Goitein M, Munzenrider J E, Shank B, Solin L J and Wesson M 1991 "Tolerance of normal tissue to therapeutic irradiation" [Review] *Int. J. Radiat. Oncol. Biol. Phys.* **21** 109-21

Fleming J S, Kemp P M 1999 "A comparison of deconvolution and the Patlak-Rutland plot in renography analysis" *J Nucl. Med.* **40** 1503-7

Fung Y C 1997 "Biomechanics: Circulation" 2nd Edition. Springer-Verlag New York

Fuss M, Wenz F, Scholdei R, Essig M, Debus J, Knopp M V, Wannenmacher M 2000 "Radiation-induced regional cerebral blood volume (rCBV) changes in normal brain and low-grade astrocytomas: quantification and time and dose-dependent occurrence." *Int. J. Radiat. Oncol. Biol. Phys.* **48** 53-8

Gong Q Y, Brunt J N, Romaniuk C S, Oakley J P, Tan L T, Roberts N, Whitehouse G H and Jones B 1999 "Contrast enhanced dynamic MRI of cervical carcinoma during radiotherapy: early prediction of tumour regression rate." *Br. J. Radiol.* **72** 1177-84

Graham M V, Matthews J W, Harms W B Sr, Emami B, Glazer H S and Purdy J A, Gur D , Drayer B P , Borovetz H S , Griffith B P , Hardesty R L and Wolfson S K 1994 "Three-dimensional radiation treatment planning study for patients with carcinoma of the lung." *Int. J. Radiat. Oncol. Biol. Phys.* **29** 1105-17

Galvin J R , Gingrich R D , Hoffman E , Kao S C S , Stern E J and Stanford W 1994 "Ultrafast computed tomography of the chest" *Radiologic Clinics of North America* **32** 775-793

Ganong W F 1999 "Textbook of medical physiology" Appleton & Lange 19th Edition Toronto

Gur D, Drayer B P, Borovetz H S, Griffith B P, Hardesty R L, Wolfson S K 1979 "Dynamic computed tomography of the lung : Regional ventilation measurements" *Journal of Computed Assisted Tomography* **3** 749-753

Hamming R 1987 "Numerical methods for scientists and engineers" Dover Press 2nd Edition UK

Hanley J, Debois M M, Mah D, Mageras G S, Raben A, Rosenzweig K, Mychalczak B,

Schwartz L H, Gloeggler P J, Lutz W, Ling C C, Leibel S A, Fuks Z, Kutcher G J 1999 "Deep inspiration breath-hold technique for lung tumors: the potential value of target immobilization and reduced lung density in dose escalation." *Int. J. Radiat. Oncol. Biol. Phys.* **45** 603-11

Hansen P C, O'Leary D P 1993 "The use of the L-curve in the regularization of discrete ill-posed problems" SIAM *J. Sci. Comput.* **14** 1487-1503

Hanson K M 1979 "Noise and contrast discrimination in computed tomography" in *Radiology of the skull and brain, Vol V: Technical aspects of computed tomography* Newton, T H and Potts D G (Editors) 3941-3955 C.V. Mosby, New York

Harikumar G and Bresler Y 1998 "FIR perfect signal reconstruction from multiple convolutions: minimum deconvolver orders" *IEEE Transactions on Signal Processing* **46** 215-8

Herbert D L, Gur D, Shabason L, Good W F, Rinaldo J E, Snyder J V, Borovetz H S, Mancici M C 1982 "Mapping of human local pulmonary ventilation by xenon enhanced computed tomography." *J. Comput. Assist. Tomogr.* **6** 1088-93

Hobday P, Hodson N J, Husband J, Parker R P, MacDonald J S 1979 "Computed tomography applied to radiotherapy treatment planning: Techniques and results" *Radiology* **133** 477-482

Hoffman E A, Tajik J K, Kugelmass S D 1995 "Matching pulmonary structure and perfusion via combined dynamic multislice CT and thin-slice high-resolution CT." *Comput. Med. Imaging Graph.* **19** 101. 101-12

Hubbell J H 1995 "Tables of X-ray mass attenuation coefficients and mass energy-absorption coefficients 1 keV to 20 MeV for Elements Z=1 to 92 and 48 additional substances of dosimetric interest" Technical report NISTIR 5623 NIST, Gaithersburg USA

Huber P E, Hawighorst H, Fuss M, van Kaick G, Wannenmacher M F and Debus J 2001 "Transient enlargement of contrast uptake on MRI after linear accelerator (linac) stereotactic radiosurgery for brain metastases." *Int. J. Radiat. Oncol. Biol. Phys.* **49** 1339-49

Hovorka R, Chappell M J, Godfrey K R, Madden F N, Rouse M K and Soons P A 1998 "CODE: a deconvolution program implementing a regularization method of deconvolution constraine to non-negative values. Description and pilot evaluation" *Biopharmaceutics & Drug Disposition* **19** 39

Huesman R H and Mazoyer B M 1987 "Kinetic data analysis with a noisy input function" *Phys. Med. Biol.* **32** 1569-79

Johns H E, Cunningham J R 1983 "Physics of Radiology" Charles C Thomas 4th Edition Springfield USA

Kay I, Basran P S, Spencer D P 2002 "On the fidelity of CT-number and actual concentration behaviour" (in preparation)

Kearfott K J, Rottenberg D A, Deck M D 1983 "Optimization of xenon-enhanced CT studies: beam energy, enhancement, root mean square deviation, and repeatability" *Am. J. Neuroradiol.* **4** 195-9

Kemerink GJ, Kruize HH, Lamers RJ 1997 "The CT's sample volume as an approximate, instrumental measure for density resolution in densitometry of the lung" *Med. Phys.* **24** 1615-20

Knopp T J, Bassingthwaighte J B 1976 "Transcoronary intravascular transport functions obtained via a stable deconvolution technique" *Ann. Biomed. Eng.* **4** 44-59

Koh T S, Zeman V, Lee T-Y, Milosevic M F, Haider M, Warde P, Yeung I W T 2001 "The inclusion of capillary distribution in the adiabatic tissue homogeneity model of blood flow" *Phys. Med. Biol.* **46** 1519-1538

Kubo H D, Hill B C 1996 "Respiration gated radiotherapy: a technical study" *Phys. Med. Biol.* **41** 43-91

Lane D A, Patel I C, Sirs J A 1975 "The variation of indicator dilution curves with velocity profile" *Phys Med Biol.* **20** 613-23

Lee T Y, Ellis R J, Dunscombe P B, McClarty B, Hodson D I, Kroeker M A, Bews J 1990 "Quantitative computed tomography of the brain with xenon enhancement: a phantom study with the GE9800 scanner" *Phys. Med. Biol.* **35** 925-35

Leibel S A, Heimann R, Kutcher G J, Zelefsky M J, Burman C M, Melian E, Orazem J P, Mohan R, LoSasso T J, Lo Y C *et al.* 1994 "Three-dimensional conformal radiation therapy in locally advanced carcinoma of the prostate: preliminary results of a phase I dose-escalation study." *Int. J. Radiat. Oncol. Biol. Phys.* **28** 55-65

Liao Z X, Travis E L and Tucker S L 1995 "Damage and morbidity from pneumonitis after irradiation of partial volumes of mouse lung" *Int. J. Radiat. Oncol. Biol. Phys.* **32** 1359-1370

Li. J and Cutler D J 1998a "Stability of finite difference deconvolution I: theoretical analysis" *Biopharmaceutics & Drug Disposition* **19** 547-594

Li J and Cutler D J 1998b "Stability of finite difference deconvolution II: simulation studies" *Biopharmaceutics & Drug Disposition* **19** 595-603

Littleton J T, Durizch M L, Moeller G, Herber D E 1990 "Pulmonary masses: contrast enhancement" *Radiology* **177** 861-71

Macovski A 1979 "Principles of reconstruction algorithms" in *Radiology of the skull and brain, Vol V: Technical aspects of computed tomography* Newton T H, Potts D G (Editors) 3877-3903 C.V. Mosby, New York

Madden F N, Godfrey K R, Chappell M J, Hovorka R and Bates R A 1996 "A comparision of six deconvolution techniques" *Journal of Pharmacokinetics and Biopharmaceutics* **24** 283-299

Mageras G, Ramsey C R 2000 personal communication

Mah D, Hanley J, Rosenzweig K E, Yorke E, Braban L, Ling C C, Leibel S A and Mageras G 2000 "Technical aspects of the deep inspiration breath-hold technique in the treatment of thoracic cancer" *Int. J. Radiat. Oncol. Biol. Phys.* **48** 1175-85.

Mah K, Van Dyk J 1988 "Quantitative measurement of changes in human lung density following irradiation." *Radiother. Oncol.* **11** 169-79.

Mah K, Caldwell C B, Ung Y C, Danjoux C E, Balough J M, Ganguli S N, Ehrlich L E, Tirona R "The impact of (18) FDG-PET on target and critical organs in CT-based treatment planning of patients with poorly defined non-small cell lung carcinoma: a prospective study" *Int. J. Radiat. Oncol. Biol. Phys.* **52** 339-50

Marks L B, Spencer D P, Bentel G C, Ray S K, Sherouse G W, Sontag M R, Coleman R E, Jaszczak R J, Turkington T G, Tapson V and *et al.* 1993 "The utility of SPECT lung perfusion scans in minimizing and assessing the physiologic consequences of thoracic irradiation" *Int. J. Radiat. Oncol. Biol. Phys.* **26** 659-68.

Marks L B, Spencer D P, Sherouse G W, Bentel G, Clough R, Vann K, Jaszczak R, Coleman E R and Prosnitz L R 1995 "The role of three dimensional function lung imaging in radiation treatment planning: the functional dose-volume histogram" *Int. J. Radiat. Oncol. Biol. Phys.* **33** 65-75

MacManus M P, Hicks R J, Ball D D L, Ciavarella F, Binns D, Hogg A, Kalff V, Ware R, Wirth A, Salminen E, McKenzie A 2002 "Imaging with F-18 FDG PET is superior to T1-201 SPECT in the staging of non-small cell lung cancer for radical radiation therapy" *Australas. Radiol.* **45** 484-90

Madden F N, Godfrey K R, Chappell M J, Hovorka R, Bates R A 1996 "A comparison of six deconvolution techniques" *Jour. Pharmaco. Biopharm.* **24** 283-299

Maseri A, Caldinin P, Permutt S, Zierler K L 1970 "Frequency function of transit times through dog pulmonary circulation" *Circ. Res.* **26** 527-43

Mayozer B M, Huesman R H, Budinger T F, Knittel B L 1986 "Dynamic PET data anaylsis" *J. Comput. Assist. Tomogr.* **10** 645-53

Mignotte M, Meunier J 2000 "Three-dimensional blind deconvolution of SPECT images" *IEEE Transactions on Biomedical Engineering* **47** 274-80

Miles K, Dawson P, Blomley M 1997 "Functional computed tomography" Martin Dunitz Oxford UK

Mori M, Murata K, Takahashi M, Shimoyama K, Ota T, Morita R, Sakamoto T 1994 "Accurate Contiguous Sections without breath-holding on chest CT: value of respiratory gating and ultrafast CT" *Am. J. of Roentgen.* **162** 1057-1062

Mutic S, Grigsby PW, Low DA, Dempsey JF, Harms, WB, Laforest R, Bosch WR, Miller TR 2002 "PET-guided three-dimensional treatment planning of intracavitary gynecologic implants" *Int. J. Radiat. Oncol. Biol. Phys.* **52** 1104-10

Nabavi D G, Cenic A, Craen R A, Gelb A W, Bennett J D, Kozak R and Lee T Y 1999 "CT assessment of cerebral perfusion: experimental validation and initial clinical experience." *Radiology* **213** 141-9.

Nakai M 1981 "Computation of transport function using multiple regression analysis" *Am. J. Physiol. Heart Circ. Physiol.* **240** H133-H144

Oguchi K, Sone S, Kasuga T, Sakai F, Maruyama Y, Watanabe T, Feng L, Andoh T, Nakadai Y 1996 [Methodological study of hemodynamic analysis of lung mass by contrast enhanced dynamic CT] *Nippon Igaku Hoshasen Gakkai Zasshi* **56** 496-501 Japanese

Ohara K, Okumura T, Akisada M, Inada T, Mori T, Yokota T and Calaguas M J B 1989 "Irradiation synchronized with respiration gate" *Int. J. Radiat. Oncol. Biol. Phys.* **17** 853-857

Patlak C S, Blasberg R G, Fenstermacher J D 1983 "Graphical evolution of blood to brain transfer constants in multijob time uptake data" *Journal of Cerebral Blood Flow and Metabolism* **3** 1-7

Polacin A, Kalendar W A, Marchal G 1992 "Evaluation of section sensitivity profiles and image noise in spiral CT" *Radiology* **185** 29-35

Press W H, Teukolsky S A, Vetterling W T, Flannery B P 1992 "Numerical recipies in C: The art of scientific computing" Cambridge University Press 2nd Edition. Cambridge

Ritchie C J, Hsieh J, Gard M F, Godwin J D, Kim Y, Crawford C R 1994 "Predictive respiratory gating: a new method to reduce motion artifacts on CT scans" *Radiology* **190**

847-852

Rubin G D, Dake M D and Semba C P 1995 "Current status of three-dimensional spiral CT scanning for imaging the vasculature." *Radioll. Clin. North. Am.* **33** 51-70.

St. Lawrence K S, Lee T Y 1998a "An adiabatic approximation to the tissue inhomogeneity model for water exchange in the brain: I. Theoretical derivation" *J. Cereb. Blood Flow Metab.* **18** 1365-77

St. Lawrence K S, Lee T Y 1998b "An adiabatic approximation to the tissue inhomogeneity model for water exchange in the brain: II. Experimental validation" *J. Cereb. Blood Flow Metab.* **18** 1378-85

Statistics Canada 1999 *Table 102-0003: Selected causes by death, by sex, Canada, provinces, territories and health regions, annual* Retrieved Jan 12 2002 from the World Wide Web: http://www.statscan.org

Sutton D G and Kempi V 1991 "Constrained least-squares restoration and renogram deconvolution: a comparison by simulation" *Phys. Med. Biol.* **37** 53-67

Swensen S J, Viggiano R W, Midthun D E, Muller N L, Sherrick A, Yamashita K, Naidich D P, Patz E F, Hartman T E, Muhm J R and Weaver A L 2000 "Lung nodule enhancement at CT: multicenter study." *Radiology* **214** 73-80

Szabo Z, Nyitrai L and Sondhaus C 1987 "Effects of statistical noise and digital filtering on the parameters calculated from the impulse response function" *Eur. J. Nucl. Med.* **13** 148-54

Tajik J K, Tran B Q, Hoffman E A, 1998 "New technique to quantitate regional pulmonary microvascular transit times from dynamic x-ray CT images" SPIE: Medical Imaging 1998, Conference Proceedings #3337-04

Ten Haken R K, Balter J M, Marsh L H, Robertson J M and Lawrence T S 1997 "Potential benefits of gating conformal irradiation of liver tumors to the ventilatory cycle" ASTRO 1997 Conference Proceedings

Thompson H, Starmer C, Whalen R and McIntosh H 1964 "Indicator transit time considered as a gamma-variate" *Cir. Res.* **14** 502-12

Tucker S L, Liao Z X and Travis E L 1997 "Estimation of the spatial distribution of target cells for radiation pneumonitis in mouse lung." *Int. J. Radiat. Oncol. Biol. Phys.* **38** 1055-66

Ueberhuber, C W (1997a) "Numerical Computation 1: Methods, Software, and Analysis" Springer-Verlag, New York

Ueberhuber, C W (1997b) "Numerical Computation 2: Methods, Software, and Analysis" Springer-Verlag, New York

Vadja S, Godfrey K R and Valko P 1988 "Numerical deconvolution using system identification methods" *Journal of Pharmacokinetics and Biopharmaceutics* **16** 85-107

Veng-Pedersen P 1980 "An algorithm and computer program for deconvolution in linear pharmacokinetics" *Journal of Pharmacokinetics and Biopharmaceutics* **8** 463-481

Verotta D 1993 "Two constrained deconvolution methods using spline functions" *Journal of Pharmacokinetics and Biopharmaceutics* 21: 609-639

Weinstein H, Acosta B S, Bernstein B, Shaffer A B 1973 "Estimation of circulatory blood volume from a tracer response curve." *IEEE Trans. Biomed. Eng.* BME-20 269-277

Wirestam R, Andersson L, Ostergaard L, Bolling M, Aunola J, Lindgren A, Gieger B, Holtas S and Stahlberg F 2000 "Assessment of regional cerebral blood flow by dynamic susceptibility contrast MRI using different deconvolution techniques" *Magnetic Resonance in Medicine* **43** 691-700

Wolfkiel C J, Ferguson J L, Chomka E V, Law W R, Labin I N, Tenzer M L, Booker M and Brundage B H 1987 Dec 1987 "Measurement of myocardial blood flow by ultrafast computed tomography." *Circulation* **76** 1262-73

Wong J W, Sharpe M B, Jaffray D A, Kini V R, Robertson J M, Stromberg J S, Martinez A A 1999 "The use of active breathing control (ABC) to reduce margin for breathing motion." *Int. J. Radiat. Oncol. Biol. Phys.* **44** 911-9

Wu X, Latson L A, Wang T, Driscoll D J, Ensing G J, Ritman E L 1988 "Regional pulmonary perfusion estimated by high-speed volume scanning CT." *Am J Physiol Imaging* **3** 73-80

Xie Q, Chen N-X "Matrix-inversion method:applications to Mobius inversion and deconvolution" *Physical Review E* **52** 6055-65

Yamashita K, Matsunobe S, Tsuda T, Nemoto T, Matsumoto K, Miki H and Konishi J 1995 "Solitary pulmonary nodule: preliminary study of evaluation with incremental dynamic CT." *Radiology* **194** 399-405.

Zierler K L 1965 "Equations for measuring blood flow by external monitoring of isotopes." *Circ. Res.* **16** 309-321

Appendix A: Clinical Example of the use of Active Breathing Control in Radiation Therapy

With the encouraging results of the ABC diaphragm study, an opportunity was sought to use this device clinically. In May of 2001, a palliative patient who presented with metastatic lesions in the liver was selected for treatment with the ABC device at the Tom Baker Cancer Centre.

A.1 Methods and Materials

The patient being treated was a woman (age > 50 years) who presented a primary cancer of the gastro-intestinal tract and several metastatic lesions in the liver. The object of the treatment was to deliver a high and uniform dose of 3000 cGy to a large mass of metastatic lesions within the liver. Because the liver is situated directly beneath the diaphragm, it is subject to respiratory motion. Normally, margins specifically allotted for respiratory margins are determined by simply adding 2.0 cm superior and inferior to the target volume. This additional margin results in significant amounts of healthy tissue that are irradiated simply to ensure adequate coverage of the tumor volume throughout the breathing cycle. The object of using ABC was to reduce these margins as much as possible while ensuring that the tumor volume always remains within the treatment fields.

A.1.1 CT-Simulation

The first step in radiation therapy delivery is a CT simulation of the patient to assess the geometric extent of the tumor and the surrounding healthy tissues. For liver cases, this is achieved by obtaining two sets of CT images: the first is a treatment planning CT to define the planning volume in the dose calculation; the second is a contrast-enhanced CT image set to delineate the tumor volume. The planning CT images represent the patient geometry and positions of the various regions of interest throughout the course of treatment. Because ABC is used throughout the treatment, CT images taken with ABC best represent the planning geometry.

Without the use of contrast, metastatic lesions in the liver are difficult to identify on CT images. Iodinated contrast material is often used to identify metastatic lesions due to pathologic blood-flow patterns. By using contrast-enhanced CT images, the extent of lesion may be better approximated and therefore, provide more accurate target delineation. The contrast-enhanced images may be merged with the planning CT to completely specify the geometric extent of both the critical structures and the planning target volume. The planning target volume contours are best represented when ABC is used in the image acquisition.

A.1.2 Treatment Planning

A commercial treatment planning system was used to devise the treatment plan [Pinnacle-3 V4.2.1 ADAC Laboratories, Milpitas USA]. Dose-volume constraints were determined by the Radiation Oncologist and are shown in Table A-1. Once the gross tumor volume (GTV) was defined, an additional 3 mm margin was 'grown' around the

GTV for daily set-up variations. An additional 5 mm was used in the superior-inferior direction to account for respiratory motion. Normally, this margin is 20 mm, but with the use of ABC, smaller margins are expected. Once the plan is accepted, digitally reconstructed radiographs (DRRs) are computed and produced for verification purposes.

Table A-1: Dose-volume constraints for the treatment plan.

Organ	Dose [Gy]	Volume [Relative]
Heart	< 25	1/3
	< 5	2/3
Kidneys (both)	< 10	Total
Liver	< 20	1/4
	< 5	1/2
Tumor	30	approx. 1/4

A.1.3 Treatment Simulation and Verification

Once the treatment plan has been accepted, the patient undergoes treatment verification by simulating treatment on a diagnostic x-ray machine, and then a mock treatment on the linear accelerator.

Verification of field placement is easily achieved through alignment of external marks when treating a rigid body. This is, however, almost never the case; internal anatomical marks are subject to anisotropic deformations and rotations. For this reason, the position of bony landmarks relative to field placements is often used when verifying

treatment fields. By gating the radiation beam, it is hoped that the diaphragm is less prone to these deformations and may provide a robust fiducial mark. Both diaphragm and bony fiducial marks in relation to the field assist in assessing field alignment. It is important to stress that neither the bony fiducial mark nor the diaphragm will be completely stationary throughout a single or multiple treatments. It is expected, however, that the position of either mark be represented with a probability distribution. A goal of ABC is to reduce the variance of that probability distribution as much as possible.

During the first simulation session SSDs are checked with the treatment planning CT. Two marks are placed on the patient's skin based on the central axis of the beam while the gantry is at 0 and 90 degrees. The patient and table are then shifted to align these points with the central-axis of the beam. Once the patient is aligned, two x-ray images are taken in the anterior-posterior (AP) and lateral (LAT) directions and compared against the DRRs to verify the patient position. Bony landmarks, surrounding normal tissues and field edges are visually compared to the position of the central-axis to assess any potential shifts. Marks are also placed on the skin at the beam entry points for the treatment fields. The SSD distances are also recorded and checked against those found during the CT simulation.

Since the patient is being treated with ABC, all images were obtained using the ABC device. To verify the position of the tumor volume during treatment, three ABC images were acquired for each of the treatment fields and the reference (AP and LAT) fields. Since the diaphragm is not visible in all treatment fields, the jaws of the x-ray

fields were widened so as to ensure that a portion of the diaphragm could be measured for each of the beam and reference fields. A visual check of the diaphragm displacement during normal respiration was also performed to assess whether the ABC would be of benefit to the patient.

The process of checking AP and LAT films against DRRs was repeated prior to the patient's first treatment on the linear accelerator. If there are no significant shifts in the field or tumor volume and the patient is able to undergo the treatment, the first treatment is given.

A.1.4 Treatment

The 3000 cGy were delivered in 10 fractions, one fraction per day. During the first and fifth day, AP and LAT films were taken to assess variations between simulation and treatment. These images may be obtained manually with hard-copy portal films, or electronically with electronic portal images (EPI). The advantages of film are that the image quality is superior to EPI and less dose is required to form an image. The advantages of EPIs are that images are electronically stored and that images may be obtained during the treatment. The EPIs can be obtained in 'cine-mode', which is concurrent acquisition of images during the treatment. Approximately 15 cGy to the tumor volume is required to generate an image. Each day, 300 cGy is delivered and thus provides 20 images each day. If the diaphragm or bony landmarks are visible within the treatment fields, an assessment of the reliability of ABC can be made.

A.2 Results

A.2.1 CT-Simulation

Prior to CT imaging, a twenty-minute training session was given to the patient prior to the CT simulation to familiarize the patient on the use of the ABC device and to determine the maximum breath hold duration. The patient was able to hold her breath for no longer than 15 seconds during this time. This required us to perform multiple ABC sessions with treatment and imaging sessions.

Two CT images were required for this patient: the first being a large volumetric image which encompassed the liver and adjacent structures; the second being a contrast enhanced set of images to delineate the metastatic lesions. Prior to the CT image acquisition, a 'scout' or 'pilot' view is also normally required to determine the CT image acquisition parameters such as axial distance scanned. Thus, three ABC images were required during the first simulation session.

During the image acquisition, the patient laid supine on the CT couch and the simulation staff aligned the patient to the reference lasers of the CT machine. Simultaneously, the CT image sequence were keyed into the console until the last step is to 'BEAM-ON'. The ABC mouth-piece was placed in the patients mouth and the software was checked to detect a signal. When the software is operating smoothly, the patient was instructed, via intercom, that the valve will be closed on her next breath. Once the valve was locked, the instruction of 'BEAM-ON' was given to the simulation staff and CT images were taken until one second remained in the ABC session. At this point, the instruction 'BEAM-OFF' was given.

The pilot view lasts only several seconds and was acquired within 10 seconds. Based on the pilot, an axial distance of approximately 21 cm was required to completely scan the treatment volume.

For treatment planning purposes, the axial resolution of the CT images must be as fine as possible; for convenience, the images must be acquired in a reasonable amount of time. For these reasons, an axial resolution of 0.3 cm was used for treatment planning purposes. This resolution is consequently the measured margin of reproducibility of the diaphragm position. The images were acquired in spiral mode.

Once the treatment planning images were acquired, a contrast-enhanced set of images of the liver lesions was obtained. The total scan length was limited to the superior-inferior extents of the lesions plus a small margin. These images were obtained using a pitch and index of 5 and 5 mm, respectively.

These images were then exported to the treatment planning system to delineate the various regions of interest and perform the dose calculation.

A.2.2 Treatment Planning

Contours of the treatment volume and the surrounding normal structures were performed on ADAC's Pinnacle Treatment Planning System [ADAC Laboratories, Milpitas USA]. The treatment planning system (TPS) has image fusion features that allow for the merging of the contrast-enhanced CT images with the treatment planning images.

External contour variations were measured to be less than 3 mm in the axial direction. Because this variation is equal to the axial resolution, the effect of these contour variations in the treatment plan is considered insignificant.

Figure A-1 also shows a final version of the treatment plan, displaying the calculated dose, beams placements, and prescription point. Three beams were used at various oblique angles about the patient. Wedges and beam weights were modified to ensure a uniform dose around the planning target volume.

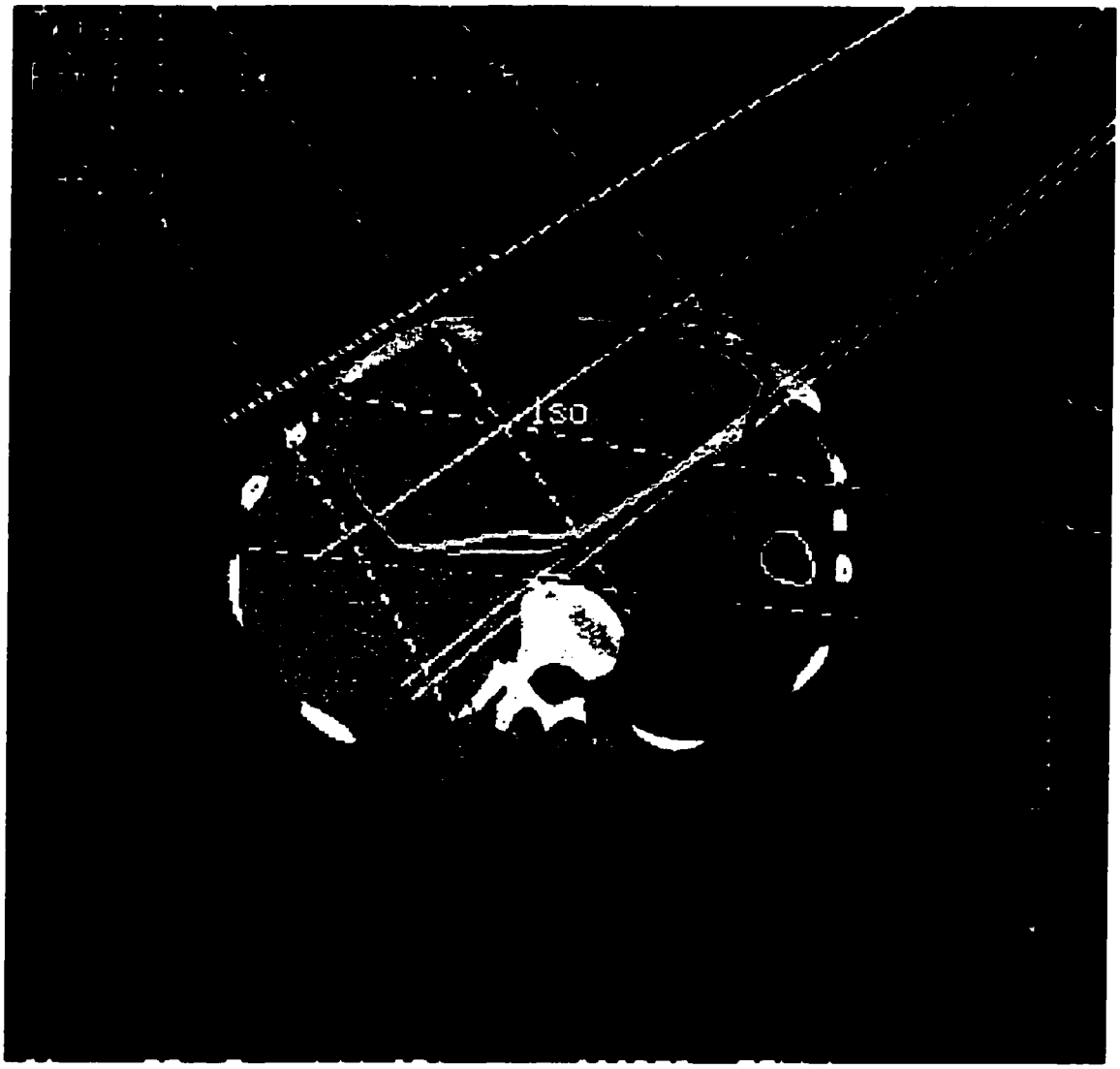

Figure A-1: Isodose plot of the treatment plan in axial plane of the prescription point.

To assess the benefit of using ABC for this treatment, Figure A-2, Figure A-3, and Figure A-4 display the beam's eye view for the three beams when using a 0.5 and 2.0 cm respiratory margin. The contours of the spinal cord, heart, normal liver, kidneys, are displayed in relation to delivered field sizes with the multi-leaf collimators (MLC).

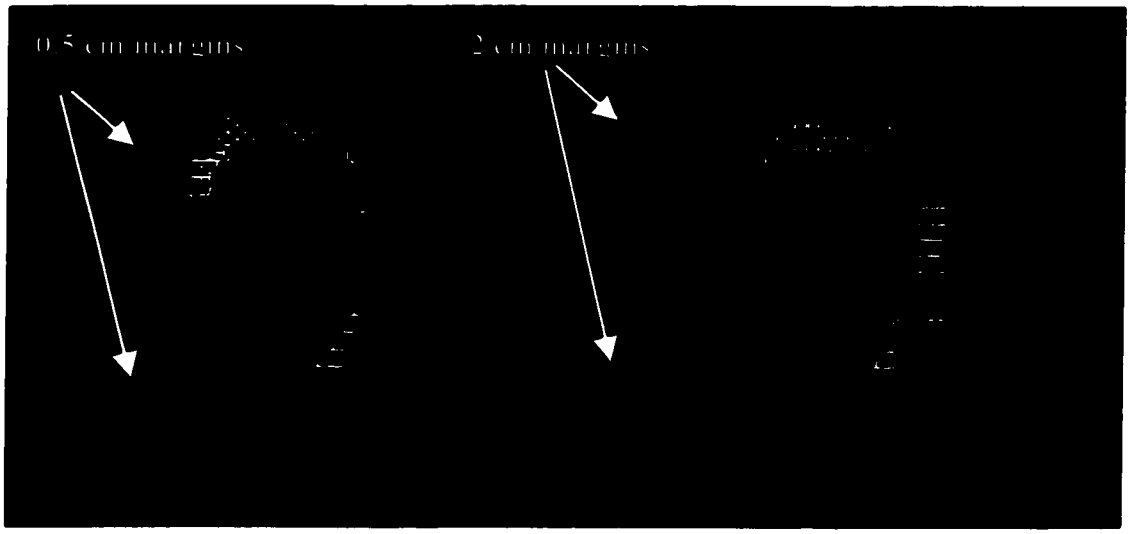

Figure A-2: Beam's eye view for beam #1.

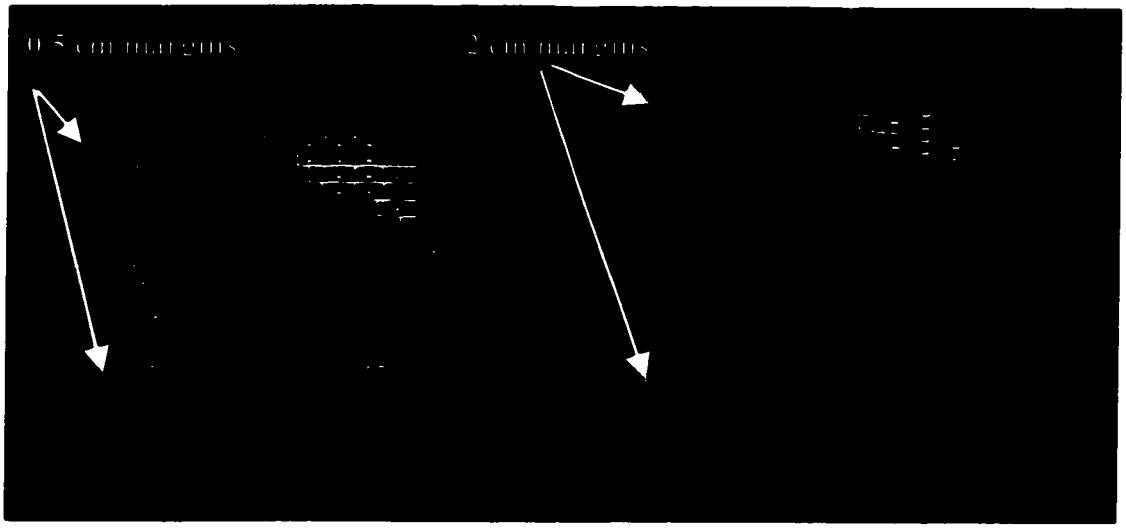

Figure A-3: Beam's eye view for beam #2.

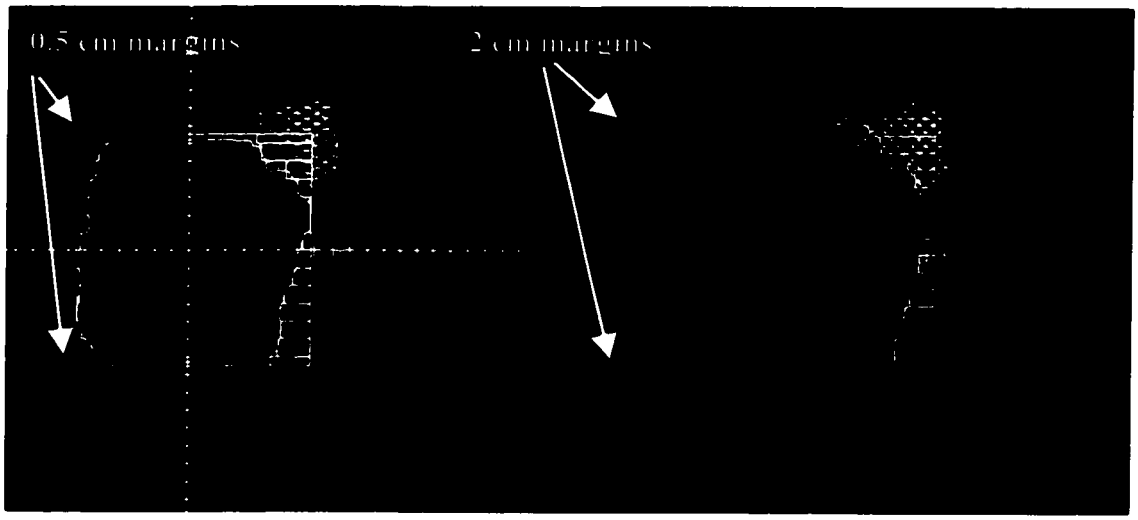

Figure A-4: Beam's eye view for beam #3.

For all beams, the irradiated volume of spinal-cord, heart, normal liver, and kidneys are reduced when using a 0.5 cm margin. This is best illustrated in Figure A-5, which shows the dose-volume histograms (DVHs) of the normal structures. For all organs, there is a significant reduction in the dose-volume histograms when using ABC.

Note that given the dose-volume constraints for the heart, as identified in Table A-1, the treatment plan with 2.0 cm margins would not be deliverable. It is likely that this particular patient could not receive radiation therapy to the liver due to excessive toxicity to the heart.

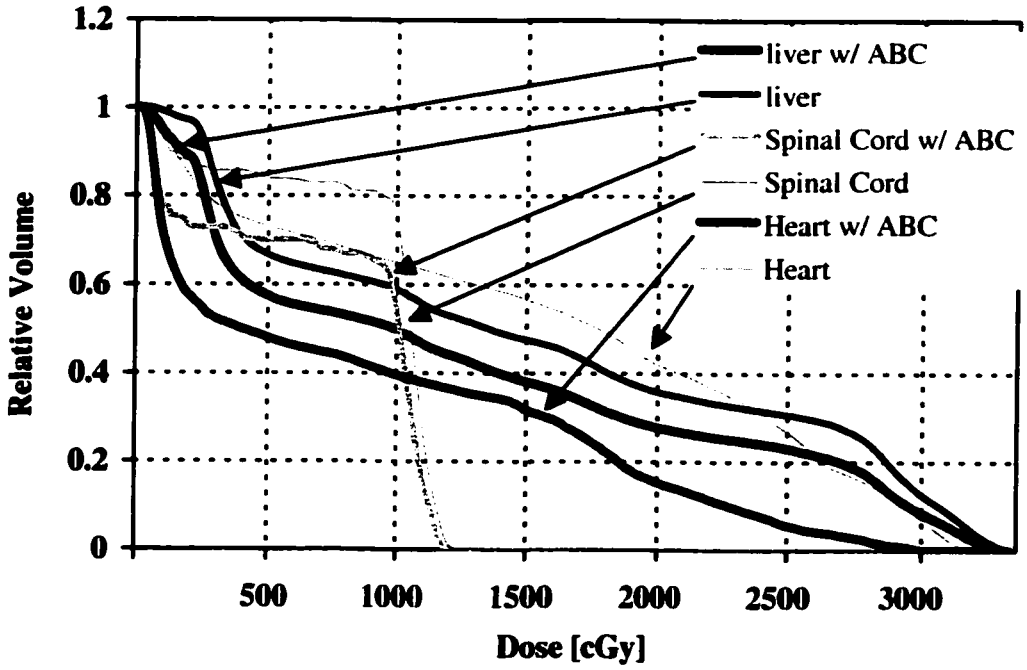

Figure A-5: Dose volume histograms of critical structures with and without ABC.

Another way of assessing the merits of respiratory gating is to examine the coverage of dose to the tumor volume which meet the normal tissue tolerances. That is, rather than decreasing the dose to normal tissue by reducing the PTV margins, reduce the dose to the tumor volume such that the normal tissue tolerances are met. Figure A-6 displays the coverage of the PTV if the ABC dose-volume constraints were met with a 2.0 cm margin for respiratory motion. Note that there is significant reduction in the dose delivered to the tumor volume. Thus, it is plausible that even if a treatment plan could be

delivered with the 2.0 cm margin, the planning target volume would not receive a homogeneous -and therefore tumorcidal- dose.

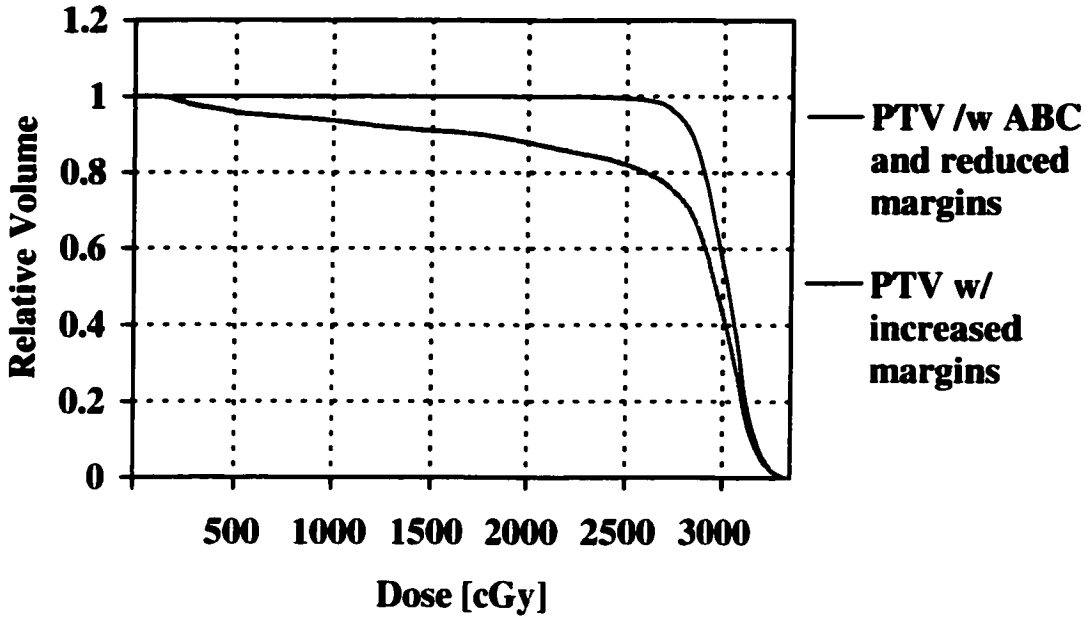

Figure A-6: Dose volume histogram of the planning target volume with and without 2.0 cm margins with constant dose-volume constraints.

A.2.3 Treatment Simulation and Verification

During normal breathing, the left and right diaphragm moves 0.7 and 2.0 cm, respectively. With three repeated ABC images, the maximum difference in position of the diaphragm was measured with respect to the beam's central axis and also with respect to a common fiducial mark in the spinal cord (see Table A-2). Measurements of the right diaphragm are most useful in estimating the motion of the tumor since the tumor resides in the right side of the patient. However, the dome of the right diaphragm is not visible within the treatment fields. During the simulation, the jaws of the x-ray

source were widened such that the dome of the diaphragm was visible. This was also done for the verification on the first treatment day.

Table A-2: Maximum difference in diaphragm with respect to the beam's central axis and a bony landmark during simulation. Note that no bony landmarks were visible in the simulation and port images except for beam #3.

Beam	Maximum difference of diaphragm w.r.t Beam Left / Right [cm]	Maximum difference of diaphragm w.r.t spine Left / Right [cm]
AP (no ABC)	0.7 / 2.0	NA / NA
AP (with ABC)	0.3 / 0.2	0.3 / 0.2
1	0.2 / 0.1	NA / NA
2	0.2 / NA	NA / NA
3	0.3 / 0.1	0.3 / 0.1

Scoliosis of the patient's spine resulted in more difficult patient alignment. More will be discussed on this later.

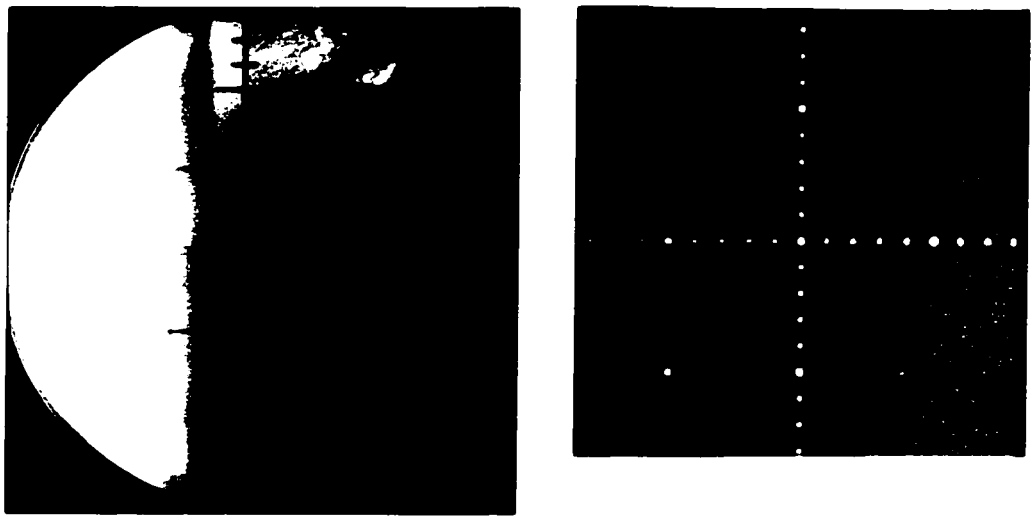

Figure A-7: Simulation (left) and first treatment verification fields for beam # 1.

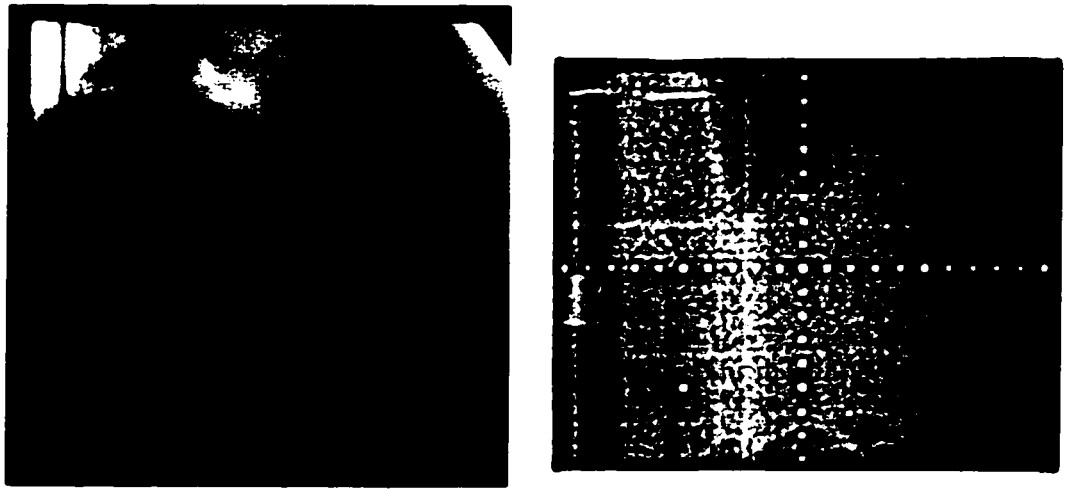

Figure A-8: Simulation (left) and first treatment verification fields for beam # 3.

On the first treatment day, portal images of the AP beam and three treatment fields were taken with ABC and anatomical positions were checked against the simulation images.

Only the first and third beam provided anatomical marks that could be compared against the simulation images. Figure A-7 and Figure A-8 displays the simulation and first treatment verification field. For Figure A-7, the diaphragm dome appeared to be within several millimeters of the simulation. For Figure A-8, the dome of the diaphragm appears to be in within several millimeters and the junction between the diaphragm and spinal cord appear to be in roughly the same positions. Note that during normal respiration, the same diaphragm moves approximately 2.0 cm. The field positions with respect to the bony landmark and diaphragm position appeared to be clinically acceptable and the decision was made to treat.

A.2.4 Treatment

Because the beam-on time for beams 1 and 2 were much longer than the patient's maximum breath-hold, the treatment beams were delivered in two sections. During the patient set-up, the mouthpiece was inserted as the very last step for each beam. The console of the linear accelerator was queued up until the very last step was pressing the 'BEAM-ON' button. The linear accelerator must clear various interlocks before the machine can deliver radiation. As soon as the mouthpiece was inserted, the staff exited the treatment room and waited for the door-interlock to clear. Once all interlocks cleared, the patient was instructed via intercom "*On your next breath*", the valve will close. Once the valve was locked, the instruction to 'BEAM-ON' was given to the therapist operating the linear accelerator console. One second before the valve was opened (15 seconds into the treatment), the instruction was given to 'BEAM-OFF', thus allowing one second for possible delays in reaction time. Once the machine was turned

off, a small delay (typically 10 seconds) was given in order for the patient to recuperate from the previous breath hold. Once a stable breathing pattern was observed on the ABC laptop, the instruction and delivery sequence was repeated.

EPIs were taken in cine-mode for each field and were quickly checked after the treatment for gross field-alignment errors. At the completion of the therapy, the EPIs were analyzed in more detail. Because the MLC fields and collimator jaws conceal many of the important landmarks used during the simulation, verifying the beam placement during the course of the treatment proved a more difficult task. In beams 1 and 2, the left diaphragm was visible and thus a measurement of the diaphragm with respect to the beam's central axis could be made. In beam 2, an inter-vertebral space was visible and thus a measurement of the spinal cord could be made. In many immobilization studies, the spinal cord is used as a reference mark since it is assumed that spine moves very little throughout the course of treatment. The variability in the spinal cord thus acts as a measure of patient set-up reliability. Therefore, for beam # 3, it was possible to examine those variations that are due to daily set-up errors (via the inter-vertebral space) and those due to respiratory immobilization (via the diaphragm).

EPIs were taken for each field for each beam on every fraction. Approximately 3, 7, and 14 images were acquired during a fraction for beams 1,2 and 3.

For beams 1 and 2, the vertical extent of the diaphragm with respect to the beam's central axis was measured. Figure A-9 displays a typical EPI image of beam # 2. For reference, each of the MLC fields are one centimeter in width.

Figure A-9: Typical EPI from beam # 2. Both the spine and diaphragm dome are observable for treatment verification.

Table A-3 displays the results of the analysis for beams 1 and 2. The average position is computed by calculating the average position within a fraction, and computing an average of the average values. Therefore it represents the average position of the mark throughout the treatment. The actual value of the diaphragm and reference mark with respect to the central axis is unimportant; however, the difference in positions over the course of the treatment reflects the uncertainty in the patient alignment. The standard deviation, displayed in the second row, provides some insight on the amount of movement throughout the course of treatment. Movement of the diaphragm primarily stem from two sources: daily mis-alignment of the treatment fields to the tumor volume;

and respiratory motion. The total standard deviation of the diaphragm thus contains the effects of both the mis-alignment of the treatment field along with the effects from using the ABC. While this statistic is useful from a practical point of view, it does not independently provide insight on the efficacy of ABC immobilization.

Table A-3: Beam # 1 and 2 statistics of diaphragm and reference mark positions.

	Beam # 1	**Beam # 2**		
	Diaphragm [cm]	Diaphragm [cm]	Reference - Sup [cm]	Reference - Lat [cm]
Position over all fxs.	4.21	3.99	2.48	2.66
Stand. dev. in position over all fx.	0.62	0.74	0.23	0.28
Average of Stand. dev. over all fx	0.17	0.23	0.07	0.09
Max. stand. dev in 1 fx.	0.34	0.31	0.11	0.12
Max. range over all fx.	2.25	2.25	0.90	1.23
Max. range in 1 fx	1.14	0.94	0.37	0.41

The average of the standard deviations, displayed in the third row, provides some insight on how much a point moves within a treatment. The reference mark moves less than a millimeter, which is on the order of the resolution and inter-observer variability. The average of the standard deviations of the diaphragm is approximately 2 mm. This suggests that within a single treatment, the diaphragm may move +/- 2 mm approximately 68 % of the time with a maximum range of 11 mm. Note also that large

differences in reference position were often accompanied with large differences in diaphragm position, which suggests systematic displacement errors.

The diaphragm was observed to move over 2 cm when comparing all fractions, and even within a fraction, a maximum displacement of 9 mm was observed. However, the inter-vertebral mark also shows up to 4 mm shift during a single treatment and up to 1.2 cm shift throughout the treatment.

Beam # 1 shows similar results in almost all statistics, but with slightly smaller standard deviations. No fiducial marks could be identified on the EPIs of beam # 3.

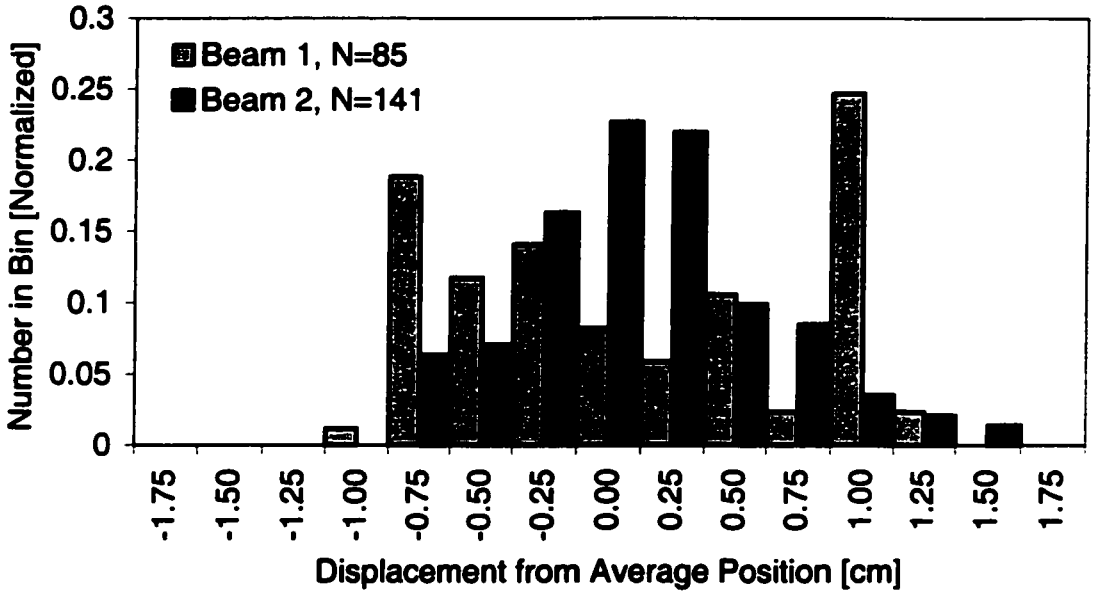

Figure A-10: Histogram plot of average displacements of diaphragm for beams 1 and 2.

Figure A-10 displays a histogram of displacements with respect to the average position of the diaphragm for beams 1 and 2. It is interesting to note that although beam

2 loosely represents a single tail, un-skewed distribution, the same cannot be said for beam 1. A large number of measurements were found with the diaphragm 1.00 cm beyond the average position. When analyzing the data closely, the majority of the 1.00 cm deviation occurred in two days (fractions 6 and 9) and all of 0.75 cm deviations occurred in a single day (fraction 8). This would suggest that these peaks are more likely to be due to a systematic error in field placement for a fraction, rather than being the error associated with the use of ABC. Such systematic variations were not as evident for beam 2.

After the first treatment, subsequent treatments required less than 20 minutes to deliver. After each treatment, examining the EPIs for gross mis-alignments required 10 minutes. Set-up of the ABC was done simultaneous to patient set-up and thus required no additional time.

A.3 Discussion

The first use of ABC at the TBCC was successfully completed. The ABC device reliably reproduces the position of the diaphragm and most likely the tumor position. By reducing the treatment margin allotted for respiration, significant reductions in the volume of peripheral normal tissues are achieved. In this clinical example, the patient would not receive radiation therapy due to excessive toxicity to the heart. Furthermore, it is likely that even if dose volume constraints were met while using larger treatment margins, adequate coverage of the tumor volume may not be attainable.

Despite the set-up error, the reproducibility of the diaphragm was approximately 2 mm, which agrees with the results of Wong *et. al* (1999) in his initial report on the use

of ABC. If we use the maximum observed range throughout the course of treatment as the necessary margin when using ABC (2.25 cm in the superior-inferior direction, or 1.1 cm margin superior and inferior to the treatment volume), this margin is still much less than the conventionally prescribed margin of 2.0 cm. A much smaller margin, such as 4 or 6 mm, would ensure 95 or 99 % confidence in the planning margin, assuming the positioning error when using ABC is normally distributed.

Table A-4: Resources required to implement and deliver ABC radiation therapy.

Task	Time w/ ABC [hours]	Normal [hours]	Additional resources / people
CT Simulation	1.00	0.50	1-2 additional
Treatment Planning	1.00	1.00	
Treatment Simulation	1.00	0.50	1-2 additional
Treatment with verification	0.75	0.50	
Subsequent treatments	0.33 / fx	0.25 / fx	1-2 additional
Post treatment analysis	0.18 / fx	0.08 / fx	1 additional
TOTAL over 10 fractions	**8.52**	**5.55**	

An important question regarding the feasibility of ABC for routine radiation therapy is that of the resources required to deliver the plan. Shown in Table A-4 are the times devoted to developing and implementing the conventional and ABC radiation therapy plans.

The majority of the additional time (approximately 3 hours) is spent in verifying the simulation and treatment fields. However, the time spent evaluating the images may

be reduced if the results of the ABC verification are reliably within accepted tolerances. The use of EPIs proved to be extremely useful in assessing these errors and considerable time-savings may be achieved from automating the simulation and EPI analysis.

One well-trained person, in conjunction with a trained therapist and simulation staff, is probably sufficient to deliver the ABC treatment. With adequate training, a radiation therapist or dosimetrist may easily implement the ABC, with the aid of the existing simulation and therapist staff.